Fundamental Studies of Irradiation-Induced Modifications in Microstructural Evolution and Mechanical Properties of Advanced Alloys

James Stubbins, University of Illinois at Urbana-Champaign, PI
Brent Heuser, University of Illinois at Urbana-Champaign, co-PI
Peter Hosemann, University of California, Berkeley, co-PI
Meimei Li, Argonne National Laboratory, co-PI

Final Report
April 24, 2018

Authors
Xiang Liu, James Stubbins

Office of Nuclear Energy
U.S. Department of Energy
Project No. NEUP 14–6762
Contract No. DOE DE-NE0008291
Project Period: October 2014 to December 2017

Contents

EXECUTIVE SUMMARY

This final technical report summarizes the research performed during October 2014 and December 2017, with a focus on investigating the radiation-induced microstructural and mechanical property modifications in optimized advanced alloys for sodium-cooled fast reactor (SFR) structural applications.

To accomplish these objectives, the radiation responses of several different advanced alloys, including austenitic steel Alloy 709 (A709) and 316H, and ferritic/martensitic Fe–9Cr steels T91 and G92, were investigated using a combination of microstructure characterizations and nanoindentation measurements. Different types of irradiation, including *ex situ* bulk ion irradiation and *in situ* transmission electron microscopy (TEM) ion irradiation, were employed in this study. Radiation-induced dislocations, precipitates, and voids were characterized by TEM. Scanning transmission electron microscopy with energy dispersive X-ray spectroscopy (STEM-EDS) and/or atom probe tomography (APT) were used to study radiation-induced segregation and precipitation. Nanoindentation was used for hardness measurements to study irradiation hardening.

Austenitic A709 and 316H was bulk-irradiated by 3.5 MeV Fe^{++} ions to up to 150 peak dpa at 400, 500, and 600℃. Compared to neutron-irradiated stainless steel (SS) 316, the Frank loop density of ion-irradiated A709 shows similar dose dependence at 400℃, but very different temperature dependence. Due to the noticeable difference in the initial microstructure of A709 and 316H, no systematic comparison on the Frank loops in A709 vs 316H was made. It would be helpful that future ion irradiation study on 316 stainless steel could be conducted to directly compare the temperature dependence of Frank loop density in ion-irradiated 316 SS with that in neutron-irradiated 316 SS. In addition, future neutron irradiation on A709 at 400–600℃ at relative high dose ($\geqslant$10 dpa) can be carried out to compare with ion-irradiated A709.

The radiation-induced segregation (RIS) of Ni and Si was observed in both A709 and 316H in all irradiated conditions and was found at various sinks: line dislocations, dislocation loops, void surfaces, carbide-matrix interfaces, etc. Radiation also induced the formation of Ni,Si-rich precipitates. As suggested in a previous study on neutron-irradiated 316 stainless steel, one possible consequence of the significant RIS of Si is that the enrichment at defect sinks depletes the silicon in the matrix, which can lead to enhanced void nucleation rate. The enrichment of Ni and Si is accompanied by the depletion of Cr at defect sinks, which could also affect the corrosion resistance.

Radiation-induced change in the orientation relationship of pre-existing MX precipitates was observed at 600℃. It is believed that this change is associated with the network dislocations formed under irradiation. The underlying mechanism is still not well understood. This change could be a positive indication that the MX precipitates can survive high density network dislocations. It would be helpful if neutron irradiation at similar dose conditions could be carried out to verify that this effect is not unique for ion irradiation.

Intragranular Cr-rich carbides with a core-shell structure, i.e. Cr-rich carbide core and Ni,Si-rich shell was found at 500℃ and 600℃ in the highest dose (150 peak dpa) specimens. Coarse voids (∼30 nm in diameter) were only commonly found at 500℃ in the 50 and 150 peak dpa specimens in regions less than 750 nm in depth. The highest swelling for A709 irradiated to 50 and 150 peak dpa at 500℃ is about 0.44% and 0.37%, respectively. Due to the choice of 100 degree temperature intervals, this study did not attempt to precisely identify peak void swelling conditions, merely the range of irradiation temperatures where this could be a concern. It is known high-dose ion irradiation can significantly suppress void nucleation. Future neutron irradiation in the 500–600℃ range (without considering the temperature shift) is needed to determine the onset of accelerated void swelling (possibly at lower dose).

Nanoindentation measurements show that the irradiation hardening decreases with increasing temperature. Microstructure-property correlation shows that the measured hardening at low dose (∼5 dpa) was mostly contributed by Frank loops at temperatures above 400℃ and network dislocations at 300℃.

T91 and G92 are both Fe–9Cr ferritic/martensitic alloy. G92 is optimized composition and heat treatment for improved performance in nuclear applications. The chromium content of T91 and G92 is close to the α–α' phase boundary. Irradiation hardening in ion-irradiated T91 and G92 is largely due to dislocation loops and network dislocations. The dislocation structure evolution was characterized by TEM during in situ 1 MeV Kr^{++} irradiation at 300, 400, and 500℃. At 500℃, the loop density at 1–3 dpa is significantly lower and the loops are dominantly $\langle 100 \rangle$ type. The loops at 400℃ are a mixture of $\langle 100 \rangle$ loops and $\langle 111 \rangle$ loops. The changes in yield strength were calculated at different doses and temperatures based on the microstructure observations. Nanoindentation measurements on bulk-irradiated specimens show that T91 and G92 have similar hardening behavior. The temperature dependence and dose dependence shown by nanoindentation measurements are consistent with the typical hardening behavior of neutron-irradiated F/M steels.

In summary, radiation-induced microstructural and mechanical property modifications in proposed advanced structural alloys were systematically investigated in this program. The results and discussions advance the understanding of the material performance under extreme irradiation environment. The results of our accelerated ion beam irradiation also serve as critical reference for further neutron irradiation campaigns. Based on current findings, we are making several recommendations for future irradiation studies of A709 and G92 in the following section.

Recommendations for future irradiation studies of A709 and G92

For ion-irradiated A709, the results of the current study show that there are significant irradiation-induced microstructural changes at temperatures between 300 and 600℃ which could significantly influence the alloy performance in service. These include: Frank loop formation and resulting hardening, major precipitation effects (e.g. matrix $M_{23}C_6$), major alloying element segregation effects (e.g. Ni-Si cosegregation to multiple defect sinks like dislocations, loops and precipitates) and void swelling. It is well established that, due to the higher dose rates in heavy ion irradiation studies, the rates (i.e. the dose) at which some of these effects form can be both accelerated (i.e. form at lower doses) and can shift in temperature (typically to higher temperatures).

Ferritic/martensitic G92 in optimized heat-treatment condition was shown to have similar, or maybe somewhat better irradiation-resistance properties compared to T91. It appears that the compositional control and heat treatment improvements could make G92 better qualified for elevated temperature application in sodium cooled fast reactor applications than other current versions of the Fe–9Cr class of alloys. This should be confirmed by a future neutron irradiation campaign on this alloy.

Future neutron irradiation campaigns on A709 and G92 should concentrate on these radiation-induced changes over a similar temperature range examined here: 300 to 600℃, to doses up to and beyond the 10 or 20 dpa anticipated for the total reactor life of the structural material applications. It is critical (especially for A709) to perform systematic post-irradiation examiniation on the possible radiation-induced microstructural and mechanical property modifications, in order to compare with current ion irradiation results and elucidate the difference of ion versus neutron irradiation.

The observed microstructural changes will affect mechanical properties and also potentially affect sodium corrosion resistance, so future neutron irradiation should also include reasonable scale tensile, fracture toughness and irradiation creep tests, to characterize potential changes (degradation) in materials structural properties. Comparisons to the significant data and literature on neutron irradiated 316-type stainless steels could confirm the superiority of A709 for SFR long-term structural applications. For G92, additional emphasis should be placed on characterize lower temperature ductility loss due to irradiation exposure.

ACKNOWLEDGMENTS

This work was supported by the US DOE Office of Nuclear Energy's Nuclear Energy University Program (NEUP) under Contract No. DE-NE0008291.

The A709, 316H, and G92 materials are provided by Oak Ridge National Laboratory. The T91 material was provided by Los Alamos National Laboratory.

The IVEM *in situ* TEM irradiation experiments were supported by the U.S. Department of Energy, Office of Nuclear Energy under DOE Idaho Operations Office Contract DE-AC07-051D14517 as part of a Nuclear Science User Facilities experiment. We would like to thank the staff members, Dr. Mark Kirk, Pete Baldo, Ed Ryan, and Dr. Jing Hu, of the IVEM-Tandem facility at Argonne National Laboratory, for their help and and support on the IVEM experiments.

The FIB, SEM, (S)TEM experiments were carried out in part in the Frederick Seitz Materials Research Laboratory Central Facilities, University of Illinois.

The APT experiments were conducted at the Center for Nanophase Materials Sicences (CNMS) at Oak Ridge National Laboratory (ORNL). The CNMS is a DOE Office of Science User Facility. We would like to thank Dr. Jonathan Poplawsky and Dr. Wei Guo at CNMS for their help with the APT experiments and discussions on the experiment results.

SUPPORTED AND CONTRIBUTING STUDENTS

Xiang Liu, Victoria Riso, Huan Yan, Donghee Park, Kuan-Che Lan (now postdoc at UNLV)
University of illinois at Urbana-Champaign

Jonathan Gigax (now postdoc at LANL)
Texas A&M University

David Krumwiede
University of California, Berkeley

1. PROGRAM OBJECTIVES AND IMPACT

This program is designed to provide a basis for designing a neutron irradiation campaign for two advanced, irradiation tolerant alloys. The approach is to develop substantive correlations between neutron and ion irradiation effects in microstructural evolution, and to assess the influence of these microstructural modifications on degradation of mechanical properties. The two advanced alloys are optimized Grade 92 and Alloy 709, both developed for improved resistance to irradiation effects. This research program will: (1) establish ion-to-neutron irradiation correlations between available neutron-irradiated reference alloys (Grade 91, Grade 92 and NF709) and the ion irradiations on these materials (to be performed in this program), and (2) to use these correlations to provide a basis for estimating neutron performance of the optimized Grade 92 and Alloy 709 materials. Neutron irradiation results for the reference alloys (Grade 91, Grade 92 and NF709, as well as the base materials, are available from a current, ongoing DOE program. The new insights developed here will both provide a firm basis for the prediction of neutron irradiation response based on ion irradiation results and a methodology to design a neutron irradiation campaign for the optimized Grade 92 and Alloy 709 materials.

The alloys for study in this program, optimized Grade 92 and Alloy 709, are promising candidates for future application in advanced sodium-cooled fast reactors. The proposed research will focus on a unique set of ion-irradiation conditions of these alloys that directly compare with available neutron-irradiation data. Appropriate models will be established to accurately estimate the microstructural modifications and the mechanical property degradation in neutron-irradiated advanced alloys based on ion irradiation data. The effects of irradiation-induced microstructural evolution on mechanical properties will also be quantitatively analyzed to better predict the performance of the optimized alloys for prospective advanced fast reactor applications, and to establish the parameters of a neutron irradiation campaign to verify their performance.

During the course of this program, the emphasis on materials radiation performance evaluation shifted toward a balance between G92 and Alloy 709 to put greater emphasis on Alloy 709. It also became clear that useful comparisons that might have existed with neutron irradiated NF709 did not turn out to be as meaningful as first thought due to differences in composition and pretreatment conditions between the older NF709 alloy and the new enhanced Alloy 709. These influences on the research program direction will be clear in the

following technical report. The work performed under this program provided very useful information about and insight into the irradiation performance of the two enhanced alloys, G92 and Alloy 709, which will be an important part of constructing a meaningful, future neutron irradiation campaign, as intended.

2. BACKGROUND

2.1 Materials challenges for advanced reactors

As an indispensable part of clean energy, light water reactor (LWR) based nuclear power currently provides over 11% of the world's electricity. After the Fukushima accident, efforts are being made to improve the safety of LWR technology using accident-tolerant fuels (ATF), or to develop advanced reactor systems with enhanced safety and efficiency features. All these improved attributes rely on the materials research and development. The advanced reactors call for resilient structural materials that can withstand harsh reactor environment such as high temperature, corrosion, and most importantly, high dose fast neutron irradiation [1]. Fig. 2.1 shows the temperature and dose ranges for various nuclear reactors [2]. Compared to current LWRs, All advanced reactors are designed to operature at higher temperatures, and most of them require much higher radiation exposures.

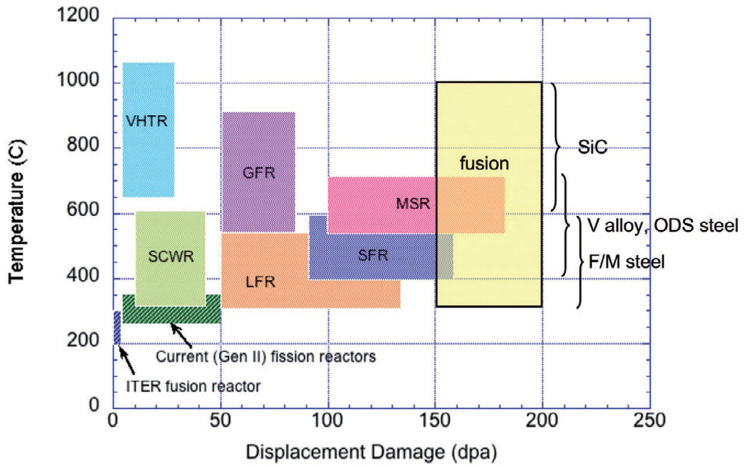

Figure 2.1: Temperature and dose ranges for various nuclear reactors [2].

Neutron irradiation damage represents one of the biggest challenges for reactor structural materials. Upon irradiation, the atoms in metals and alloys undergo successive displacements and point defects are created far exceeding

the equilibrium concentrations. The material system is driven into thermodynamic nonequilibrium and the microstructure can be modified in many ways: dislocation loops are formed due to the collapse of the interstitial-rich cascade shell, the accumulation of vacancies leads to the nucleation of voids, the preferential coupling between alloying elements and the defect fluxes results in the elemental segregation at defect sinks, the stability of precipitates is strongly impacted by displacement cascades and radiation-enhanced diffusion, etc.

The radiation-induced microstructure modifications have huge impacts on the material properties, which set the boundaries on reactor operation conditions and lifetime. No matter it is the life extension of current LWRs, or the development of advanced reactors, we need to understand how the materials are degraded during service and what engineering methods could be adopted to suppress the degradation processes. To achieve higher energy efficiency and cost reduction goals, advanced reactors should be optimized so that the materials for each structural component can meet the design requirements and are also the most economic. It is therefore necessary to have a thorough understanding of the radiation effects in multiple alloy systems, so that the bottleneck of structrual components could be identified and the most appropriate materials could be chosen for specific structural applications.

2.2 Radiation effects in austenitic alloys

Austenitic stainless steels are widely used in nuclear reactors. For instance, in pressurized water reactors (PWRs), austenitic stainless steel 304 is used for core structurals and piping, austenitic stainless steels 308 and 309 are used for vessel cladding [3]. In fact, most of the core structural materials are austentiic stainless steels, due to their excellent aqueous corrosion resistance at high temperatures [3].

Neutron irradiation produces high-density clustered defects that lead to significant hardening at low temperatures ($\sim$0.35 T_M) [3]. The most representative clustered defects in austenitic stainless steels are Frank faulted loops. The habit planes of Frank loops are $\{111\}$ planes and the Burgers vectors are of $1/3\langle 111\rangle$ type. Figs. 2.2 (a) and (b) show the Frank loops in neutron-irradiated 25% cold-worked (CW) Ti-modified austenitic stainless steel 316 (or prime-candidate alloy, PCA) imaged using satellite streaks and weak-beam dark-field (WBDF), respectively [4].

At intermediate temperatures, void swelling becomes one of the most concerning radiation effects for austenitic stainless steels, especially at high doses. Fig. 2.3 shows the swelling data of austenitic stainless steels. The void swelling can be roughly divided into two regimes: the low-swelling transient regime characterized by void nucleation and/or initial growth at low doses, and the steady-state regime dominated by void growth at higher doses. The steady-state swelling rate in austenitic stainless steels is typically around 1%/dpa.

Besides void swelling, radiation-induced segregation and precipitation also occurs at intermediate temperatures. For example, Ni_3Si (γ') is a radiation-

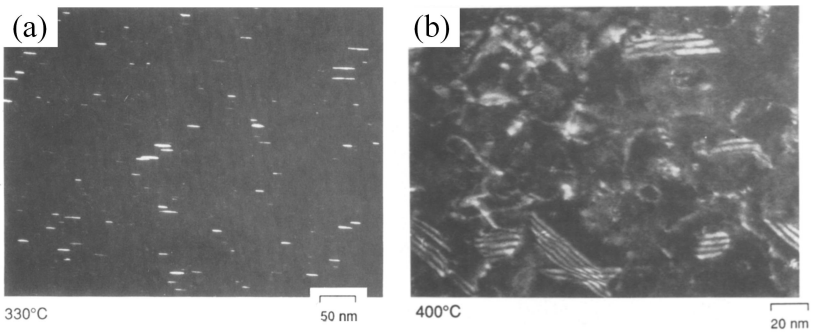

Figure 2.2: Frank loops in CW PCA steel neutron-irradiated to 7.4 dpa and 130 appm He: (a) TEM DF image using $\langle 111 \rangle$ satellite streaks near $\mathbf{g}_{200}$ showing the Frank loops at 330℃, and (b) TEM WBDF image showing the Frank loops at 400℃ [4].

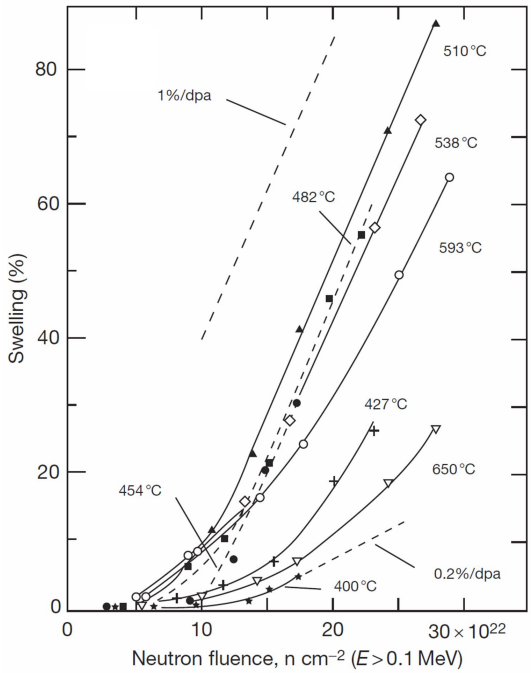

Figure 2.3: Swelling of cold-worked austenitic AISI 316 irradiated in EBR-II [5].

induced phase previously found in neutron-irradiated austenitic stainless steel 316 [4, 6–9]. Fig. 2.4 shows the dose and temperature regime in which γ' is expected in 20% CW austenitic stainless steel 316. Previous studies also suggested that the formation of γ' phase can be influenced by many factors, such as thermomechanical pre-treatment and He/dpa ratio [8]. It was found that γ' form more rapid and also in greater amounts in CW rather than solution-annealed (SA) material [6, 7]. For DO-heat 316 irradiated at 500–550°C, γ' was found in fast-spectrum EBR-II reactor irradiation (0.5 appm He/dpa) but not in mixed-spectrum HFIR reactor irradiation (∼70 appm He/dpa) [8]. Fig. 2.5 shows the data on γ' precipitation in austenitic stainless steels with different heats irradiated at different reactors. The conditions (alloy composition, He/dpa ratio, temperature, dose) for γ' precipitation is still not well understood.

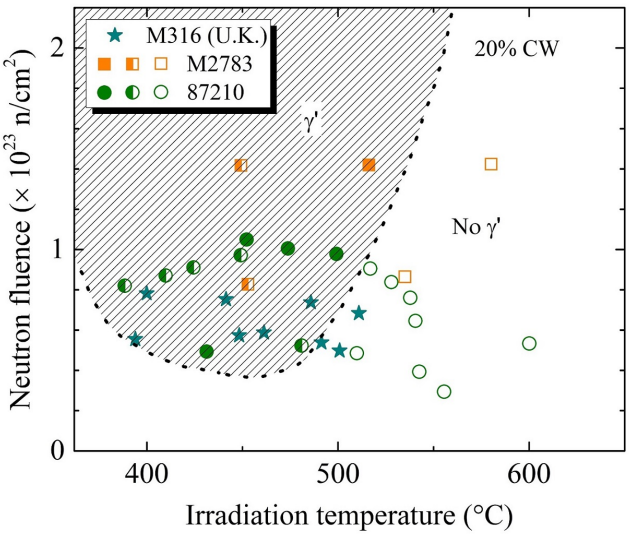

Figure 2.4: Irradiation conditions for γ' formation in 20% CW austenitic stainless steel 316, reproduced from ref. [10]. Solid symbols represent appreciable amount ($> 0.5\%$) of γ', half-filled symbols represent low volume fraction of γ', and open symbols represent no detectable γ'.

Finally, the harsh reactor environment can have much more complex impacts on the structural materials and the degradation mechanisms can be very complicated. An important and probably the most complex effect in austenitic stainless steels due to the combination of high-temperature water, mechanical stress, and neutron irradiation is irradiation-assisted stress corrosion cracking (IASCC), which is linked to water chemistry, radiation-induced Cr depletion at grain boundaries, irradiation hardening, and other radiation-induced modifications [14–16].

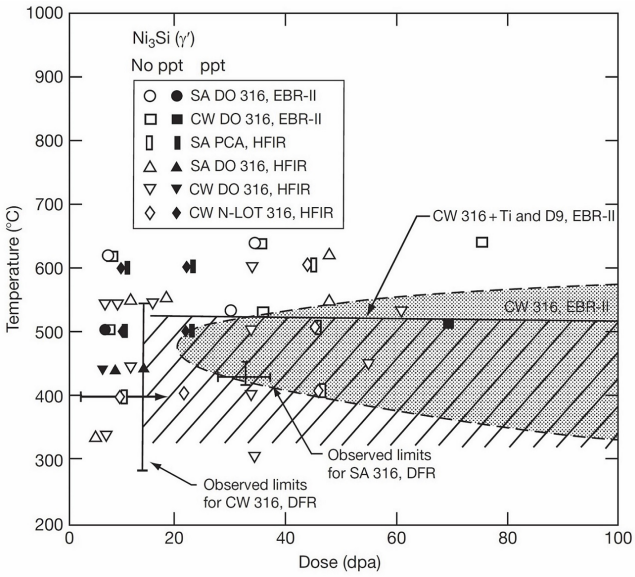

Figure 2.5: Radiation-induced γ' in various austenitic stainless steels [11]. The shaded region is taken from ref. [7], and the lined region are based on data from refs. [12, 13].

2.3 Radiation effects in ferritic/martensitic alloys

Ferritic/martensitic alloys are candidate materials for structural applications in advanced fission reactors and fusion reactors. Compared to austenitic stainless steels, F/M alloys suffer much less from void swelling. As an example, Fig. 2.6 shows the swelling data of F/M alloys neutron-irradiated in EBR-II and FFTF. It is easy to see that the void swelling in F/M alloys is orders of magnitude smaller than that of austenitic alloys. The steady-state swelling rate of F/M alloys is around 0.2%/dpa.

Besides superior void swelling resistance, F/M steels also have higher thermal conductivity, lower thermal expansion coefficients, and lower cost. High chromium (9–12 wt.%) F/M steels are of perticular interest due to their excellent resistance to swelling and irradiation creep [17].

For high chromium F/M steels, the most concerning radiation effect is the degradation in mechanical properties through irradiation hardening and embrittlement at low temperatues.

Irradiation hardening is represented by significant increase in yield strength, $\Delta\sigma_Y$. Fig. 2.7 shows the increase in yield strength of 3Cr, 9Cr, and A533B steels irradiated at low temperatures [18]. It can be seen that for irradiation at low temperatures ($\leqslant$ 160℃), significant hardening can occur as early as 0.01 dpa.

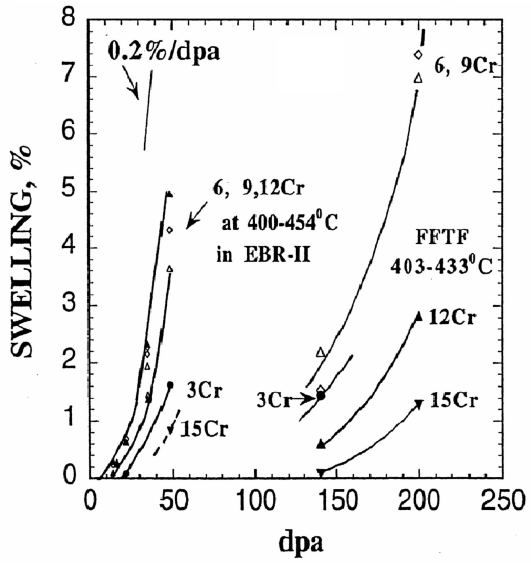

Figure 2.6: Swelling of Fe–Cr alloys irradiated in EBR-II and FFTF-MOTA [5].

The temperature dependence and dose dependence of irradiation hardening in various F/M steels is shown in Fig. 2.8 (a) and (b), respectively. It can be clearly seen that irradiation hardening strongly depends on the irradiation temperature, and almost no hardening was observed for temperatures above 500℃. Hardening also tends to saturate at around 10 dpa.

F/M steels are also susceptible to ductile-to-brittle transition. Low temperature irradiation can induce significant increase in the ductile-to-brittle transition temperature (DBTT). Fig. 2.9 (a) shows the Charpy imact curves of HT9 (12Cr–1MoVW), suggesting that the fracture toughness is significantly reduced after irradiation and the DBTT increased by over 150℃. Fig. 2.9 (b) shows the change in ductile-to-brittle transition temperature (ΔDBTT) as a function of the chromium content. It is easy to see that the minimum ΔDBTT occurs around 9%Cr, which is one reason why 9Cr F/M steels are of particular interest for advanced reactor applications.

Irradiation hardening and embrittlement is related to radiation-induced microstructural modifications such as the buildup of dislocation loops and the precipitation of new phases [19, 22]. In α-iron and Fe-base body-centered cubic (BCC) alloys, $a_0\langle 100\rangle$ loops are produced by irradiation [23–32], in addition to the typical $a_0/2\langle 111\rangle$ loops found in other BCC systems. Previous studies have also found that irradiation temperature has significant impacts on the stability of $a_0/2\langle 111\rangle$ loops with respect to $a_0\langle 100\rangle$ loops [33]. Fig. 2.10 shows the dislocation loops in neutron-irradiated α-iron [34]. As shown in Fig. 2.10 (a), mobile $a_0/2\langle 111\rangle$ loops are produced at lower temperature and they tend to decorate pre-existing dislocations, whereas in Fig. 2.10, sessile $a_0\langle 100\rangle$ loops

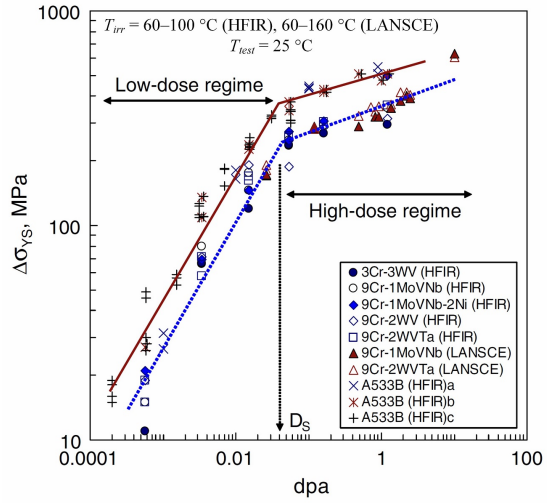

Figure 2.7: Hardening of 3Cr, 9Cr, and A533B steels irradiated at low temperatures [18].

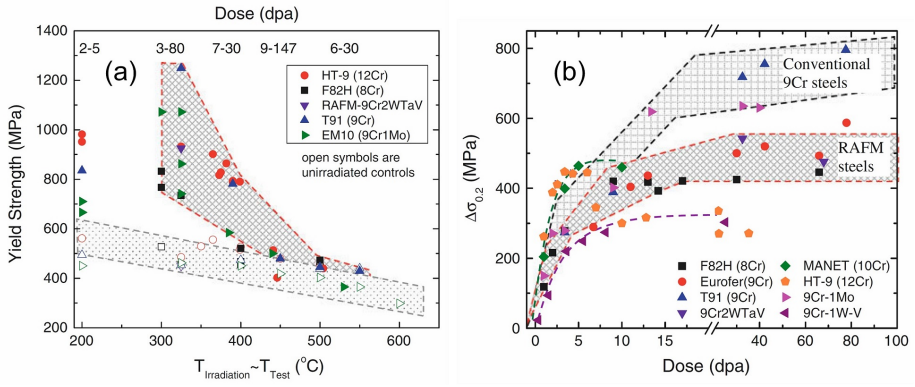

Figure 2.8: Irradiation hardening of various F/M steels: (a) temperature dependence of yield strength σ_Y before and after irradiation, and (b) dose dependence of $\Delta\sigma_Y$ at irradiation temperatures < 350°C (for HT9, $T_{test} \sim T_{irr} =$ 360–400°C) [17].

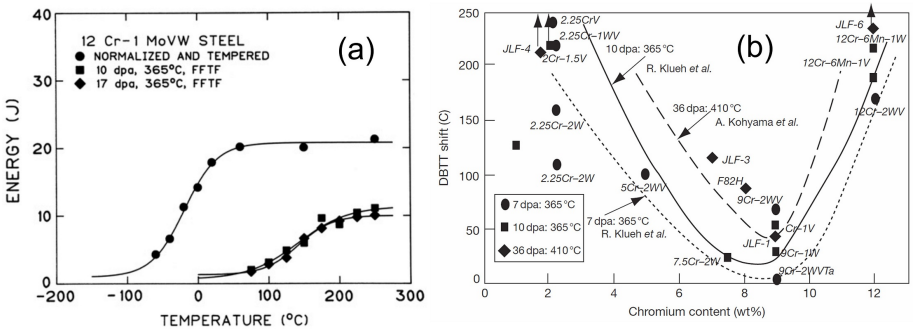

Figure 2.9: Irradiation embrittlement and DBTT shift in irradiated F/M steels: (a) Charpy imact curves of Sandvik HT9 [19], and (b) effect of chromium content on the DBTT shift of various F/M steels neutron-irradiated in FFTF [20, 21].

become dominant at higher temperature and the spatial distribution is more uniform.

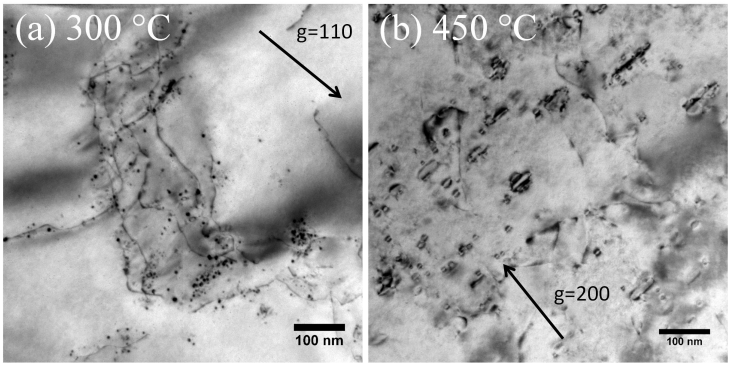

Figure 2.10: Dislocation loops in α-iron neutron-irradiated to 1 dpa at (a) 300℃, and (b) 450℃ [34].

Cr-rich brittle α' precpitation is closely related to the embrittlement of high chromium F/M steels irradiated at low temperatures (below 500℃). Standard (CALPHAD) Fe–Cr phase diagram indicates very low solubility limit, which was disproved by theoretical predictions, density functional theory (DFT) calculations, and experimental data [35–37]. The actual phase boundary is roughly located at 8–9% Cr for temperatures below ∼450℃ [35].

Recent studies have shown that the α' precpitation is a radiation-enhanced process [38–42], and the α' precpitates could be influenced by the cascade damage during irradiation [42]. A previous study on electron-irradiated Fe–15Cr has shown that without cascade damage, radiation greatly enhanced the α' precipitation process (shown in Fig. 2.12), and the α' precipitates reached thermodynamic equilibrium Cr concentration (96 at.%Cr) at around 0.7 dpa.

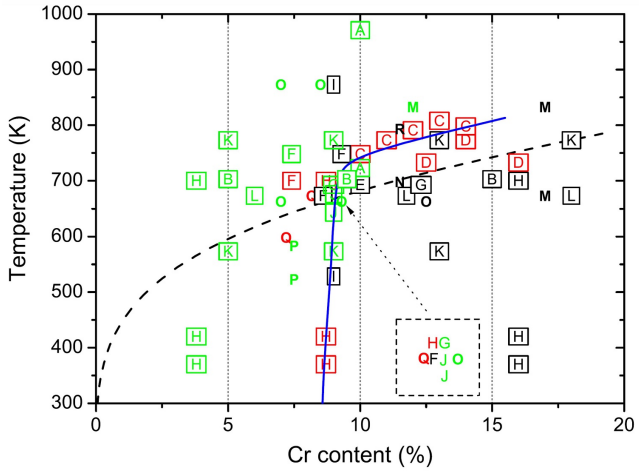

Figure 2.11: α' phase boundary in the Fe-rich part of the Fe–Cr phase diagram: dashed line is CALPHAD result, points are experimental data showing Cr ordering (green), precipitation (black), and suggested phase boundary (red). Solid blue line is the phase boundary based on experimental data [35].

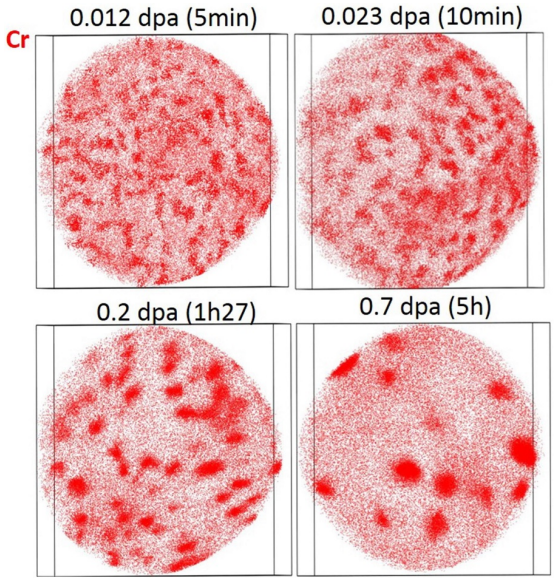

Figure 2.12: α' precipitation in electron-irradiated Fe–15Cr [40].

The cascade damage becomes important for heavy ion irradiation, the dose rate of which is typically 1000–10,000 higher than neutron irradiation. In fact, many heavy ion irradiation studies using high dose rates ($\geqslant 10^{-3}$ dpa/s) failed to find any α' precipitates in irradiated Fe–Cr alloys. Only recently, a study employing low dose rates (10^{-5}–10^{-4} dpa/s) heavy ion irradiation observed α' precipitates [42] with compositions much lower than phase diagram predictions [42]. Fig. 2.13 clearly shows the dose rate effect on the α' precipitates in irradiated Fe–18Cr alloy.

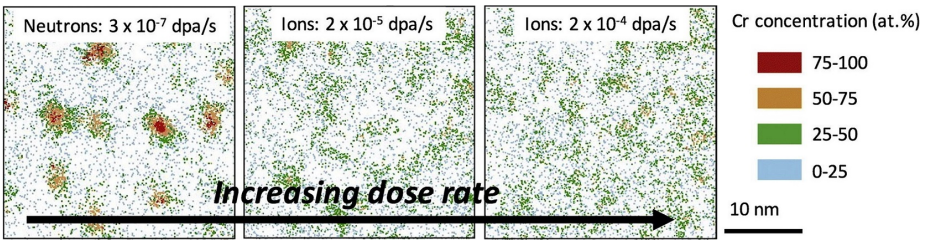

Figure 2.13: Dose rate effect on the α' precipitation in neutron/ion irradiated Fe–18Cr alloy [42].

2.4 Investigated Materials

This study aims to cover the radiation response of several different types of advanced alloys, including austenitic stainless steels Alloy 709 (A709) and 316H, F/M steels T91 and G92. Table 2.1 lists the nominal chemical compositions of the alloys investigated in this study [43, 44].

Table 2.1: Chemical compositions of the materials in this study (in wt.%).

Material	Fe	Cr	Ni	C	W	Al	Ti	V	Mn	Si	Mo	N	Nb	Co	B	O
A709	bal.	19.80	25.09	0.067	–	–	<0.01	–	0.90	0.40	1.50	0.15	0.26	–	0.0043	–
316H	bal.	16.23	10.12	0.045	–	0.004	0.002	0.06	1.42	0.65	2.09	0.053	0.014	0.279	0.004	–
T91	bal.	9.24	0.16	0.089	–	0.002	0.002	0.21	0.47	0.28	0.96	0.035	0.054	0.019	–	0.008
G92	bal.	8.9	–	0.09	1.8	–	–	0.2	–	–	0.4	0.05	0.08	–	–	–

The as-received A709 was taken from the Carpenter Technology Heat # 011502, Lot # H4. It was hot-processed (forged + rolled) and annealed at 1100 ℃, followed by water-quenching [43]. The as-received T91 was normalized at 1038 ℃ for 1 h, and air cooled, then tempered at 760 ℃ for 1 h and air cooled. The as-received G92 was normalized at 1130 ℃ for 0.5 h and tempered at 750 ℃ for 4 h and air cooled [44].

Fe–Cr–Ni ternary diagram is used to visualize the compositions of the investigated alloys. Fig. 2.14 shows the relative positions of investigated alloys, together with Incoloy 800H and type 304, 316 austenitic stainless steels.

The U.S. Advanced Reactor Technologies (ART) program have downselected one austenitic steel, A709, and one F/M steel, G92, as the primary candidate

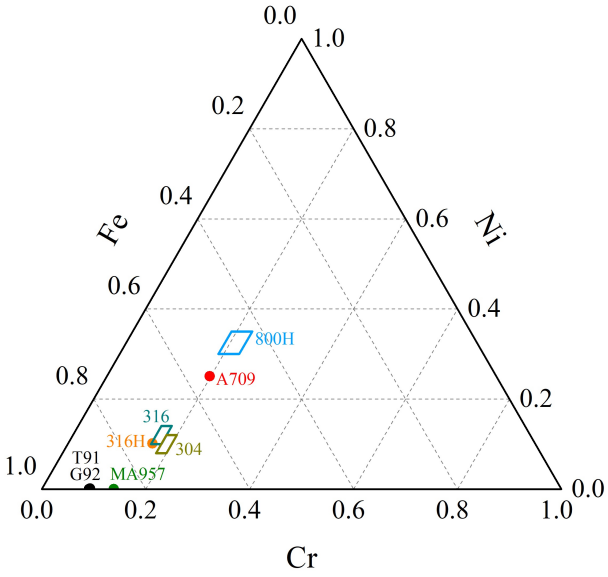

Figure 2.14: Fe–Cr–Ni ternary diagram showing the compositions of investigated alloys.

structural materials for the sodium-cooled fast reactor [45, 46]. As one of the six Gen-IV reactor concepts, sodium-cooled fast reactors show promising applications with demonstrated technological feasibility. Sodium-cooled fast reactors come with improved features such as high core power density, inherent safety, high thermal efficiency, low pressure, etc. However, the corrosive coolant, higher outlet temperature, and intense fast neutron irradiation poses challenges for structural materials in terms of sodium compatibility, creep resistance, radiation resistance, etc. In order to meet the individual requirements of each structural components and enhance the performance, safety, and affordability of sodium-cooled fast reactors, both austenitic stainless steels and F/M steels are being developed for different structural applications in sodium-cooled fast reactors. Both T91 and the downselected G92 are 9Cr F/M steels, and G92 has improved strength and creep resistance over T91 [46].

Austenitic A709 was selected mainly due to its superior high temperature strength, corrosion resistance, and creep properties. It is the improved version of a previous austenitic steel known as NF709 [47, 48]. Both alloys belong to the Nb/Ti-stabilized 20Cr–25Ni stainless steel family that was developed in the 1980s [49, 50]. A709 contains nano-sized Nb-rich MX precipitates and possesses improved creep resistance over traditional austenitic stainless steel 316H.

To date, the radiation response of A709 is unkown. Literature data on Nb/Ti-stabilized 20Cr–25Ni austenitic stainless steels and other austenitic stainless steels (e.g. type 316) is therefore a good starting point for this research.

Previous studies provide some general trend of the Frank faulted loops pro-

duced in neutron-irradiated austentic stainless steels. It was found that the density of Frank loops highly depdends on the irradiation temperature. Fig. 2.15 shows the temperature dependence of the Frank loop density in high dose ($>$ 10 dpa) neutron-irradiated austenitic stainless steel 316. It can be seen that for irradiation temperatures above 300℃, the Frank loop density drops rapidly with increasing temperature. Note also that cold working only seems to have a major effect for irradiation temperatures below 300℃. However, there are only a few studies in this temperature regime, so it is difficult to draw universal conclusion about the effects of cold work at lower irradiation temperatures.

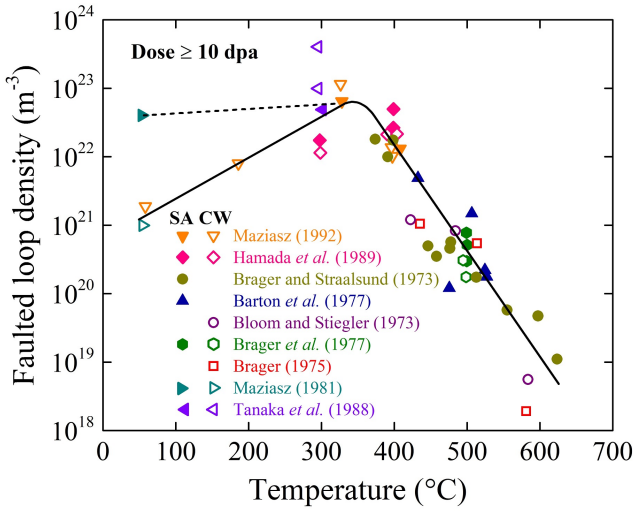

Figure 2.15: Temperature dependence of faulted loop density in high-dose neutron-irradiated type 316 austenitic stainless steel, reproduced form ref. [51]. Original data are from refs. [52–61].

Fig. 2.16 shows the dose dependence of the Frank loop density in austenitic stainless steels neutron-irradiated around 400℃. It is found that the Frank loop density saturates after about 3 dpa. Previous studies also indicate that for higher temperature ($\geqslant$ 450℃) irradiations, after saturation at relative low doses, the loop density started to decrease with increasing dose [51, 60–63].

Fig. 2.17 shows the time-temperature-precipitation (TTP) diagram of a 20Cr–25Ni–Nb stablized stainless steel with thermomechanical treatment (TMT). It can be seen that at sodium-cooled fast reactor relevant temperatures (550–650℃), $M_{23}C_6$ phase andd G-phase precipitate out at grain boundaries (GB) first, followed by matrix Nb(C,N) precipitation, and then GB σ-phase precipitation, and finally matrix G-phase and matrix σ-phase precipitation.

Similar to austenitic stainless steel 316, Ni,Si-rich precipitates were also found in neutron-irradiated 20Cr–25Ni–Nb stabilized austenitic stainless steel, and were thought to be of the γ' type [50]. Ni,Si-rich precipitates found in a 15% CW austenitic stainless steel 316 neutron-irradiated to 12 dpa at 359.85℃ con-

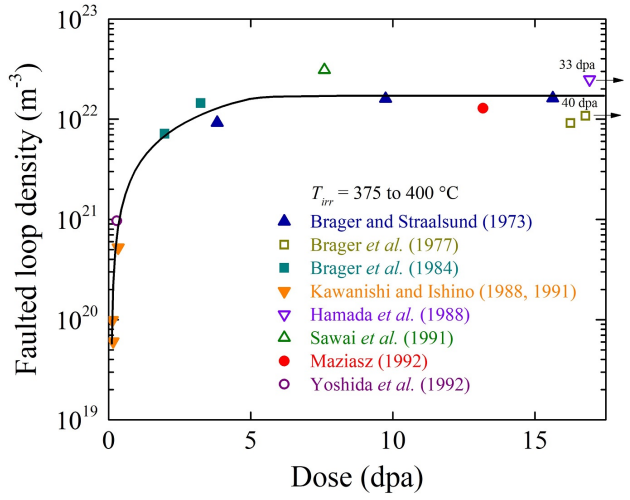

Figure 2.16: Dose dependence of faulted loop density in neutron-irradiated SA austenitic stainless steels, reproduced form ref. [51]. Original data are from refs. [52, 53, 60, 61, 64–68].

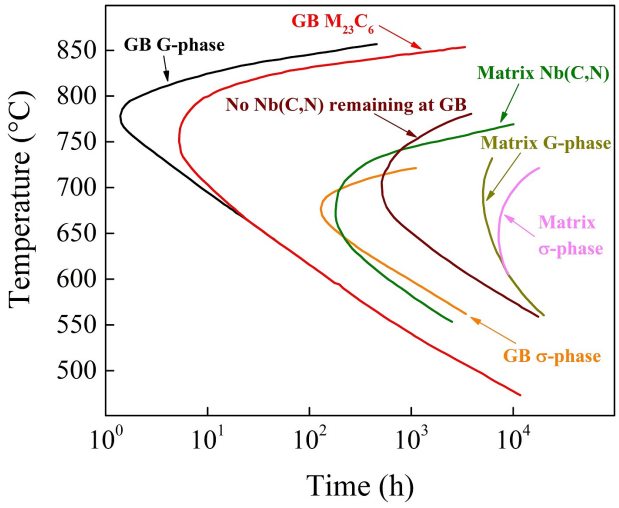

Figure 2.17: TTP diagram of a 20Cr–25Ni–Nb stablized stainless steel with TMT, reproduced from ref. [49].

tain ∼40 at.% Si and ∼50 at.% Ni, differing from the Ni_3Si stoichiometry [69]. Fig. 2.4 shows the temperature and dose range where the γ' phase is expected in neutron-irradiated 20% CW austenitic stainless steel 316.

3. METHODS

This study is focused on the radiation response, including the radiation-induced modifications in microstructure, microchemistry, and mechanical properties, of advanced alloys. Two types of irradiation were employed: *ex situ* bulk ion irradiation and *in situ* TEM thin foil irradiation. A series of microstructure characterization techniques, including transmission electron microscopy (TEM), scanning transmission electron microscopy (STEM), and atom probe tomography (APT), were used for microstructure characterization. Small-scale mechanical testing using nanoindentation was used for mechanical property measurements.

3.1 Irradiation experiments

For A709, 316H, T91, and G92 alloys, the as-received materials were cut into 3.0 mm in diameter circular discs by electrical discharging machining. Prior to *ex situ* ion irradiation, the disc specimens were mechanically thinned to around 100 µm and then twin-jet polished for ∼10 s using electrolyte containing 5% perchloric acid and 95% methanol at −30℃ and 23–24 V. For *in situ* TEM irradiation, the mechanically-thinned disc specimens were jet-polished to electron transparent with the same electrolyte under similar temperature and voltage conditions. The jet-polished TEM specimens were then plasma cleaned for ∼2 mins.

3.1.1 Dose calculations for ion irradiation

In this study, all the bulk ion irradiations of A709 and 316H used 3.5 MeV Fe^{++} ions and all the bulk ion irradiations of T91 and G92 used 1.0 MeV or 1.8 MeV Kr^{+} ions. All the *in situ* TEM irradiations used 1.0 MeV Kr^{++} ions. 3.5 MeV Fe^{++} ions were chosen because self-ions can better simulate neutron irradiation (in terms of recoil spectrum) and the energy can produce reasonably deep damage region for post-irradiation examination. For the *in situ* TEM irradiations, 1.0 MeV Kr^{++} were chosen because they are sufficiently energetic to pass through the TEM foil and produce displacement cascades similar to that of fast neutrons. The dose and dose rate for ion irradiation were calculated using the SRIM software with the quick Kinchin-Pease model [70, 71]. The displacement energy for Fe, Cr, Ni was 40 eV and 60 eV for Mo [72]. Fig. 3.1

shows the SRIM calculations of the displacement per atom (dpa) and injected ion fractions for A709, and Fe–9Cr alloys. The dose profile for 316H is almost identical to A709.

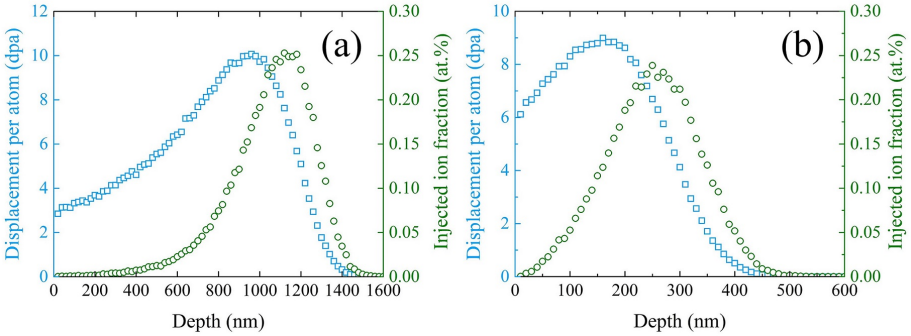

Figure 3.1: SRIM calculations of dpa and injected ion fractions for (a) 3.5 MeV Fe^{++} in A709, and (b) 1 MeV Kr^{++} in Fe–9Cr alloys.

Table 3.1 lists the dpa distribution for A709/316H irradiated by 3.5 MeV Fe^{++} to 10 peak dpa, and Fe–9Cr alloys irradiated by 1.0 MeV Kr^{++} ions to 9 peak dpa. For 3.5 MeV Fe^{++} ion irradiation, 200–400 nm region is often chosen to avoid the impacts due to surfaces effects, oxidation, and chemical modifications due to injected ions. The corresponding dose for 10 peak dpa sample in the 200–400 nm region is 4.24 dpa. For *in situ* irradiations, it is more meaningful to refer to the local dpa since the TEM specimen is typically 100 nm thick, much less than the depth of the peak dpa region. Unless otherwise stated (such as peak dpa), all the dpa in this report refers to local dpa. For Fe–9Cr alloys, 7 dpa and 9 peak dpa refers to the same irradiation.

Table 3.1: Local dpa for A709/316H irradiated to 10 peak dpa by 3.5 MeV Fe^{++} and Fe–9Cr irradiated to 9 peak dpa by 1.0 MeV Kr^{++}.

3.5 MeV Fe^{++} (10 peak dpa)		1.0 MeV Kr^{++} (9 peak dpa)	
Depth (nm)	Local dpa	Depth (nm)	Local dpa
0–200	3.30	0–100	7.27
200–400	4.24	100–200	8.74
400–600	5.64	200–300	6.37
600–800	7.77	300–400	1.73
800–1000	9.72	400–500	0.11
1000–1200	7.70		
1200-1400	1.87		

3.1.2 *Ex situ* bulk irradiation

For A709 and 316H, the *ex situ* bulk irradiations were carried out using a 1.7 MV Ionex Tandetron accelerator at Texas A&M University. The specimens

were irradiated by 3.5 MeV Fe^{++} ions at a peak dose rate of around 1.7×10^{-3} dpa/s to target doses of 10, 50, and 150 peak dpa. The ion fluence for 10 peak dpa is approximately 9.7×10^{15} ions/cm^2. For T91 and G92, the *ex situ* bulk irradiations were carried out using a Van de Graaff accelerator at the University of Illinois at Urbana-Champaign. The specimens were irradiated by 1.0 or 1.8 MeV Kr^+ ions at a dose rate of around 1.0×10^{-3} dpa/s. Table 3.2 lists the *ex situ* bulk irradiation matrix.

Table 3.2: *Ex situ* bulk irradiation matrix.

Material	Facility	$T_{irr.}$ (℃)	dose (peak dpa)	dose rate (dpa/s)	Ions used
A709, 316H	TAMU	400, 500, 600	10, 50	1.7×10^{-3}	3.5 MeV Fe^{++}
A709, 316H	TAMU	500, 600	150	1.7×10^{-3}	3.5 MeV Fe^{++}
T91	UIUC	400, 500	3.9	1.0×10^{-3}	1 or 1.8 MeV Kr^+
G92	UIUC	300, 400, 500	3.9, 19.3	1.0×10^{-3}	1 or 1.8 MeV Kr^+

3.1.3 *In situ* thin foil irradiation

All the *in situ* thin foil irradiation (or *in situ* TEM irradiation) experiments were carried out at the Intermediate Voltage Electron Microscopy (IVEM)-Tandem Facility, Argonne National Laboratory (ANL). The experimental setup is shown in Fig. 3.2. A Hitachi 9000 NAR electron microscope operated at 200 kV or 300 kV was used for TEM imaging. The incident ion beam was 30° to the electron beam and on average 15° to the foil normal. At ∼15° tilt, grains satisfying desired diffraction conditions were selected for TEM observations. The irradiation temperature was measured by a thermocouple attached to the heating cup of a double tilt heating sample holder and was kept within ± 3℃ during the irradiation. The ion flux was kept at 6.25×10^{11} ions/(cm$^2\cdot$ s).

The *in situ* thin foil irradiation matrix is listed in 3.3.

Table 3.3: *In situ* thin foil irradiation matrix.

Material	Facility	$T_{irr.}$ (℃)	Ion fluence (ions/cm^2)	dose (dpa)	dose rate (dpa/s)	Ions used
A709	IVEM	400, 500, 600, 700	1.8×10^{15}	3	1.0×10^{-3}	1 MeV Kr^{++}
T91	IVEM	300, 400, 500	4.2×10^{15}	7	1.0×10^{-3}	1 MeV Kr^{++}

The advantages of *in situ* thin foil irradiation are: (1) it allows microstructure observations while the specimen is being irradiated, so that the microstructure evolution can be real-time monitored; (2) the irradiation conditions (specimen orientation, temperature, dose, dose rate) can be very well controlled; (3) it is possible to track the microstructure evolution of exactly the same area at different dose levels, excluding the uncertainties due to averaging over different areas as in bulk irradiations.

However, it should be noted that irradiating a thin foil specimen can differ significantly from irradiating a bulk specimen, especially at elevated temperatures when surface effects beome dominant. *In situ* thin foil irradiation also

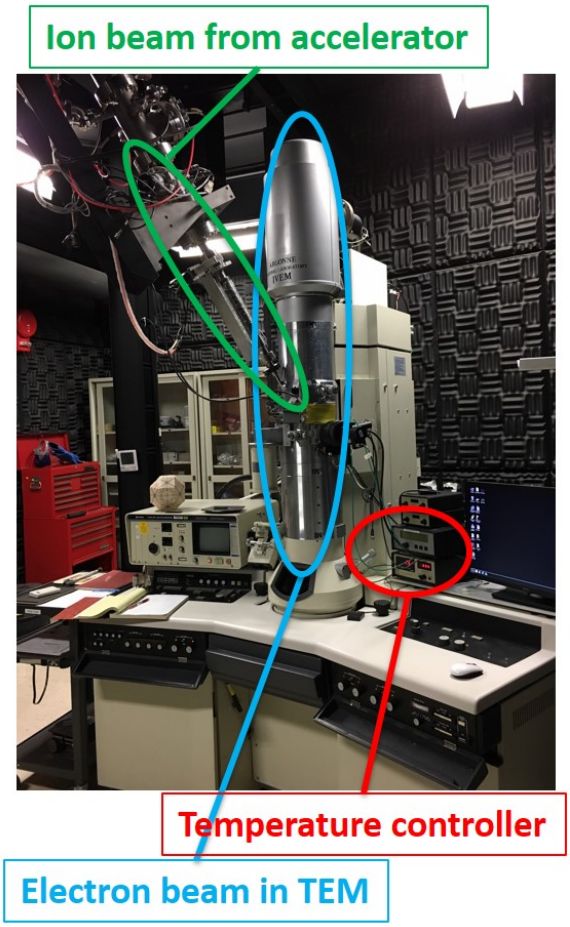

Figure 3.2: IVEM-Tandem facility for *in situ* thin foil irradiation.

requires high quality TEM specimens that have very clean surfaces, as any residual chemicals can lead to strong interactions at elevated temperatures and bring in artifacts.

3.2 Post-irradiation sample preparation using focused ion beam

Focused ion beam (FIB) lift-out was used to prepare TEM and APT specimens for post-irradiation examination (PIE). Fig. 3.3 shows the key steps during TEM lamella preparation using FIB. In order to protect the surface, electron beam Pt deposition (∼200 nm) was used prior to ion beam Pt deposition. To minimize FIB-induced damage inside the TEM lamella, 80 pA current of 30 keV Ga ions was used for final thinning, followed by cleaning with 5 keV Ga ions and final cleaning with 2 keV Ga ions for 1–3 mins.

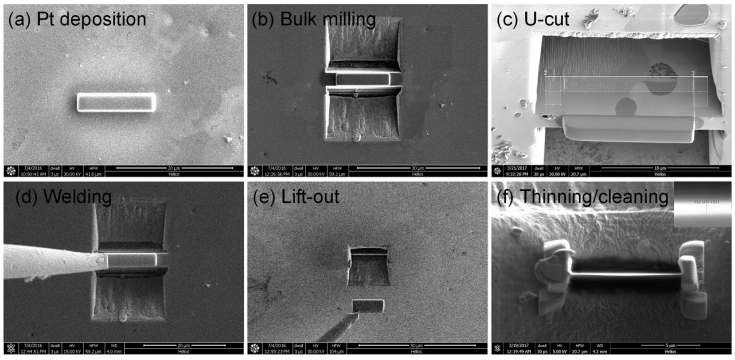

Figure 3.3: Illustration of the key steps during TEM lamella preparation using FIB.

For A709 and 316H, atom probe tips were prepared by FIB lift-out and annular milling using a FEI Nova 200 DualBeam FIB/SEM at the Center for Nanophase Materials Science (CNMS), Oak Ridge National Laboratory (ORNL).

3.3 Transmission electron microscopy

TEM was primarily used to characterize radiation-induced dislocation loops, voids, and precipitates. Kinematic bright-field (BF) and weak-beam dark-field (WBDF) were used for imaging dislocation loops in both body-centered cubic (BCC) and face-centered cubic (FCC) materials. For FCC materials, rel-rod dark-field was sometimes used for imaging Frank faulted loops. In addition, thickness fringes and/or convergent electron beam diffraction (CBED) was used for TEM specimen thickness determination [73].

TEM has been widely used for microstructure characterization owing to its powerful resolution down to sub-nm and also the ability to obtain diffraction information. Features in the nm to µm scale can be imaged using TEM. By tilting the specimen to specific orientations, desired diffraction conditions could be chosen to form images with proper contrast for the microstructure features of interest. For instance, $\mathbf{g}(3\mathbf{g})$ and/or $\mathbf{g}(5\mathbf{g})$ WBDF technique has been developed to image dislocations and stacking faults.

3.3.1 Loop habit plane determination

Radiation-induced dislocation loops can be well characterized by TEM. The conventional $\mathbf{g}\cdot\mathbf{b}$ analysis has been widely used to determine the Burgers vector of loops. The habit planes of loops can also be determined by comparing the loop orientation with respect to the diffraction vectors. This method can be used for loops that are large enough so that the orientation can be resolved.

Figs. 3.4–3.6 show the projections of loops lying on {111} planes, {110} planes, and {100} planes on to [011] plane, respectively. It is then easy to tell whether the habit planes of the loops are {111}, {110}, or {100} planes by comparing the TEM images with the predicted projections in Figs. 3.4 and 3.5.

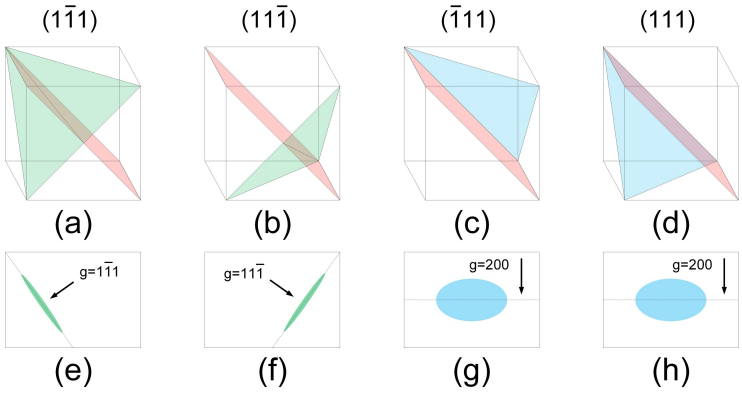

Figure 3.4: Illustration of loops lying on {111} planes imaged near [011] zone.

Alternatively, [001] zone can also be used to distinguish {111} loops from {110} loops. Fig. 3.7 and Fig. 3.8 show the projection of loops lying on {111} planes and {110} planes on to the [001] plane, respectively. The projection of loops lying on {100} on to [001] is trivial and is not shown here. Similarly, the habit planes of the loops can be distinguished by comparing with actual TEM images.

3.3.2 Thickness determination

In order to obtain quantitative information on the size and density of dislocation loops, voids, and precipitates, it is necessary to determine the specimen

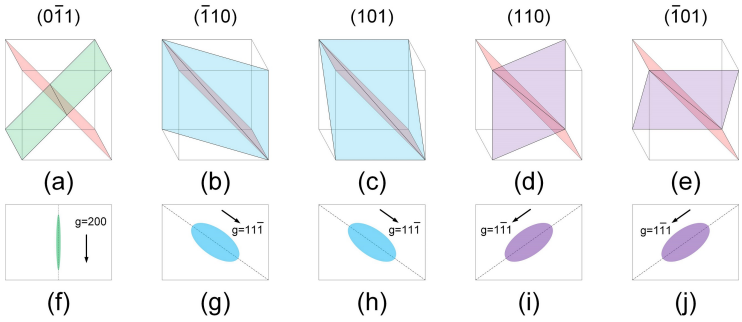

Figure 3.5: Illustration of loops lying on {110} planes imaged near [011] zone.

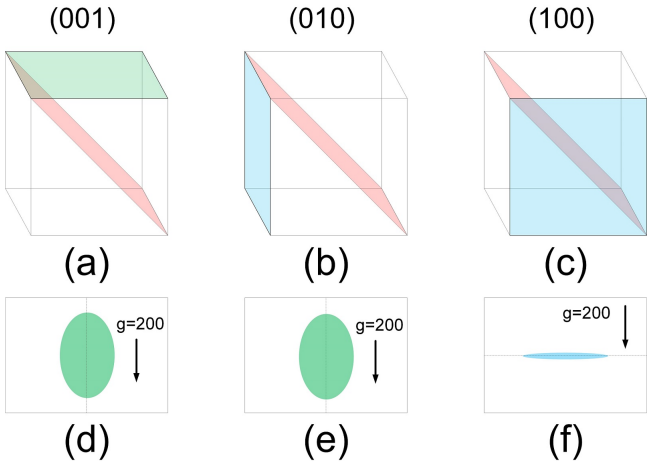

Figure 3.6: Illustration of loops lying on {100} planes imaged near [011] zone.

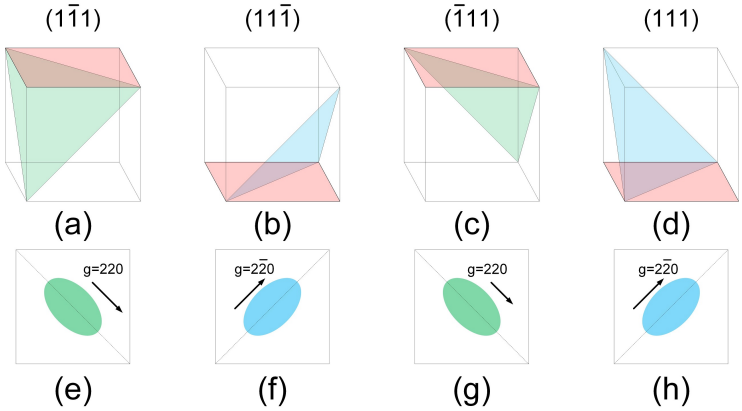

Figure 3.7: Illustration of loops lying on {111} planes imaged near [001] zone.

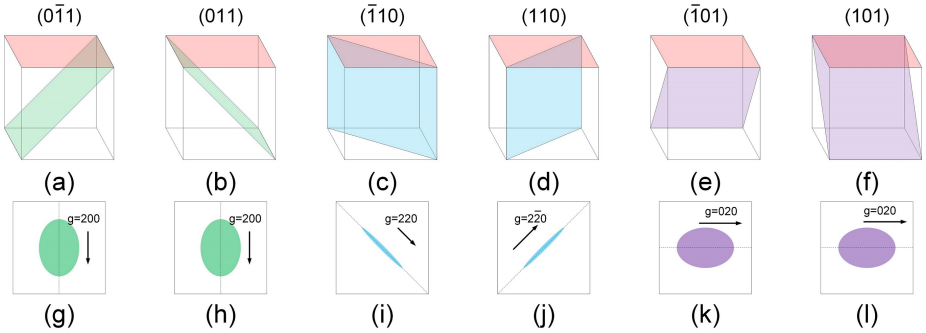

Figure 3.8: Illustration of loops lying on {110} planes imaged near [001] zone.

thickness. For wedge-shaped TEM specimens prepared by jet-polishing, thickness fringes are used for thickness determination.

For thickness fringes, the thickness increment t between two adjacent fringes is given by [73]:

$$t = (s_{eff})^{-1} = \frac{1}{s^2 + 1/\xi_g^2} \tag{3.1}$$

and

$$s = (n-1)\lambda/2d_{hkl}^2 \tag{3.2}$$

where ξ_g is the extinction distance for diffraction vector $\mathbf{g}$, λ is the electron wavelength, $n\mathbf{g}$ is where the Ewald sphere cuts the row of systematic reflections, and d_{hkl} is the spacing between $[hkl]$ planes, and s is the magnitude of excitation error. The t values for BCC ferritic alloys using $\mathbf{g}_{110}$ and $\mathbf{g}_{200}$ reflections can be found in ref. [34]. Here, the t values for FCC austenitic alloys are listed in Table 3.4. The extinction distances are taken from ref. [74].

Table 3.4: Thickness increment values for different diffraction conditions in austenitic alloys.

Diffraction condition	$\mathbf{g}_{111}$, (g, 5g)	$\mathbf{g}_{111}$, (g, 5g)	$\mathbf{g}_{200}$, (g, 5g)	$\mathbf{g}_{200}$, (g, 5g)
Voltage (kV)	200	300	200	300
λ (pm)	2.51	1.97	2.51	1.97
ξ_g (nm)	29.9	33.4	34.8	38.9
s (nm^{-1})	0.114	0.090	0.152	0.120
t (nm)	8.42	10.54	6.64	8.15

CBED was used mostly for FIB-prepared TEM lamellas, which are normally not wedge-shaped. In order to get the desired CBED pattern, the TEM specimen needs to be tilted to a proper two-beam condition with proper C2 aperture. Fig. 3.9 is a CBED pattern of A709 irradiated to 10 peak dpa at 500°C, obtained by tilting the specimen near [011] zone and exciting $\mathbf{g}_{31\bar{1}}$.

The equation for thickness determination using CBED pattern is given by

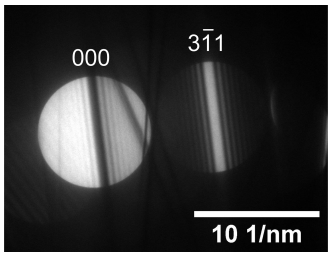

Figure 3.9: An example CBED pattern of A709 irradiated to 10 peak dpa at 500℃.

[73]:

$$\frac{s_i^2}{n_k^2} + \frac{1}{\xi_g^2 n_k^2} = \frac{1}{t^2} \tag{3.3}$$

where s_i is the deviation parameter for the i^{th} fringe, n_k is an integer decided during linear fitting, ξ_g is the extinction distance for diffraction vector $\mathbf{g}$. The deviation parameter s_i is given by:

$$s_i = \lambda \frac{\Delta\theta_i}{2\theta_B d^2} \tag{3.4}$$

where $2\theta_B$ is the separation of the 000 and hkl disks, λ is the wavelength of the electron beam, and d is the d-spacing of hkl planes.

From Eq. 3.3 it is easy to see that we should expect a linear line if we plot s_i^2/n_k^2 vs $1/n_k^2$. Fig. 3.10 shows the linear fitting result obtained based on the CBED pattern in Fig. 3.9. The thickness is then determined to be 106.3 nm for the A709_10 peak dpa_500℃ specimen.

3.4 Scanning transmission electron microscopy

Unlike TEM that uses parallel electron beam, a STEM uses convergent beam. Since the electron probe is very small (sub-Å), STEM images are obtained by rastering the electron probe over a certain region of the specimen. By filtering out the Bragg diffracted electrons, the high angle annular dark field (HAADF) detector is often used to form Z-contrast (or mass-thickness contrast) HAADF images. Combined with energy dispersive X-ray spectroscopy (EDS) and/or electron energy loss spectroscopy (EELS), the chemical information could be obtained together with the HAADF images. In this study, STEM-EDS was primarily used to characterize radiation-induced segregation and precipitation in austenitic stainless steels. High resolution STEM (HRSTEM) was used for precipitate identification. The STEM-EDS experiments were performed on a JEOL 2010F EF-FEG STEM operated at 200 kV. The HRSTEM experiments were performed on a JEOL JEM-2200FS operated at 200 kV.

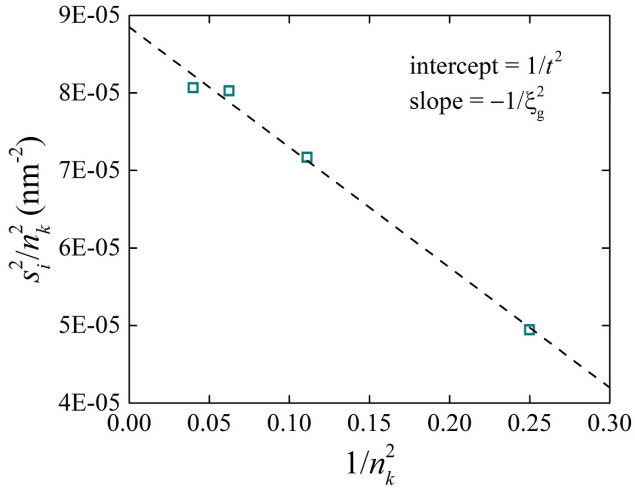

Figure 3.10: The linear fitting of s_i^2/n_k^2 vs $1/n_k^2$ gives a thickness of 106.3 nm for the A709_10 peak dpa_500℃ specimen.

3.5 Atom probe tomography

The atom probe tomography is currently the only technique that can characterize both the 3D microstructure and chemical composition of materials. Fig. 3.11 is a schematic diagram of APT [75]. During an APT experiment, the atoms from the needle-shape specimen are ionized and then field evaporated. The ions are then collected by a position-sensitive detector. The x-y position is determined from the hit position on the detector and the z-position is determined from the evaporation sequence. Utilizing the time-of-flight (TOF) mass spectrometry, the ions are identified by their mass-to-charge ratio. Together, the 3D microstructure and chemical composition are obtained.

For A709 and 316H, the APT experiments were carried out on a CAMECA LEAP 4000× HR at the Center for Nanophase Materials Sciences, ORNL. The APT specimens were analyzed in the 200 kHz pulsed-laser mode at a specimen temperature of 50 K, and a focused laser beam energy of 50–85 pJ. Data analyses were performed using the CAMECA IVAS software.

3.5.1 Isosurface analysis

An isoconcentration surface (isosurface) is a surface that connects a designated concentration level in 3D. Isosurface is an effective way of visualizing the precipitates and elemental segregation. In this study, isosurfaces were used to characterize secondary precipitates and elemental segregation at defect sinks in irradiated specimens.

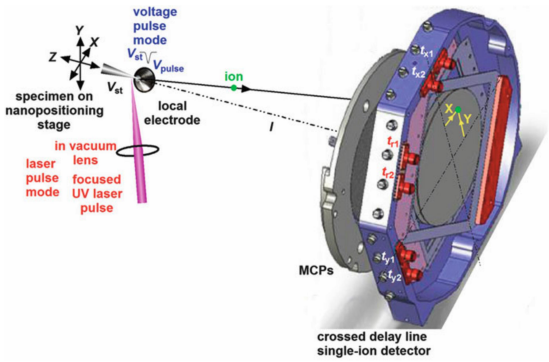

Figure 3.11: Schematic diagram of a local electrode atom probe [75].

3.5.2 Proxigram analysis

Proximity histogram (proxigram) is commonly used to quantify the composition of adjacent phases. An example is previous studies on the Cr concentration of the α' phase and the Cr concentration of the matrix in irradiated Fe–Cr model alloys. In this study, proxigrams were used to analyze the concentration of alloying elements at dislocation loops, composition of radiation-induced precipitates in ion-irradiated austenitic stainless steels.

3.6 Nanoindentation

Nanoindentation is widely used to study the mechanical properties of materials at sub-micron scale. The most common properties measured from nanoindentation experiments are hardness and elastic modulus.

In this study, the nanoindentation on austenitic stainless steels was carried out on a Hysitron TI 950 Triboindenter with a Berkovich tip under quasi-static mode. Displacement control with norminal maximum displacement of 200 nm or 300 nm was used for all measurements on unirradiated and ion-irradiated austenitic stainless steels. This depth was chosen as a compromise to reduce the impacts due to the size effects on shallow indents and the substrate effects on deep indents. In order to reduce statistical errors, multiple indents (10–16) with a separation of 30 µm were performed for each sample.

The nanoindentation on ion-irradiated F/M steels was carried out at UC Berkeley under either quasi-static mode or continous stiffness measurement (CSM) mode. For quasi-static mode, displacement control mode was used and multiple indents (> 10) were performed for each sample to reduce the statistical errors.

4. RADIATION RESPONSE OF AUSTENITIC STAINLESS STEEL A709

To understand the radiation response of A709, it is necessary to characterize the unirradiated microstructure, such as the grain size, initial dislocation density, and pre-existing precipitates.

Fig. 4.1 is a EBSD map showing the grain orientation of A709. The average grain size of A709 is about 20–40 µm.

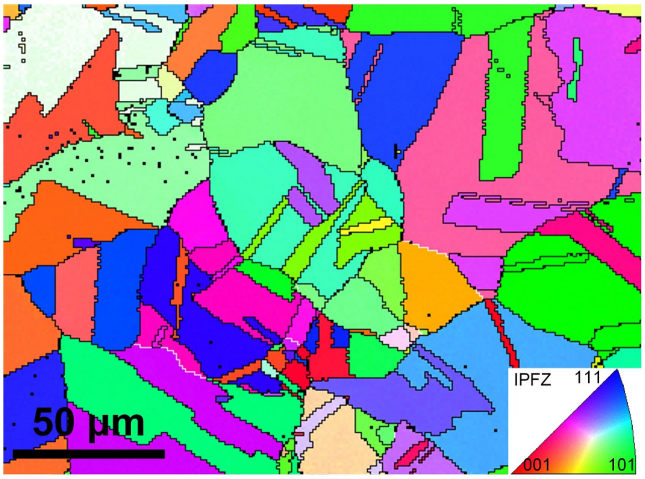

Figure 4.1: EBSD inverse pole figure of A709.

Some of the results of A709 will be compared with those of 316H, which is a Fe–16Cr–10Ni austenitic stainless steel widely used for elevated temperature applications. Figs. 4.2 (a) and (b) shows the dislocations in unirradiated A709 and 316H, respectively. It is easy to see that the initial dislocation density of 316H is orders of magnitude higher than that of A709. The dislocation density in unirradiated A709 is very low ($\sim 10^{12}$ m^{-2}).

The precipitates in the unirradiated Alloy 709 is shown in Fig. 4.3. Fig. 4.3 (a) is a high-angle annular dark-field (HAADF) STEM image showing the distribution of MX precipitates, some of which are indicated by the arrows. The MX precipitates are much heavier than the matrix, and they can be easily

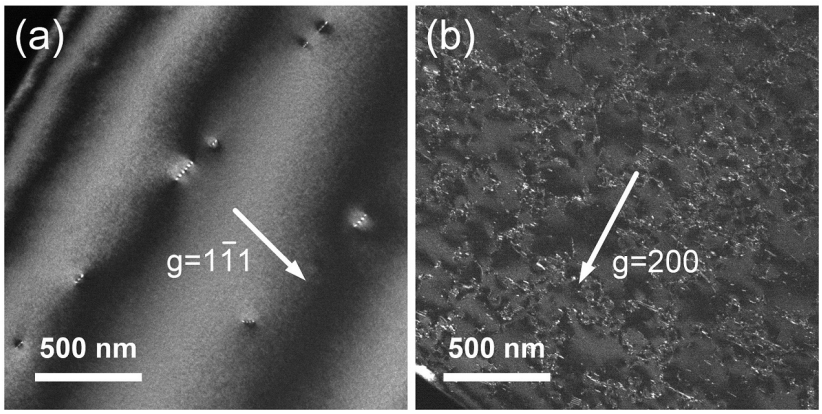

Figure 4.2: TEM WBDF image showing the dislocations in (a) unirradiated A709, and (b) 316H, respectively.

identified from the darker background in the Z-contrast HAADF STEM images. Fig. 4.3 (b) shows the representative EDS spectrum of the MX precipitates. The enrichment of Nb can be clearly seen. The EDS gives an Nb content of 69.7 wt.%, and the actual value should be even higher since the matrix containing Cr, Fe, and Ni also contributes to the measured EDS result.

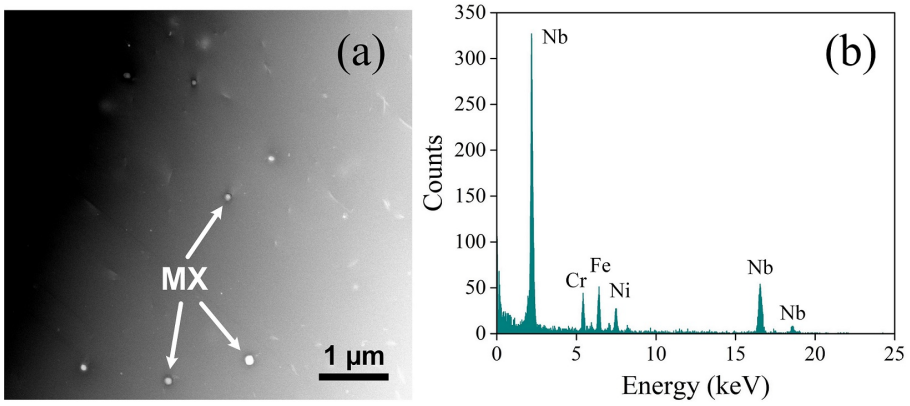

Figure 4.3: Unirradiated A709: (a) STEM HAADF image showing the MX precipitates, and (b) EDS spectrum of a MX precipitate.

APT was used to check if there is any clustering in the unirradiated A709. Fig. 4.4 shows the reconstructed atom maps of unirradiated A709. It is easy to see that the elements are uniformly distributed and little clustering was found.

The chemical composition (VIM Final) certified by Carpenter in wt.% is converted to at.% and compared with APT measurement, and the results are tabulated in Table 4.1. It is easy to see that the APT measurement is basically

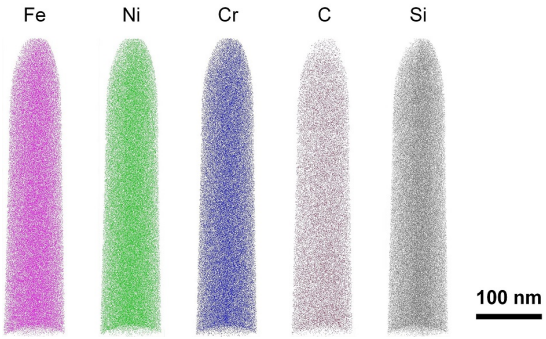

Figure 4.4: Reconstructed atom maps of unirradiated A709 showing little clustering.

consistent with Carpenter provided composition.

Table 4.1: Chemical composition (at.%) of unirradiated A709.

Element	Carpenter	APT
Cr	21.131	22.198
Ni	23.721	21.565
C	0.3096	0.4932
Mo	0.868	0.882
Si	0.790	1.031
Mn	0.909	0.968

4.1 Radiation-induced dislocation loops

4.1.1 *In situ* thin foil irradiation at 300℃

It is well known that in austenitic steels, the dislocation loops produced by irradiation are dominantly black-dots (∼2 nm) and larger Frank faulted loops. The black-dots are small clustered defects and become prevailing for low temperature irradiations. All the TEM characterization on bulk-irradiated A709 relies on the TEM sample preparation using FIB, and it is very hard to distinguish radiation-induced black-dots from FIB-induced damage. Therefore, in order to avoid possible artifacts from FIB-induced damage, the irradiation at 300℃ was carried out on a jet-polished TEM thin foil *in situ* with 1.0 MeV Kr^{++} ions using the IVEM facility. The Kr^{++} ions were sufficient energetic to pass through the thin foil, so that effects due to injected ions were avoided.

Fig. 4.5 shows the microstructural evolution of A709 irradiated by 1 MeV Kr^{++} ions up to 5 dpa at 300℃. It can be seen that black-dots occurred as early as 0.1 dpa, dislocation segements started to form at 0.55 dpa. Pre-existing dislocations were dissolved and uniform network dislocations formed at 3.0 dpa. The microstructure was basically unchanged from 3.0 dpa to 5.0 dpa. The final

microstructure is consist of uniform network dislocations and black-dots. No large Frank loops were observed.

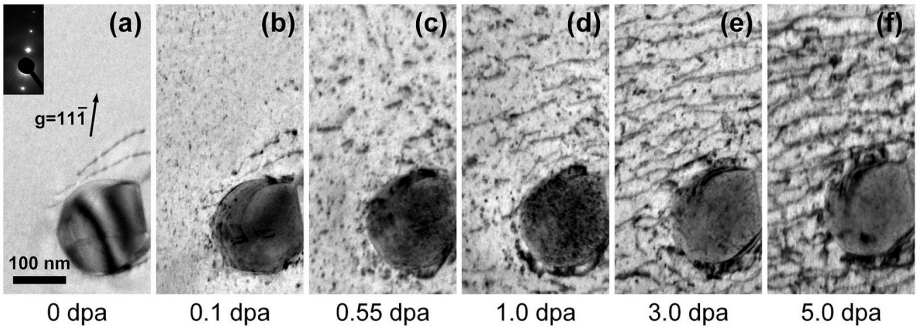

Figure 4.5: TEM kinematic BF images showing the microstructural evolution in A709 irradiated by 1 MeV Kr $^{++}$ ions up to 5 dpa at 300℃. The images were taken near [011] zone with $\mathbf{g}_{11\bar{1}}$ strongly excited.

4.1.2 *Ex situ* bulk irradiation at 400℃

At 400℃ and above, larger Frank loops become dominant and they can be easily distinguished from FIB-induced damage. In order to avoid the possible surface effects from thin foil irradiation, bulk-irradiation was employed and FIB-prepared TEM lamellae were used for the PIE work.

It is known that the habit plane of Frank loops are {111} planes and their Burgers vectors are of $a/3\langle 111\rangle$ type. Frank loops can be well characterized using the WBDF technique or the rel-rod dark-field technique [76, 77].

The dislocation loops in A709 irradiated to 10 peak dpa at 400℃ are shown in Fig. 4.6. The image was taken near [011] zone and all the loops are close to edge-on.

In order to verify that these loops are Frank loops, the orientation of the loops was then compared to the diffraction vectors. Fig. 4.7 is another set of TEM images taken near the peak damage region. It is easy to see that $\mathbf{g}_{11\bar{1}}$ is perpendicular to the loops marked by green arrows, $\mathbf{g}_{1\bar{1}1}$ is perpendicular to the loops marked by blue arrows, and $\mathbf{g}_{200}$ is perpendicular to the loops marked by yellow arrows. Recall that in the illustration shown Fig. 3.4, near [011] zone, loops that reside on $(1\bar{1}1)$ plane are perpendicular to $\mathbf{g}_{1\bar{1}1}$ diffraction vector and are close to edge-on, loops that reside on $(11\bar{1})$ plane are perpendicular to $\mathbf{g}_{11\bar{1}}$ diffraction vector and are close to edge-on, and loops that reside on $(\bar{1}11)$ or (111) planes are perpendicular to $\mathbf{g}_{200}$ diffraction vector and are elliptical. Therefore, the edge-on loops marked by green arrows are $(11\bar{1})$ loops, the edge-on loops marked by blue arrows are $(1\bar{1}1)$ loops, and the elliptical loops marked by yellow arrows are $(\bar{1}11)$ or (111) loops. In addition, the fault contrast of these loops indicate they are all faulted loops. Therefore, it is confirmed that they are Frank faulted loops.

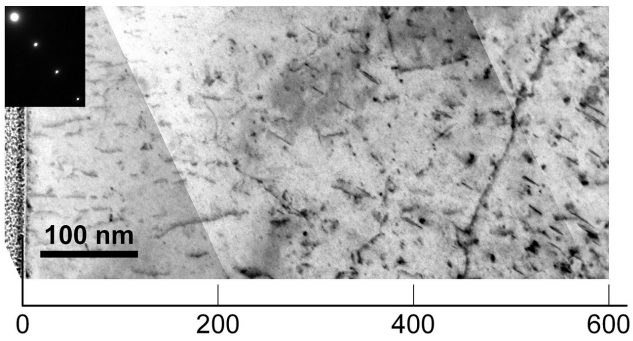

Figure 4.6: TEM kinematic BF image showing the dislocation loops in A709 irradiated to 10 peak dpa at 400℃.

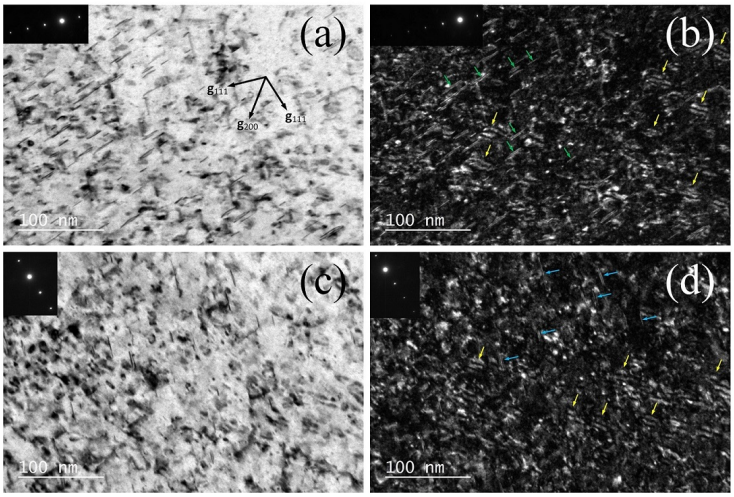

Figure 4.7: TEM kinematic BF and WBDF images showing the Frank loops in A709 irradiated to 10 peak dpa at 400℃: (a) and (b) are BF and WBDF images taken with $\mathbf{g}_{1\bar{1}1}$ strongly excited, (c) and (d) are BF and WBDF images of another region taken with $\mathbf{g}_{11\bar{1}}$ strongly excited. The zone axis is [011].

The average Frank loop size in the 200–400 nm region is 14.99±6.03 nm. The measured $(11\bar{1})$ Frank loop density is 4.03×10^{21} m^{-3}. The total projected Frank loop density is 4 times the density of $(11\bar{1})$ Frank loops, 1.61×10^{22} m^{-3}.

The dislocation loops can also be observed in APT specimens if there is detectable elemental segregation at loop periphery. As an example, Fig. 4.8 shows the APT results of reconstructed atom maps and 30% Ni isosurfaces of A709 irraidated to 10 peak dpa at 400℃. Note that the top of the tip is ∼200 nm beneath the sample surface. The dislocation loops are readily visible in the Si map and become quite obvious in the 30% Ni isosurface image.

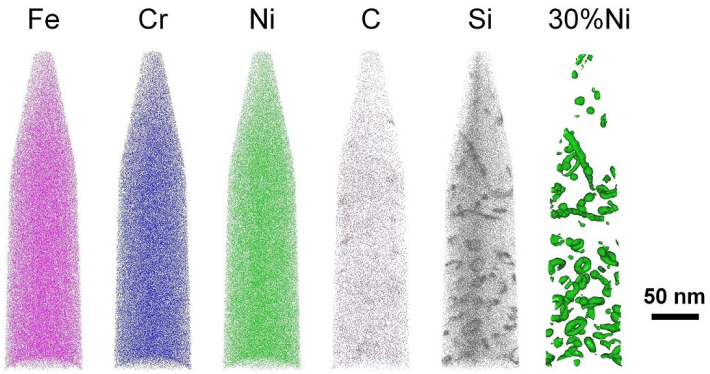

Figure 4.8: APT results showing dislocation loops in A709 irradiated to 10 peak dpa at 400℃.

Fig. 4.10 shows the rel-rod DF image of the Frank loops in A709 irradiated to 50 peak dpa at 400℃. The Frank loop size and density seem to be similar to the 10 peak dpa case. Further quantitative measurement shows that the average Frank loop size in the 200–400 nm region is 13.44±3.32 nm, slightly smaller than that of 10 peak dpa. The measured Frank loop density (one variant) is 2.68×10^{21} m^{-3}, smaller than the 10 peak dpa case. The total projected Frank loop density is 1.07×10^{22} m^{-3}.

For 400℃ irradiation, neither loop size nor loop density increased from 4.24 dpa (10 peak dpa) to 12.72 dpa (50 peak dpa). The Frank loop density even dropped at the higher dose.

4.1.3 *Ex situ* bulk irradiation at 500℃

For A709 irradiated to 10 peak dpa at 500℃, Fig. 4.11 is an overview showing the depth-dependent loop distribution. It can be seen that dislocation loops distributed all the way along the irradiation direction up to ∼1300 nm, which is consistent with SRIM calculated dose profile. The loop density is much lower at near-surface region and is the highest at about ∼1000 nm depth region, also consistent with SRIM calculated dose profile.

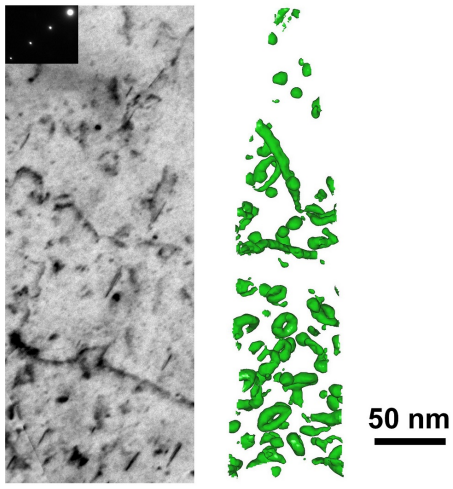

Figure 4.9: TEM and APT image of dislocation loops in A709 irradiated to 10 peak dpa at 400℃.

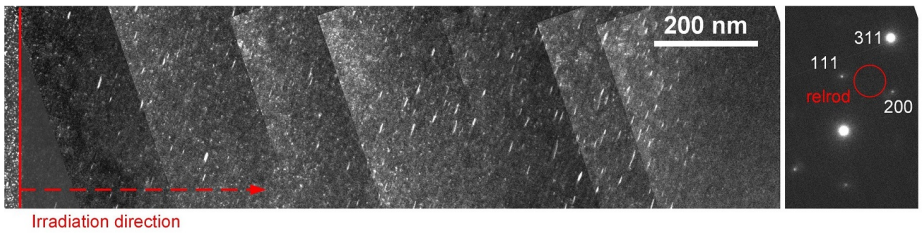

Figure 4.10: TEM rel-rod DF image showing the Frank loops in A709 irradiated to 50 peak dpa at 400℃. The zone axis is $[01\bar{1}]$.

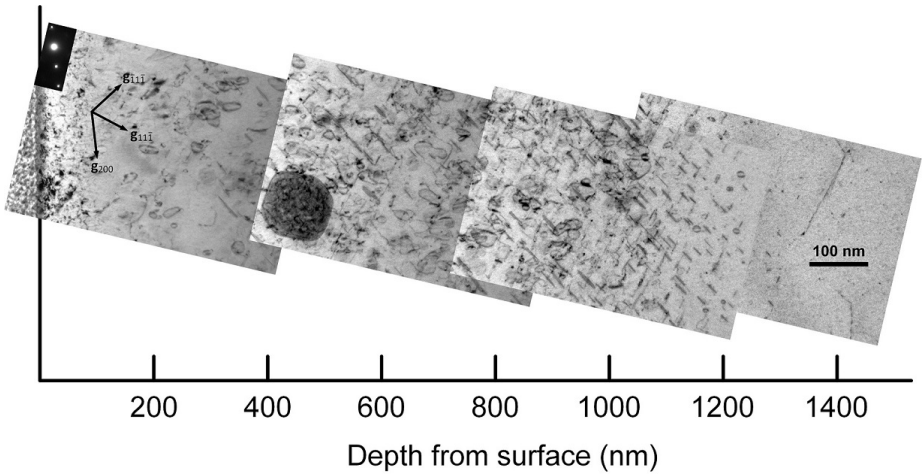

Figure 4.11: TEM kinematic BF images of dislocation loops in A709 irradiated to 10 peak dpa at 500℃.

Fig. 4.12 shows higher magnification TEM images of the dislocation loops. Using the same projection method, it is easy to tell that in Fig. 4.12 (a), the near edge-on loops perpendicular to $\mathbf{g}_{11\bar{1}}$ are $(11\bar{1})$ loops and the near edge-on loops perpendicular to $\mathbf{g}_{\bar{1}1\bar{1}}$ are $(\bar{1}1\bar{1})$ loops, and the elliptical loops perpendicular to $\mathbf{g}_{200}$ are $(\bar{1}11)$ or (111) loops. Fig. 4.12 (b) clearly shows the stacking fault contrast of these loops, confirming that they are faulted loops.

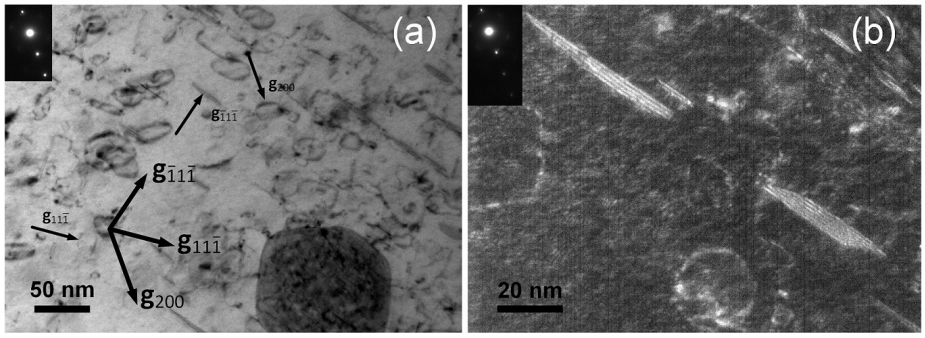

Figure 4.12: TEM images showing the characteristics of loops in A709 irradiated to 10 peak dpa at 500℃: (a) kinematic BF image of 200–500 nm depth region showing the orientation of the loops, and (b) high mag image showing the faulted nature of the loops.

The rel-rod DF images of the Frank loops in A709 irradiated at 500℃ to 10, 50, and 150 peak dpa are shown in Figs. 4.13 (a), (b), and (c), respectively. The loop size for all three cases looks similar. Overall, the Frank loop density seems

lowest for 50 peak dpa and the highest for 150 peak dpa. Quantitative results on the Frank loop size and density are shown in Figs. 4.14 and 4.15, respectively. Fig. 4.14 shows that the Frank loop size distribution is almost identical for all three cases. The loop size is almost constant for depth less than 1 µm. Near the tail (1–1.4 µm in depth) region, both large loops and small loops are found. At regions over 400 nm in depth, the loop density dropped noticeably from 10 peak dpa to 50 peak dpa, and then increased again at 150 peak dpa.

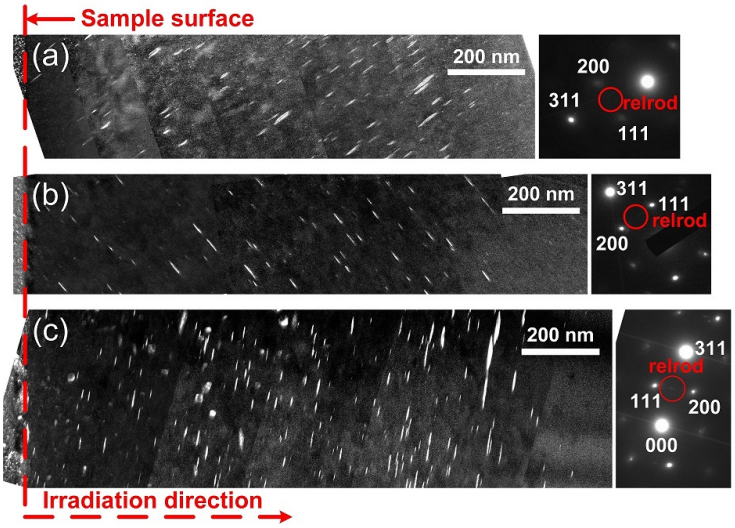

Figure 4.13: Rel-rod dark-field images showing the Frank loops in A709 irradiated to (a) 10, (b) 50, and (c) 150 peak dpa at 500°C.

4.1.4 *Ex situ* bulk irradiation at 600°C

The Frank loops in A709 irradiated at 600°C to 10 and 50 peak dpa are shown in Figs. 4.16 and 4.17, respectively. The loop size is significantly larger than 400 and 500°C irradiations. Loops over 50 nm are found in both 10 and 50 peak dpa specimens. Compared to 400 and 500°C irradiations, the loop density dropped significantly. Only several loops were found in the 200–400 nm depth region.

4.1.5 Summary of Frank loops in ion-irradiated A709

Table 4.2 lists the quantitative results on the Frank loops in A709 *ex situ* irradiated at 400, 500, and 600°C to 10 and 50 peak dpa. All the data are from the 200–400 nm depth region.

Efforts were also made to quantitatively compare the dose dependence and temperature dependence of the Frank loops in ion-irradiated A709 with existing austenitic stainless steel (mostly 316) neutron irradiation data. Fig. 4.18 shows

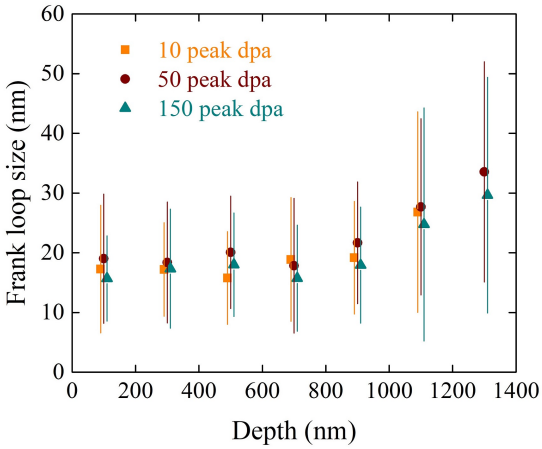

Figure 4.14: Frank loop size in A709 irradiated to 10, 50, and 150 peak dpa at 500℃. The error bars represent the standard deviations.

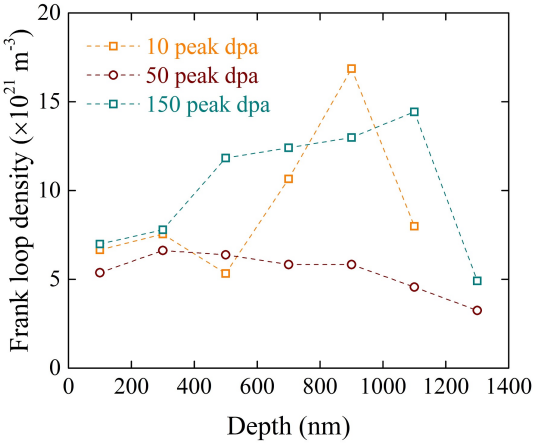

Figure 4.15: Frank loop density in A709 irradiated to 10, 50, and 150 peak dpa at 500℃.

Table 4.2: Quantitative results of the Frank loops in A709 *ex situ* irradiated at 400–600℃.

Irr. condition	Loop size (nm)	Loop density (one variant) ($\times 10^{21}$ m^{-3})	Projected density ($\times 10^{21}$ m^{-3})	local dpa
10 peak dpa, 400℃	14.99 ± 6.03	4.03	16.11	4.24
50 peak dpa, 400℃	13.44 ± 3.32	2.68	10.71	12.72
10 peak dpa, 500℃	17.21 ± 7.83	1.87	7.54	4.24
50 peak dpa, 500℃	18.39 ± 10.12	1.66	6.62	12.72
10 peak dpa, 600℃	26.34 ± 25.10	0.70	2.79	4.24
50 peak dpa, 600℃	41.02 ± 10.97	0.26	1.04	12.72

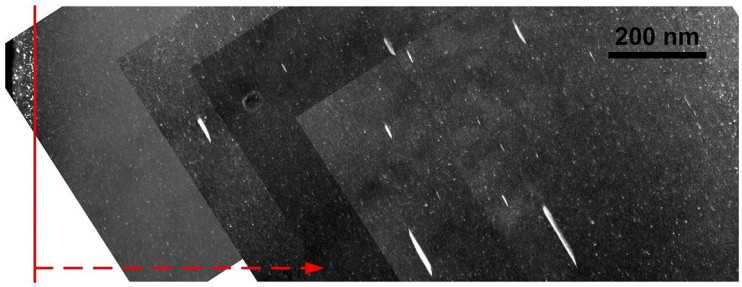

Figure 4.16: TEM rel-rod DF image showing the Frank loops in A709 irradiated to 10 peak dpa at 600℃.

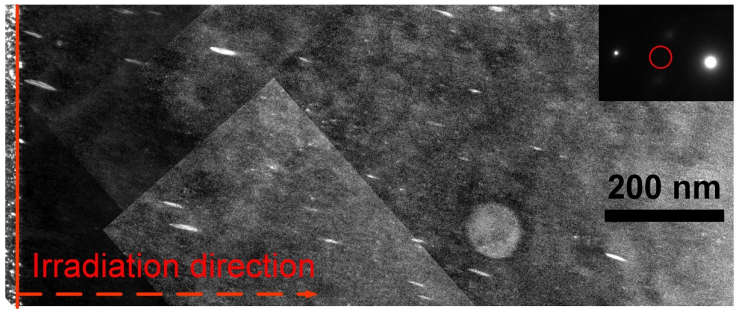

Figure 4.17: TEM rel-rod DF image showing the Frank loops in A709 irradiated to 50 peak dpa at 600℃.

the dose dependence of Frank loop density in A709 irradiated at 400℃ together with existing austenitic stainless steel neutron irradiation data. It is easy to see that at 400℃, the density of ion-irradiated A709 shows similar saturation trend as other austenitic stainless steels and the absolute density values are also in line with existing stainless steel neutron irradiation data.

Fig. 4.19 shows the temperature dependence of the Frank loop density in A709 together with existing austenitic stainless steel 316 neutron irradiation data. As can be seen, the Frank loop density of A709 at 400℃ is close to the density of austenitic stainless steel 316 neutron-irradiated at 400℃. The Frank loop density of A709 ion-irradiated at 500℃ is similar to the density of austenitic stainless steel 316 neutron-irradiated at 425℃. The Frank loop density of A709 ion-irradiated at 600℃ is similar to the density of austenitic stainless steel 316 neutron-irradiated at 475℃.

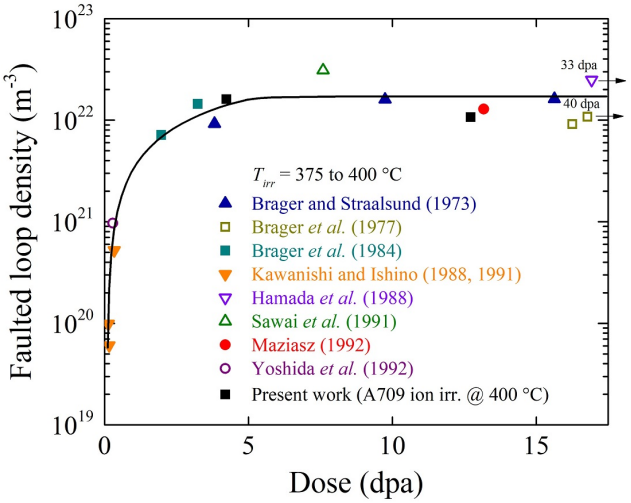

Figure 4.18: Dose dependence of Frank loop density in A709 irradiated at 400℃, compared with existing austenitic stainless steel neutron data.

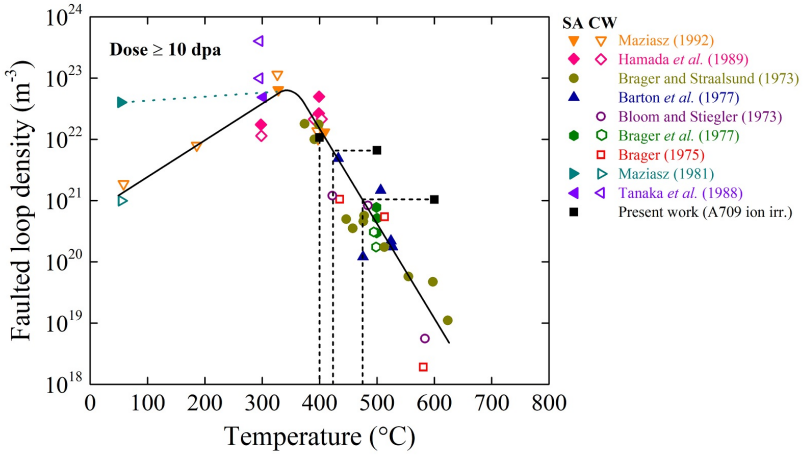

Figure 4.19: Temperature dependence of Frank loop density in A709 ion-irradiated to 50 peak dpa, compared with existing neutron data of austenitic stainless steel 316. The density of A709 is extracted from 200–400 nm depth region with corresponding local dose of 12.72 dpa.

4.2 Radiation-induced segregation and precipitation

Radiation-induced segregation (RIS) is a major issue for austenitic stainless steels irradiated at elevated temperatures. RIS is caused by the perferential coupling between the fluxes of alloying elements and the defect fluxes [1]. As a result, the alloying elements can undergo enrichment or depletion at defect sinks. In irradiated austenitic stainless steels, Cr is always found depleted at grain boundaries, which could contribute to intergranular corrosion and stress corrosion cracking [1].

For A709, it was found that the RIS of Ni and Si happened under all investigated irradiation conditions, i.e. temperature from 300 to 600℃, and dose from 10 peak dpa to 150 peak dpa.

Fig. 4.20 is the APT result showing the segregation of Ni at network dislocations in A709 irradiated to 10 peak dpa at 300℃. The dislocation network structure is similar to TEM observations in Fig. 4.5. The enrichment of Si at network dislocations was also observed (not shown here).

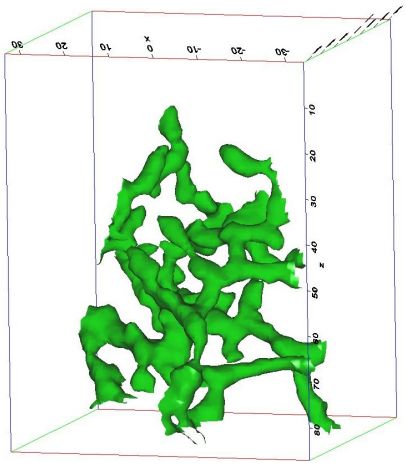

Figure 4.20: APT 26% Ni isosurfaces showing Ni segregation at network dislocations in A709 irradiated to 10 peak dpa at 300℃. The top corresponds to ∼200 nm depth and the irradiation direction is from top to bottom.

The segregation of Ni and Si at dislocation segements and dislocation loops in A709 irradiated to 10 peak dpa at 400℃ was shown in Fig. 4.8. It should be noted that at 10 peak dpa, in addition to RIS of Ni and Si, some precipitate-like Ni,Si-rich clusters were found. The proxigram in Fig. 4.21 shows that near the edge of the chosen dislocation loop, Ni enriched from a base composition level of 21.7 at.% to ∼53 at.%, and Si enriched from a base composition level of 0.3 at.% to around 11 at.%, whereas Fe depleted from a base composition level of 53.5

at.% to ∼26.5 at.% and Cr depleted from a base composition level of 21.5 at.% to ∼8.5 at.%. For the Ni,Si-rich precipitates, Fig. 4.22 shows the proxigram of chosen precipitates. It was found that the Ni and Si concentrations of these Ni,Si-rich precipitates is only slightly higher than the Ni and Si concentrations of the dislocation loop edge.

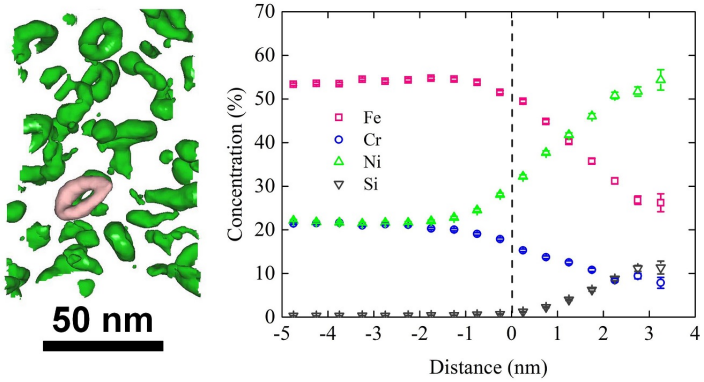

Figure 4.21: Proxigram showing the enrichment of Ni and Si and depletion of Fe and Cr at a dislocation loop in A709 irradiated to 10 peak dpa at 400℃.

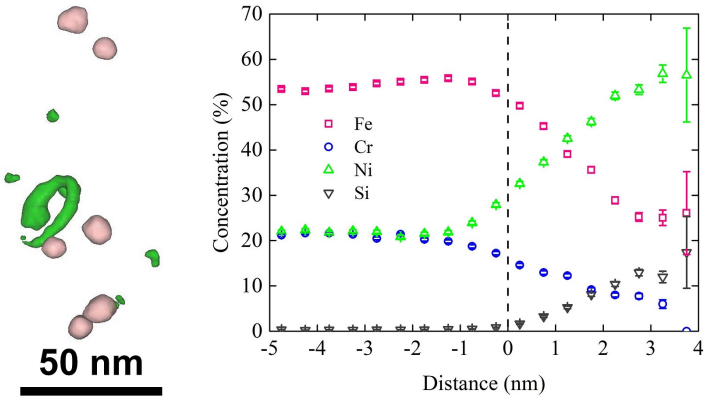

Figure 4.22: Proxigram of selected Ni,Si-rich clusters in A709 irradiated to 10 peak dpa at 400℃.

Figs. 4.23–4.25 show the APT results of A709 irradiated at 500℃ to 10, and 50 peak dpa, respectively. Again, RIS of Ni and Si was observed at all three doses. At 10 peak dpa, as shown in the proxigrams of dislocation loops in Fig. 4.24 (a), Ni and Si enriched to 60 at.% and 13 at.%, whereas Fe and Cr depleted to 21 at.% and 6 at.%, respectively. For the Ni,Si-rich clusters shown in Fig. 4.24 (b), Ni and Si enriched to 70 at.% and 23 at.%, and Fe and Cr depleted to

5.1 at.% and 0.6 at.%, respectively.

It is reasonable to believe that the Ni,Si-rich clusters are radiation-induced precipitates, for two reasons: (1) the proxigram of the Ni,Si-rich precipitates is very similar to that of the dislocation loops, and the Ni and Si segregation at defect sinks such as dislocation loops is radiation-induced. The same mechanism can lead to the precipitation of Ni,Si-rich phase when local concentration exceeds the solubility, and (2) the composition of these Ni,Si-rich clusters is very close to the radiation-induced Ni_3Si (γ') precipitates found in neutron-irradiated austenitic stainless steel 316.

Although it is believed that the Ni,Si-rich clusters are radiation-induced, they are different from the radiation-induced Ni_3Si precipitates found in neutron-irradiated austenitic stainless steel 316, as no extra spots showed up in the diffraction pattern. The reason should be that in our high dose-rate (1.7×10^{-3} dpa/s) ion irradiation, the displacement cascades frequently knock the atoms of the γ' precipitates out and the crystal structure is distorted. Similar phemonema happened to the α' precipitates in ion-irradiated BCC Fe–Cr alloys. The Cr concentation of the α' precipitates is below equilibrium in lower dose-rate ion irradiated Fe–18Cr [42] and no α' precipitates could be found in high dose-rate ($\geqslant 10^{-3}$ dpa/s) ion-irradiated Fe–Cr alloys.

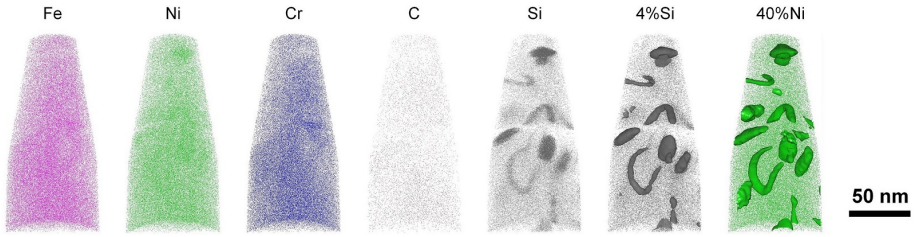

Figure 4.23: APT results showing Ni,Si-rich clusters and RIS of Ni and Si at dislocation loops in A709 irradiated to 10 peak dpa at 500℃.

The RIS of Ni and Si not only happened at dislocation loops and network dislocations, but also at the interfaces of voids. Figs. 4.26 and 4.27 show the EDS mapping of A709 irradiated to 150 peak dpa at 500℃ and 600℃, respectively. The interfaces of voids are clearly enriched in Ni (the count of Si is too low for EDS mapping).

Similar Ni and Si segragation and Ni,Si-rich precipitates have also been observed in irradiated 316H. Fig. 4.28 is the STEM-EDS mapping result of 316H irradiated to 150 peak dpa at 500℃. Several big Ni,Si-rich precipitates were found. Ni (and possibly Si) segregation also happened near voids and Cr-rich carbide particle-matrix interfaces.

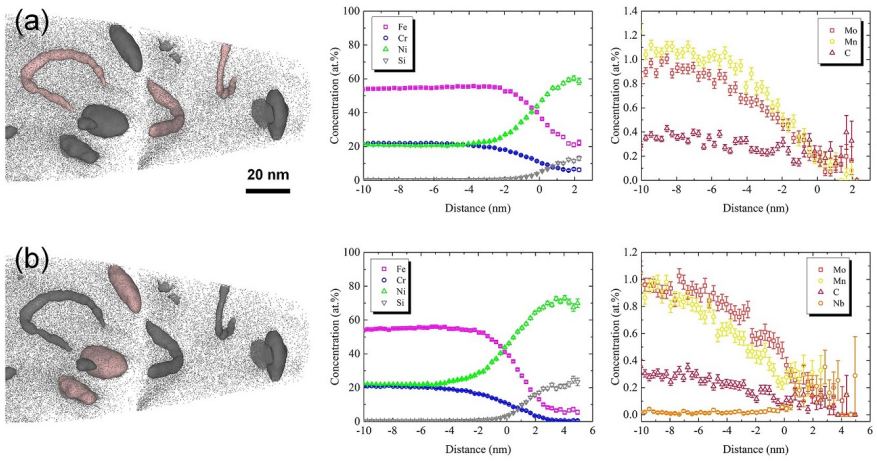

Figure 4.24: Proxigrams of (a) dislocation loops, and (b) Ni,Si-rich clusters in A709 irradiated to 10 peak dpa at 500℃.

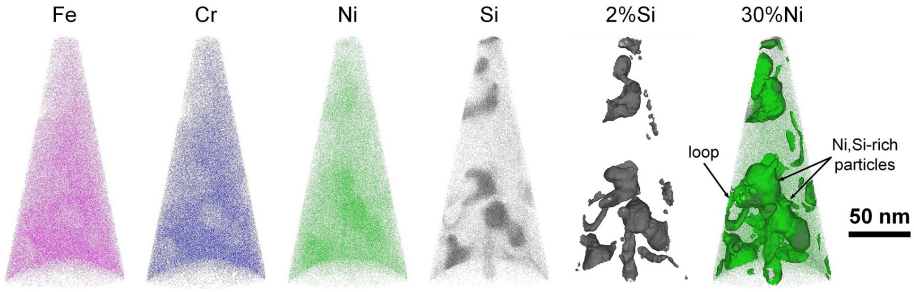

Figure 4.25: APT results showing large Ni,Si-rich particles and RIS of Ni and Si at dislocation loops in A709 irradiated to 50 peak dpa at 500℃.

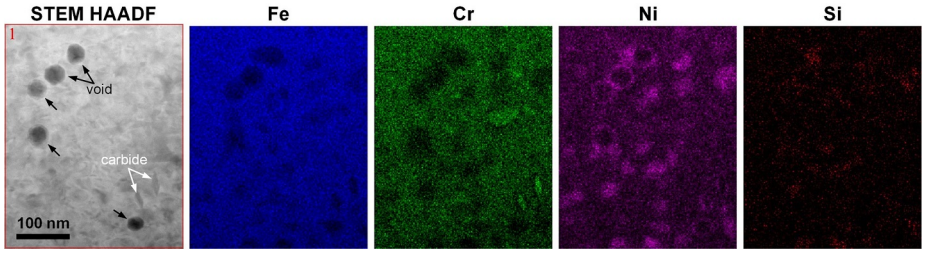

Figure 4.26: STEM-EDS mapping showing Ni,Si-rich precipitates and segregation of Ni and Si at void surfaces, Cr-rich carbide particle-matrix interfaces in A709 irradiated to 150 peak dpa at 500℃.

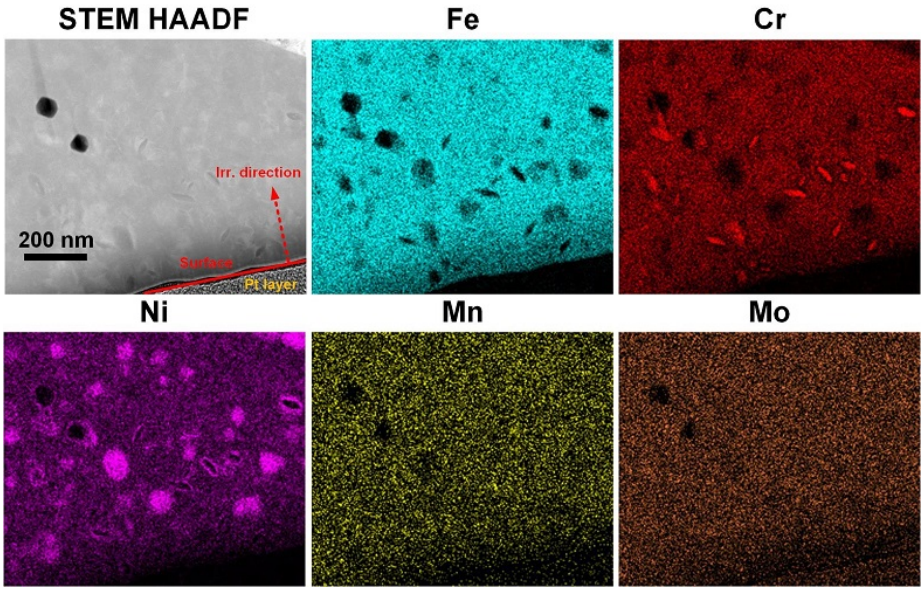

Figure 4.27: STEM-EDS mapping showing Ni,Si-rich precipitates, Cr-rich carbides, and segregation of Ni and Si in A709 irradiated to 150 peak dpa at 600℃.

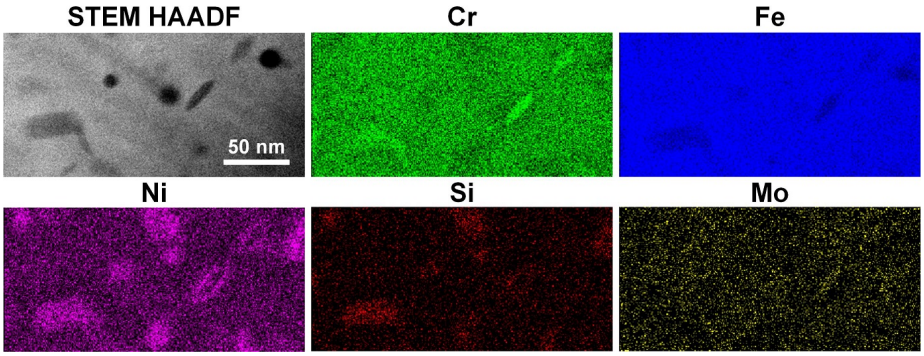

Figure 4.28: STEM-EDS mapping showing Ni,Si-rich precipitates and segregation of Ni at Cr-rich carbide particle-matrix interfaces in 316H irradiated to 150 peak dpa at 500℃.

4.3 Radiation-modified precipitation

Besides radiation-induced Ni,Si-rich clusters, Cr-rich carbides were frequently found in highest dose (150 peak dpa) specimens. The Cr-rich carbides are readily visible in the EDS mapping results in Figs. 4.26 and 4.27. Ni is also found enriched at the carbide-matrix interfaces.

The Cr-rich carbides can be studied in more detail using APT. Fig. 4.29 shows the APT result of A709 irradiated at 500℃ to 150 peak dpa. Three Cr-rich carbides can be easily seen. It is also found that the carbides have a core-shell structure: carbide core with Ni,Si shell. The Ni,Si shell can be easily understood by radiation-induced segregation at defect sinks, and in this case the sinks are the carbide-matrix interfaces.

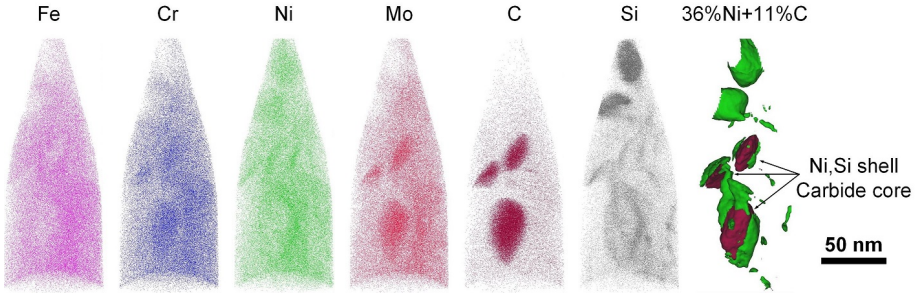

Figure 4.29: APT results showing Ni,Si shell with carbide core structure in A709 irradiated to 150 peak dpa at 500℃.

Proxigrams were used to quantitatively characterize the Cr-rich carbide precipitates and the enrichment of Ni and Si at the carbide interfaces. Fig. 4.30 shows the proxigrams of a carbide in A709 irradiated at 500℃ to 150 peak dpa. It can be seen that the peak Ni and Si concentrations at the carbide interface are around 37 at.%, and 2.2 at.%, respectively. The carbide is enriched in Cr and Mo. The composition of the carbide (defined at the FWHM) is about 52.4 at.% Cr, 2.7 at.% Mo, 13.0 at.% Fe, 9.6 at.% Ni, and 20.6 at.% C. The metal to carbon ratio (M/C) is about 3.76, very close to that of $M_{23}C_6$ (3.83). The enrichment of Cr and Mo in these carbides is also consistent with the fact that $M_{23}C_6$ carbides are likely to be enriched in Cr and Mo.

However, it should be noted that these Cr-rich carbides (presumably $M_{23}C_6$) formed at 500℃ differ from the $M_{23}C_6$ carbides occurred during thermal aging in several aspects: (1) the morphology of the carbides found in A709 irradiated at 500℃ is different from the $M_{23}C_6$ carbides found in thermally-aged Fe–20Cr–25Ni–Nb stainless steels, the former are thin plate-like, whereas the latter are typically cuboidal, (2) the $M_{23}C_6$ carbides in irradiated A709 are intragranular precipitates, whereas $M_{23}C_6$ carbides found in thermally-aged Fe–20Cr–25Ni–Nb stainless steels are located at grain boundaries as suggested in Fig. 2.17, and (3) the carbides in irradiated A709 formed after irradiation for about 24 h, whereas the $M_{23}C_6$ carbides are only expected after thermal aging for

5000–10,000 h at 500℃. Based on above information, these carbides should be identified as radiation-modified precipitates.

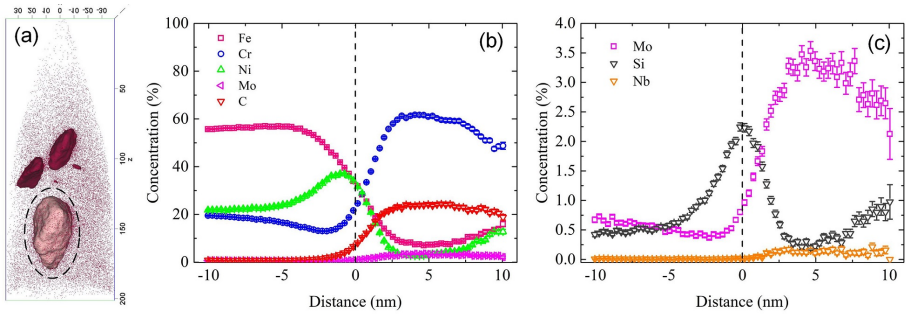

Figure 4.30: APT results of A709 irradiated to 150 peak dpa at 500℃ showing: (a) three carbides, (b) and (c) are the proxigrams of the chosen carbide showing the Ni and Si segregation at carbide interface and also the elemental concentrations inside the carbide.

At 600℃, Cr-rich carbides of similar thin plate shape were also found in the 150 peak dpa specimen, as shown in Fig.4.27. The carbide number density is higher at 600℃. APT was also used to check the composition of the carbides. Fig. 4.31 shows the APT results of a Cr-rich carbide in A709 irradiated at 600℃ to 150 peak dpa. From the reconstructed atom maps, it is easy to see that the carbide is enriched in Cr, Mo, Nb, and depleted in Fe, Mn. Ni and Si enrichment at the carbide interface was again observed.

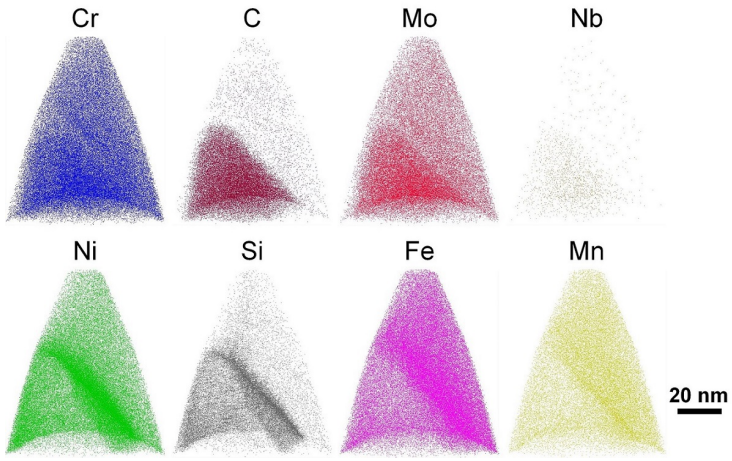

Figure 4.31: Reconstructed atom maps showing a carbide in A709 irradiated to 150 peak dpa at 600℃.

The composition of the caribde can be obtained from the proxigrams shown

in Fig. 4.32. The proxigrams were generated based a 35% Ni isosurface. From Fig. 4.32, the composition of major elements of the carbide is roughly 71.3% Cr, 6.1% Mo, 3.7% Fe, 2.6% Ni, 14.4 % C. The carbide also contains ∼0.3% Nb and ∼0.6% N. The metal to carbon ratio (M/C) is about 5.81, very close to 6. Therefore, this carbide is likely to be M_6C type, different from the 500℃ case.

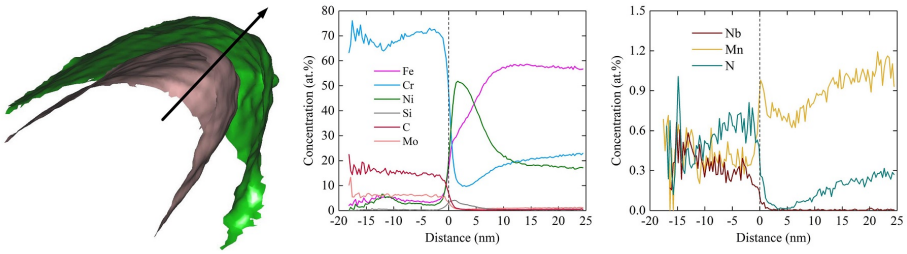

Figure 4.32: Proxigrams showing the Ni and Si segregation and the composition of a carbide in A709 irradiated to 150 peak dpa at 600℃.

In addition, small Ni,Fe-rich clusters were found inside the carbide shown in Fig. 4.31. Fig. 4.33 shows the four Ni,Fe-rich clusters and the corresponding proxigram. These four clusters are enriched in only Ni and Fe, and the measured Ni and Fe concentrations are 41.3 at.% and 24.5 at.%, respectively. It is unclear how these Ni,Fe-rich clusters formed inside the Cr-rich carbide. It should be noted that similar Ni,Fe-rich clusters were also observed in the Cr-rich carbide at 500℃ (Fig. 4.30) but not shown.

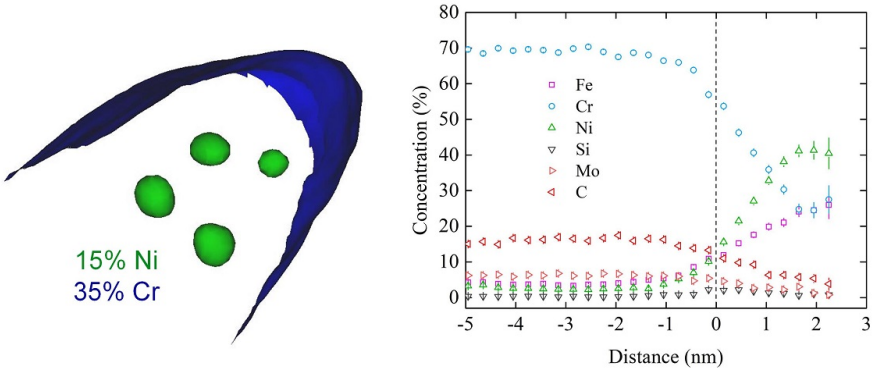

Figure 4.33: Proxigrams showing the composition of four Ni,Fe-rich clusters inside the carbide in Fig. 4.31.

In order to verify that the carbides observed at 600℃ are M_6C carbides, TEM diffraction patterns were employed. As shown in the diffraction pattern in Fig. 4.34, The carbide has an $[011]_m \| [011]_p$, $(11\bar{1})_m \| (\bar{3}3\bar{3})_p$ orientation relationship with respect to the matrix. The corresponding lattice constant is about 3 times

that of the matrix, or ∼1.08 nm, also consistent with the M_6C phase.

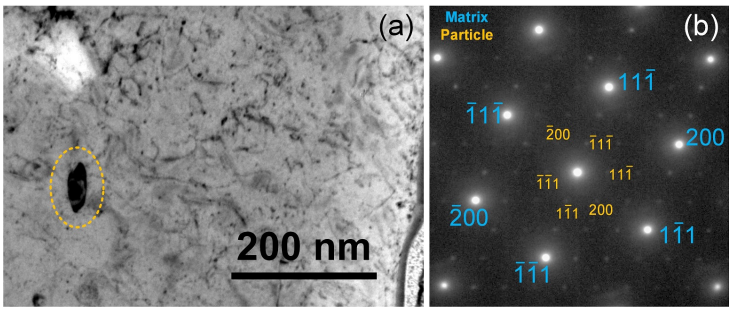

Figure 4.34: Diffraction pattern of a Cr-rich carbide in A709 irradiated to 150 peak dpa at 600℃.

In addition to the M_6C carbides, another type of Cr-rich carbide was also observed in A709 irradiated to 150 peak dpa at 600℃. Fig. 4.35 shows the HRSTEM results of a carbide. It was found that the carbide is of hcp crystal structure and has an $[1\bar{1}0]_m \| [1\bar{2}10]_p$, $(111)_m \| (0002)_p$ orientation relationship with respect to the matrix. The measured d-spacing of (0002) planes is ∼2.220 Å, and the d-spacing of $(10\bar{1}0)$ planes is ∼2.425 Å. The corresponding lattice constants are $a \approx 2.80$Å and $c \approx 4.44$Å, and the c/a ratio is about 1.59. EDS result (not shown here) of this carbide shows it is enriched in Cr and slightly enriched in Mo. Combining all the information, the precipitate is idenfied as $(\mathbf{Cr},\mathrm{Mo})_2(\mathbf{C},\mathrm{N})$, the space group of which is P63/mmc (194). To the author's best knowledge, this phase has not been reported in thermally-aged NF709 or Fe–20Cr–25Ni austenitic stainless steels.

4.4 Radiation-induced changes in precipitate orientation relationship

The MX precipitates in the unirradiated A709 are incoherent precipitates. Fig. 4.36 (a) shows a ∼70 nm MX precipitate and Fig. 4.36 (b) is the diffraction pattern taken on the [001] zone of the matrix. Besides the diffraction spots of the matrix, only two 020 diffraction spots from the MX precipitate were identified. The remaining extra spots were due to double diffraction. On [001] zone, the projected angle between $\mathbf{g}_{020,m}$ and $\mathbf{g}_{020,p}$ is roughly 7.5° (subscripts m and p represent matrix and precipitate, respectively). This rotation angle indicates that the 020 lattice planes of the precipitate is rotated with respect to the 020 lattice planes of the matrix.

It was also found that the unirradiated incoherent MX precipitates have different orientations with respect to the matrix. Figs. 4.36 (c)–(e) are diffraction patterns of different MX precipitates. Fig. 4.36 (c) is another diffraction pattern taken on the [001] zone, and the projected angle between $\mathbf{g}_{020,m}$ and $\mathbf{g}_{020,p}$

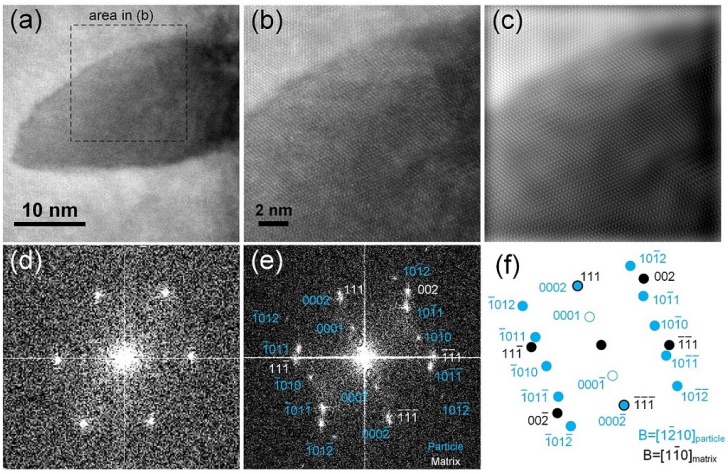

Figure 4.35: HRSTEM results of a carbide in A709 irradiated to 150 peak dpa at 600℃: (a) and (b) HRSTEM images, (c) FFT-IFFT enhanced image showing the lattice fringes, (d) FFT of the matrix, (e) FFT of the region in (b), and (f) indexed lattice planes showing the orientation relationship.

is roughly 11.1°. Fig. 4.36 (d) and (e) are diffraction patterns of two different MX precipitates taken both on the [011] zone of the matrix. Again, different orientations with respect to the matrix was observed. In all cases, only one pair of diffraction spots (e.g. 020 and 0$\bar{2}$0) from the MX precipitate was observed and they are always rotated relative to the matrix diffraction spots.

However, the orientation relationship was found changed after irradiation at 600℃ to 50 peak dpa. Fig. 4.37 shows the diffraction patterns of a MX precipitate in A709 irradiated at 600℃ to 50 peak dpa. The size of this precipitate is similar to unirradiated MX and the EDS result in Fig. 4.37 shows that this precipitate is still Nb-enriched. The diffraction patterns shown in Figs. 4.37 (c)–(e) in three zones [$\bar{1}$12], [001], and [$\bar{1}$14] all confirm that this precipitate has a cubic-on-cubic orientation relationship with respect to the matrix. The lattice constant of this precipitate is measured to be ∼4.42 Å, consistent with that of MX phase.

The radiation-induced changes in MX precipitate orientation relationship is believed to be due to both collisional events and radiation-enhanced diffusion.

Besides the change in orientation relationship, RIS of Ni (and also possibly Si) was observed at the MX particle-matrix interface. As shown in Fig. 4.38 (a), the MX precipitate before irradiation is enriched in Nb and no segergation was observed at the MX particle-matrix interface. However, as shown in Fig. 4.38 (b), EDS mapping on a MX precipitate in A709 irradiated to 50 peak dpa at 600℃ shows significant segregation of Ni at the MX particle-matrix interface.

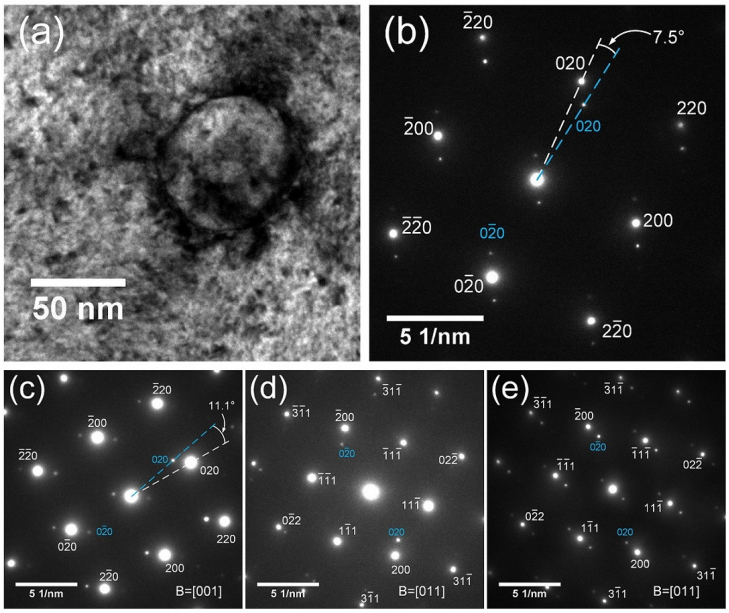

Figure 4.36: Unirradiated incoherent MX precipitates in Alloy 709: (a) TEM bright-field (BF) image showing the MX precipitate, and (b) the diffraction pattern of the precipitate taken on [001] zone. (c)–(e) are diffraction patterns of different MX precipitates showing distinct relative orientations with respect to the matrix.

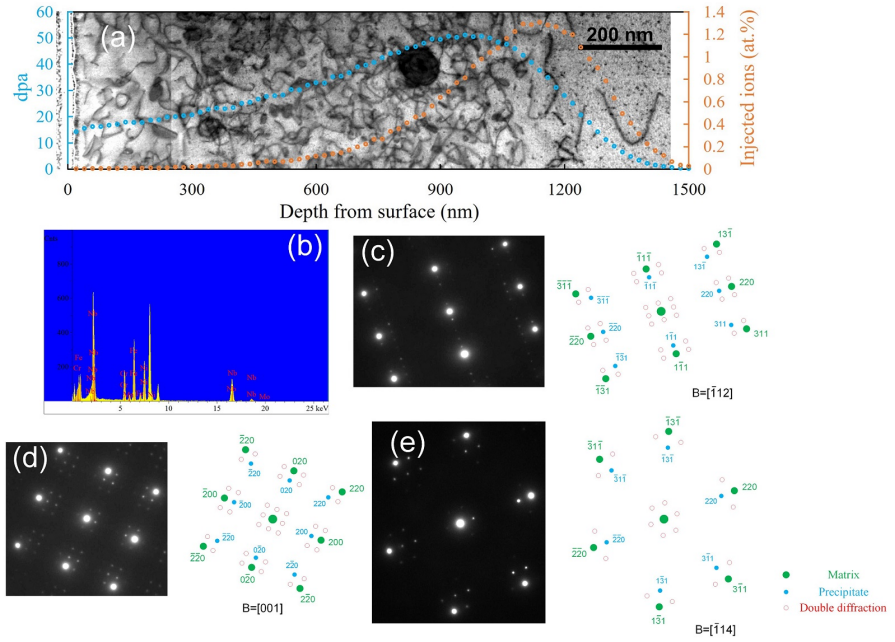

Figure 4.37: A MX precipitate in A709 irradiated to 50 peak dpa at 600°C: (a) STEM bright-field image showing the dislocation microstructure and a MX precipitate at around 850 nm depth. The blue curve and orange curve represent dose in displacement per atom (dpa) and injected ion fraction (at.%), respectively. (b) EDS result showing that the MX precipitate is still enriched in Nb, (c)–(e) are diffraction patterns of the precipitate taken on [$\bar{1}$12], [001], and [$\bar{1}$14] zones, respectively. The large solid green circles, small solid blue circles, and small open red circles represent the diffraction spots from the matrix, the precipitate, and double diffraction, respectively.

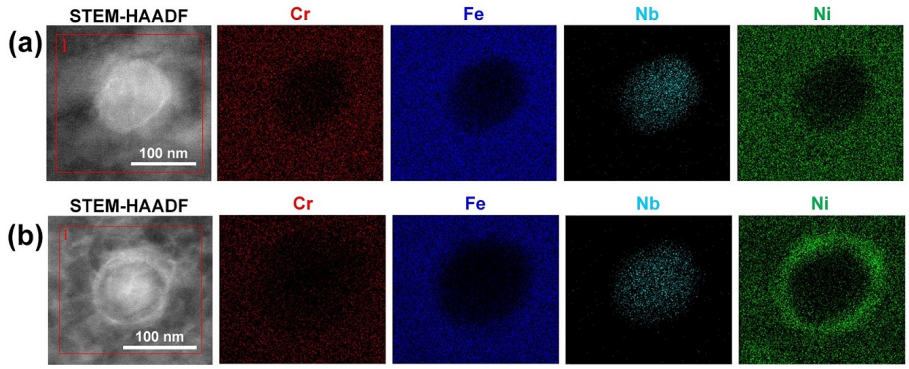

Figure 4.38: STEM-EDS mapping showing RIS of Ni at the MX particle-matrix interface in A709 irradiated to 50 peak dpa at 600℃: (a) a MX precipitate before irradiation, and (b) another MX precipitate after irradiation.

4.5 Radiation-induced voids

For A709 irradiated to 10 peak dpa, no voids were found at 300–500℃, and only 1 void (∼25 nm) was found in the 600℃ specimen. At 50 peak dpa, voids were only found in the 500℃ specimen and the 600℃ specimen, and the number density at 600℃is extremely low (only 1 void in the entire specimen). Fig. 4.39 shows the microstructure of the same depth region (200–600 nm) in A709 irradiated to 50 peak dpa at 400, 500, and 600℃, respectively. Voids were only found in Fig. 4.39 (b).

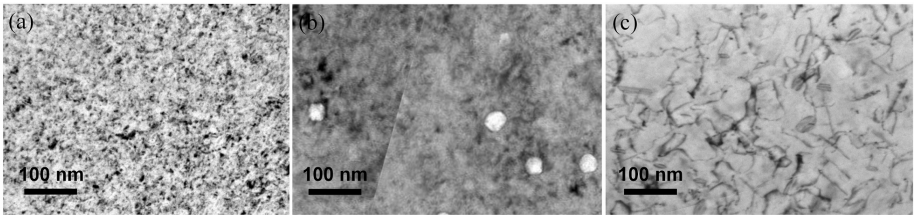

Figure 4.39: TEM BF images showing the microstructure of A709 irradiated to 50 peak dpa at (a) 400℃, (b) 500℃, and (c) 600℃. All the images are from the 200–600 nm depth region and the average dose is 4.94 dpa. The irradiation direction is from top to bottom. The top edge is at 200 nm depth and the bottom edge is at 600 nm depth.

A709 was irradiated to 150 peak dpa only at two temperatures: 500℃ and 600℃. At 150 peak dpa, voids in the 600℃ are relatively large (50–120 nm), but the number density is very low ($< 2 \times 10^{19}$ m^{-3}). Only quantitative analysis for A709 irradiated to 50 peak dpa and 150 peak dpa at 500℃ was carried out.

To quantify the depth-dependent distribution of voids, the STEM HAADF

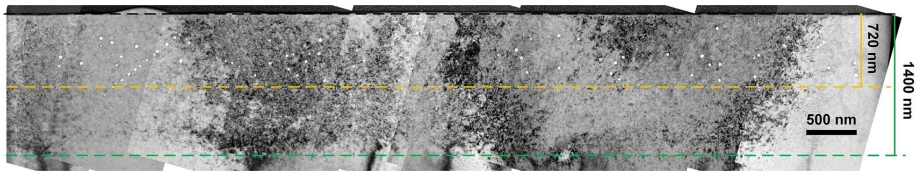

Figure 4.40: TEM BF images showing the radiation-induced voids in A709 irradiated to 50 peak dpa at 500℃.

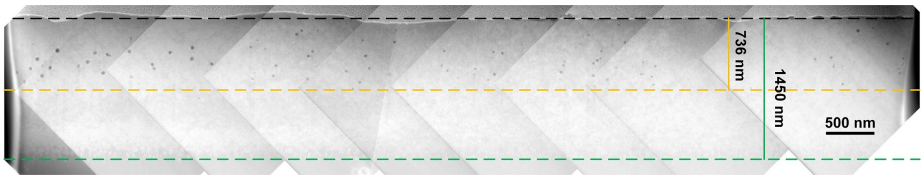

Figure 4.41: STEM HAADF images showing the radiation-induced voids in A709 irradiated to 150 peak dpa at 500℃.

(or TEM) images were divided into regions with depth intervals of 200 nm. The void swelling is estimated using:

$$\Delta V/V_0(\%) = \frac{V_{void}}{V - V_{void}} \times 100 \tag{4.1}$$

where V is the volume of the region of interest (ROI), V_{void} is the volume of voids inside the ROI.

The number density and size of voids, and swelling of A709 irradiated at 500℃ to 50 and 150 peak dpa are listed in Tables 4.3 and 4.4, respectively. The error bars of the void size represent the standard deviations, and the error bars of swelling are calculated based on the Student's t-distribution with 90% (double sided) confidence level.

Table 4.3: Void number density, size, and swelling of A709 irradiated to 50 peak dpa at 500℃.

Depth (nm)	N_{void} ($\times 10^{20}$ /m^3)	d_{void} (nm)	swelling (%)	local dpa
0–200	0.29	28.9 ± 4.8	0.039 ± 0.020	16.5
200–400	1.61	30.6 ± 5.4	0.263 ± 0.039	21.2
400–600	2.67	30.5 ± 6.0	0.441 ± 0.052	28.2
600–800	0.78	27.8 ± 7.4	0.103 ± 0.031	38.8

The void swelling data from Tables 4.3 and 4.4 are also plotted in Fig. 4.42, together with the dose profile and injected ion profile in arbitrary unit (a.u.). It can be clearly seen that the swelling of 50 peak dpa specimen is about the same as that of the 150 peak dpa specimen, indicating that the swelling is still inside the incubation period. This can also be confirmed by the fact that the number density and size of the voids in the 150 peak dpa specimen is roughly the

Table 4.4: Void number density, size, and swelling of A709 irradiated to 150 peak dpa at 500℃.

Depth (nm)	N_{void} ($\times 10^{20}$ /m^3)	d_{void} (nm)	swelling (%)	local dpa
0–200	0.57	20.1 ± 8.1	0.035 ± 0.020	49.5
200–400	1.01	30.8 ± 5.8	0.171 ± 0.35	63.6
400–600	1.89	32.4 ± 6.0	0.372 ± 0.053	84.5
600–800	0.64	30.5 ± 4.5	0.102 ± 0.021	116.5

same as that in the 50 peak dpa specimen. Fig. 4.42 also shows that the peak swelling for both 50 and 150 peak dpa specimens is located at a depth of ∼500 nm from the surface, whereas the peak dpa occurs at ∼1000 nm. The swelling approaches 0 for regions over ∼800 nm, where the injected ions are distributed. This kind of suppressed swelling behavior in the injected ion region has also been reported by many previous studies on self-ion irradiated F/M steels and ODS F/M steels [78,79], and can be well-explained by the defect imbalance and injected interstitials [80,81].

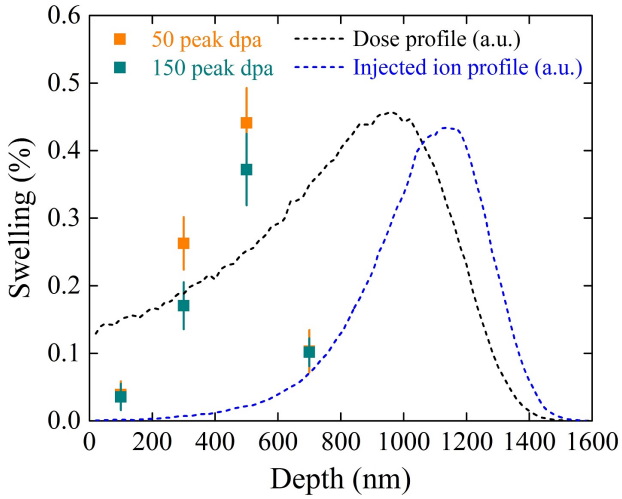

Figure 4.42: Void swelling of A709 irradiated to 50 and 150 peak dpa at 500℃.

For comparison, Fig. 4.43 shows the void distribution in 316H irradiated to 150 peak dpa at 500℃. Similar to A709, the voids were only found in regions with depth less than 750 nm.

A more direct comparison on the voids in A709 with the voids in 316H is shown in Fig. 4.44. Both alloys were irradiated to 150 peak dpa at 500℃. It is easy to see that the voids in A709 are much bigger than those in 316H, and the number density is much lower (roughly by a factor of 3).

The quantitative swelling data of 316H irradiated to 150 peak dpa at 500℃ are listed in Table 4.5. It is easy to see that the highest swelling is located in the

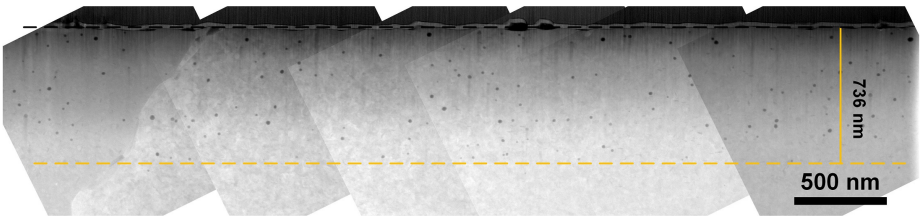

Figure 4.43: STEM HAADF images showing the radiation-induced voids in 316H irradiated to 150 peak dpa at 500℃.

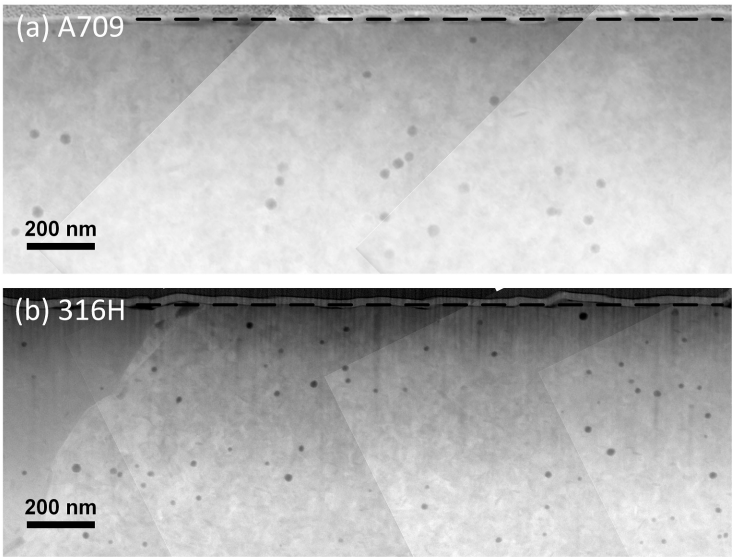

Figure 4.44: STEM HAADF images showing the voids in (a) 316H and (b) A709. Both were irradiated to 150 peak dpa at 500℃.

400–600 nm depth region, and the amount of swelling (0.170%) is lower than that of A709 (0.372%), largely due to the fact that the voids in 316H is only about half the size of the voids in A709.

Table 4.5: Void number density, size, and swelling of 316H irradiated to 150 peak dpa at 500℃.

Depth (nm)	N_{void} ($\times 10^{20}$ /m^3)	d_{void} (nm)	swelling (%)	local dpa
0–200	4.53	16.1 ± 3.7	0.114 ± 0.024	49.5
200–400	4.15	15.2 ± 3.5	0.089 ± 0.017	63.6
400–600	5.98	16.6 ± 4.0	0.170 ± 0.032	84.5
600–800	3.08	14.3 ± 3.0	0.053 ± 0.012	116.5

It should be noted that the less swelling of 316H does not indicate that 316H is superior to A709 in terms of swelling resistance. This is because the two alloys strarted from very different initial conditions. The much higher dislocation density in unirradiated 316H can have significant impacts on the void nucleation and growth. In order to compare these two alloys, the unirradiated 316H should be heat-treated (solution annealing) to similar initial condition as A709, or much higher dose irradiations that are relatively insensitive to the initial conditions need to be carried out. A rigorous comparison on the swelling of these two alloys is not yet available.

4.6 Irradiation hardening

4.6.1 Nanoindentation measurement

All aforementioned microstructural modifications can have impacts on the mechanical properties of irradiated A709. Examples of changes in mechanical properties are increase in the yield strength and loss of fracture toughness.

Here, since the depth of the irradiated region is on the µm scale, nanoindentation was used to measure the changes in hardness in different irradiation conditions. Fig. 4.45 shows the hardness values of A709 irradiated to 10, 50, and 150 peak dpa at 500℃, measured using two different contact depths, ∼165 nm and ∼250 nm. The trend shown by two different depths is similar: sharp increase in hardness at 10 peak dpa, and than gradual increase from 10 peak dpa to 150 peak dpa. The hardness values using ∼165 nm contact depth are consistently higher, which should be due to the well-known indentation size effect.

The temperature dependence and dose dependence of irradiation hardening of A709 is shown in Fig. 4.46, together with the data of 316H. The contact depth is ∼250 nm for all measurements.

From Fig. 4.46, it is easy to see that the hardness of unirradiated 316H is higher than A709, which should be due to the much higher dislocation density in 316H before irradiation. At the lowest dose (10 peak dpa), the irradiated hardness of A709 is almost the same as 316H, as shown in Fig. 4.46 (a). At

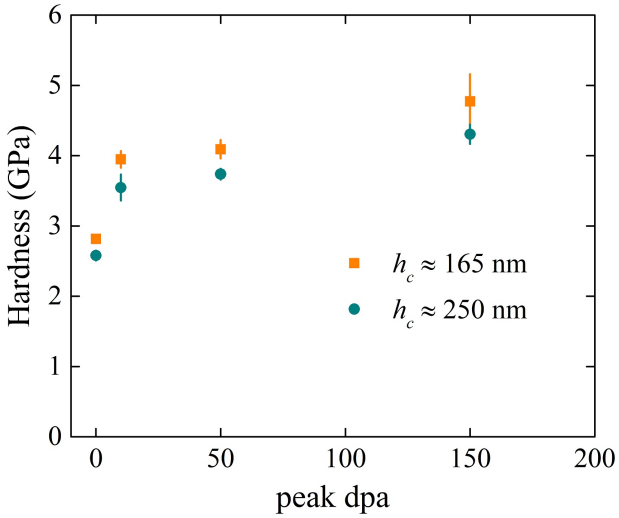

Figure 4.45: Hardness data of A709 irradiated at 500℃, measured at two different contact depths.

500℃, the hardness of A709 is higher than that of 316H at higher doses, as shown in Fig. 4.46 (b). The hardness values are also tabulated in Tables. 4.6–4.8.

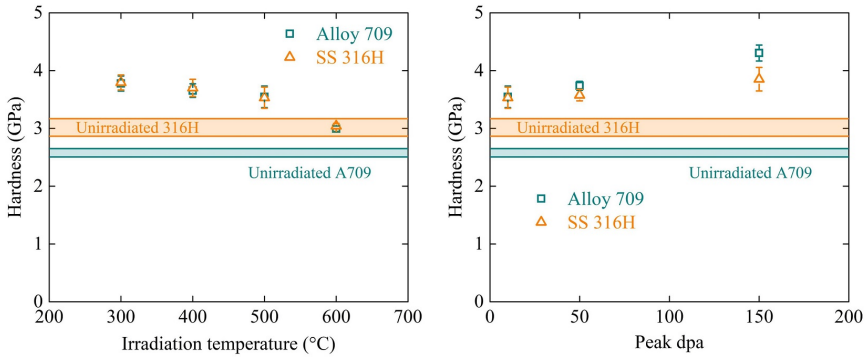

Figure 4.46: Hardness of A709 vs 316H at different irradiation conditions: (a) temperature dependence at 10 peak dpa, and (b) dose dependence at 500℃.

4.6.2 Modeling of irradiation hardening

Up to now, we have both microstructure information and hardness measurement from nanoindentation. It is then possible to correlate the microstructure

Table 4.6: Nanoindentation data of A709 irradiated at 500℃, measured at two different contact depths.

Dose	h_c (nm)	Hardness (GPa)	E_r (GPa)	h_c (nm)	Hardness (GPa)	E_r (GPa)
unirradiated	173.0	2.82 ± 0.04	159.1 ± 5.9	260.4	2.58 ± 0.07	150.8 ± 5.9
10 peak dpa	166.1	3.95 ± 0.12	199.0 ± 8.2	252.7	3.55 ± 0.19	191.6 ± 7.0
50 peak dpa	163.7	4.09 ± 0.13	180.6 ± 3.4	251.3	3.74 ± 0.08	175.2 ± 3.1
150 peak dpa	160.3	4.77 ± 0.39	183.5 ± 11.5	247.5	4.30 ± 0.14	178.4 ± 3.7

Table 4.7: Nanoindentation data of A709 vs 316H irradiated to 10 peak dpa at different temperatures.

	A709			316H		
$T_{irr.}$ (℃)	h_c (nm)	Hardness (GPa)	E_r (GPa)	h_c (nm)	Hardness (GPa)	E_r (GPa)
unirradiated	260.4	2.58 ± 0.07	150.8 ± 5.9	257.7	3.02 ± 0.15	173.2 ± 5.8
300	251.3	3.78 ± 0.13	203.4 ± 6.7	251.3	3.79 ± 0.13	203.9 ± 6.7
400	252.7	3.65 ± 0.12	196.9 ± 5.2	252.9	3.70 ± 0.15	193.6 ± 4.0
500	252.7	3.55 ± 0.19	191.6 ± 7.0	253.5	3.53 ± 0.18	177.1 ± 6.9
600	255.1	2.99 ± 0.05	143.1 ± 2.1	259.3	3.04 ± 0.04	187.0 ± 8.1

Table 4.8: Nanoindentation data of A709 vs 316H irradiated to different doses at 500℃.

	A709			316H		
Dose	h_c (nm)	Hardness (GPa)	E_r (GPa)	h_c (nm)	Hardness (GPa)	E_r (GPa)
unirradiated	260.4	2.58 ± 0.07	150.8 ± 5.9	257.7	3.02 ± 0.15	173.2 ± 5.8
10 peak dpa	252.7	3.55 ± 0.19	191.6 ± 7.0	253.5	3.53 ± 0.18	177.1 ± 6.9
50 peak dpa	251.3	3.74 ± 0.08	175.2 ± 3.1	253.0	3.58 ± 0.10	183.2 ± 5.9
150 peak dpa	247.5	4.30 ± 0.14	178.4 ± 3.7	247.3	3.85 ± 0.20	158.6 ± 6.6

with the nanoindentation measured hardness.

For nanoindentation, a contact depth of ∼250 nm was chosen as a compromise to minimize the size effect for shallow indents and the substrate effect for deep indents. It should be noted that at a contact depth of 250 nm, a rough estimation of the plastic region is about 5 times the contact depth, or ∼1250 nm. Therefore, the nanoindenation measurement basically samples the entire volume of the irradiated region. Considering that the defect distribution along the depth direction can be non-uniform, we need to average over the entire irradiated region. We also limit our analysis to the lowest dose and also the simplest case in which dislocations and/or dislocation loops are the major contributor to irradiation hardening. Table 4.9 lists the quantitative TEM data on the defect measurements. The data for 300℃ are from *in situ* TEM irradiation at 5 dpa shown in Fig. 4.5, and it is assumed the network dislocation structure is uniform along the irradiation depth direction. The data for 400–600℃ are from *ex situ* bulk irradiation to 10 peak dpa, and are averaged over the entire irradiated region. It should be noted that in Table 4.9, the dislocation density is twice the measured density, since half $a_0/2\langle 110\rangle$ dislocations are invisible under the diffraction condition in Fig. 4.5, and the Frank loop density is four times the measured density, since only one of the four $\{111\}$ variants is visible in rel-rod DF TEM images.

Table 4.9: TEM data of A709 irradiated at 300–600℃.

Temperature	Loop size (nm)	Loop density (10^{21} m^{-3})	Dislocation density (10^{14} m^{-2})
300	4.85 ± 1.47	4.51	2.62
400	15.83 ± 6.44	20.85	–
500	19.41 ± 11.07	9.221	–
600	30.13 ± 32.44	2.71	–

Note: Loops at 300℃ are black-dots, and at 400–600℃ refer to Frank loops. 300℃ data are from *in situ* TEM irradiation at 5 dpa, and 400–600℃ data are from *ex situ* bulk irradiation at 10 peak dpa, or 5.75 dpa averaged over the entire irradiated region.

The dispersed barrier hardening model has been used in previous studies [27, 30, 34, 82–86] to establish the microstructure-property relationship and to evaluate the hardening induced by neutron and ion irradiations. According to the dispersed barrier hardening model, the change in yield strength $\Delta\sigma_Y$ due to dislocation loops and line dislocations is given by:

$$\Delta\sigma_Y = M\alpha_L\mu b\sqrt{\rho_L d_L} + M\alpha_D\mu b(\sqrt{\rho_D^{irr.}} - \sqrt{\rho_D^{unirr.}}) \tag{4.2}$$

where M is the Taylor factor, α is the defect barrier strength, μ is the shear modulus, b represents the magnitude of the Burgers vector of dislocations, ρ_L is the loop density, d_L is the loop size, $\rho_D^{irr.}$ is the dislocation density after irradiation, and $\rho_D^{unirr.}$ is the dislocation density before irradiation.

Table 4.10 lists the values of the parameters used in our calculations, which are consistent with the values used in Fe–Cr–Ni alloys [87–89].

Table 4.10: List of the parameters used in the dispersed barrier hardening model.

Parameter	Value
Taylor factor, M	3.06
Shear modulus, μ	82 GPa [87]
Magnitude of Burgers vector of dislocations, b	0.254 nm
Barrier strength of dislocations, α_D	0.2 [87, 89]
Barrier strength of Frank loops and black-dots, α_L	0.3 [88]

The change in yield strength $\Delta\sigma_Y$ is then correlated to change in Vickers hardness ΔH_V by [90]:

$$\Delta\sigma_Y = 3.03\Delta H_V \tag{4.3}$$

The Vickers hardness H_V is in unit of kgf/mm^2, and is related to the nanohardness H by [91, 92]:

$$H_V = 0.0945H \tag{4.4}$$

Fig. 4.47 shows the change in hardness from nanoindentation measurements vs that from microstructure-based calculations. The calculated ΔH agrees well with the measurements, especially considering the complications due to size effect, substrate effect, and nonuniform defect distribution in the nanoindentation experiments. The microstructure-based calculations only considered contributions from dislocation loops and network dislocations, RIS of Ni and Si was observed but not considered here.

Both measured ΔH and calculated ΔH decreases with increasing temperature, which is also consistent with the typical behavior of irradiation hardening.

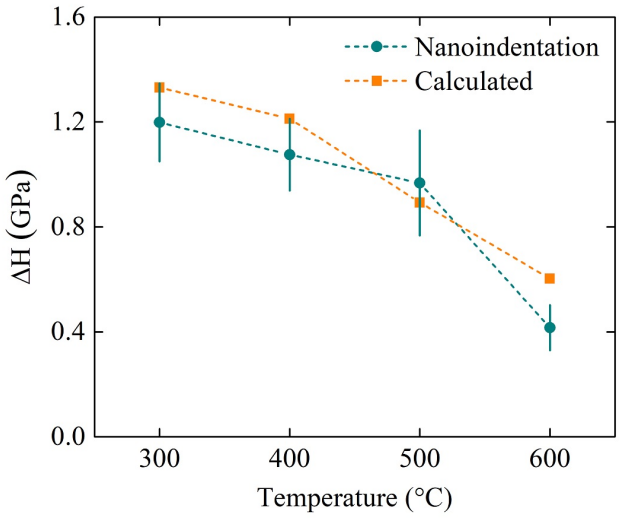

Figure 4.47: Comparison of measured changes in hardness with microstructure-based calculations.

5. RADIATION RESPONSE OF F/M STEELS T91 AND G92

The typical microstructure of F/M steels consists of martensite laths, as illustrated in Fig. 5.1. T91 and G92 are both F/M steels with dominant martensite microstructure. Fig. 5.2 shows the microstructure of T91. The lath martensite structure with $M_{23}C_6$ decorating lath/grain boundaries can be clearly seen.

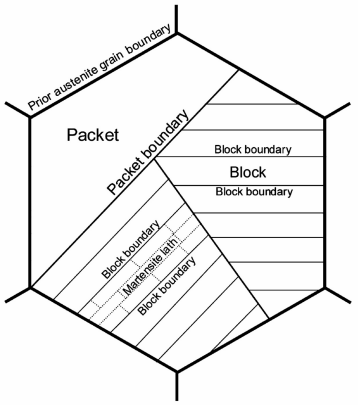

Figure 5.1: Illustration of the martensite lath structure [93].

5.1 Microstructural evolution under heavy ion irradiation

The real-time microstructural evolution of T91 irradiated up to 4.2×10^{15} ions/cm^2 ($\sim$7 dpa) at three different temperatures (300, 400, and 500℃) is shown in Figs. 5.3–5.5. From these TEM micrographs, it is found that irradiation-induced dislocation loops began to show up at approximately 1 dpa and loop density increased by 1–2 orders of magnitude from 1 dpa to 3 dpa. After the density of dislocation loops reached about 2×10^{21} m^{-3} to 4×10^{21} m^{-3}, the interactions of these loops with grown-in defects (line dislocations or grain boundaries) became apparent, as manifested by the changes in grown-in defects

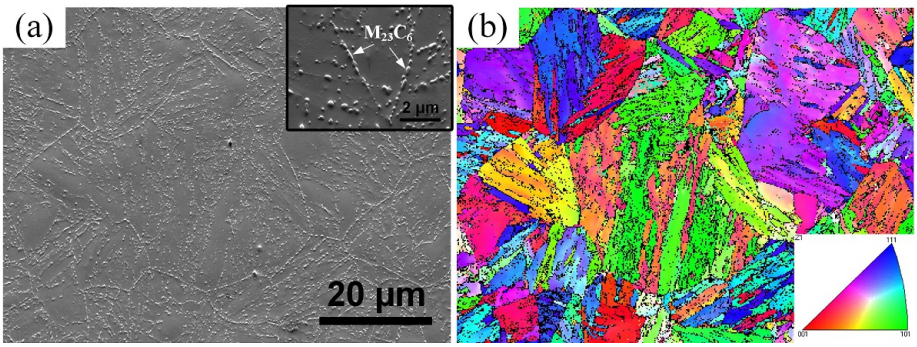

Figure 5.2: The microstructure of T91: (a) SEM image with insertion showing $M_{23}C_6$ precipitates at lath/grain boundaries, and (b) EBSD IPF map showing the martensite lath structure.

shown in Figs. 5.3–5.5.

For the specimen irradiated at 300℃, the microstructure evolution is shown in Fig. 5.3. All the TEM micrographs in Fig. 5.3 were taken under nearly identical kinematical diffraction conditions, in which the sample was tilted near the [001] zone and only $\mathbf{g}_{110}$ was strongly excited. As can be seen, several black-dot dislocation loops formed at 1 dpa. Examples are the ones marked by red arrows in Fig. 5.3 (b). From 1 to 3 dpa, the loop density increased significantly from 6.3 $\times$ 10^{20} m^{-3} to 3.8 $\times$ 10^{21} m^{-3}. Although the loop distribution was relatively uniform, i.e. no apparent dislocation decoration occurred, strong interactions between grown-in line dislocations and irradiation-induced dislocation loops occurred. Some line dislocations were completely altered and they linked together with surrounding defects. An example is shown in the blue circle in Fig. 5.3, where gradual changes in the morphology of a dislocation can be readily seen. Observable changes also occurred in the lath boundary shown in Fig. 5.3. As the dose increased, increasing numbers of dislocation segments attached to the lath boundary.

Fig. 5.4 shows the evolution of grown-in line dislocations and irradiation-induced dislocation loops in the specimen irradiated at 400℃. Similarly, only a few loops were observed at 1 dpa, and the loop density is estimated to be around 4 $\times$ 10^{20} m^{-3}. Some of the loops were indicated by red arrows in Fig. 5.4 (b). Similar to the 300℃ case, noticeable increase (by a factor of $\sim$10) in the loop density was observed between 1 dpa and 3 dpa. In Fig. 5.4 (c)–(e), both black dots and extended loops were observed, and some of them were marked by red arrows. In Fig. 5.4 (d) and (e), dislocation segments (some were marked by red arrows) formed by coalescence of adjacent dislocation loops and/or line dislocations. The dislocation structure at 7 dpa did not show any apparent alignment. After 3 dpa, strong interaction between preexisting line dislocations and dislocation loops occurred, as shown in the changes in the dislocations D_1 and D_2 in Fig. 5.4 (d) and (e). Several jogs/kinks (marked

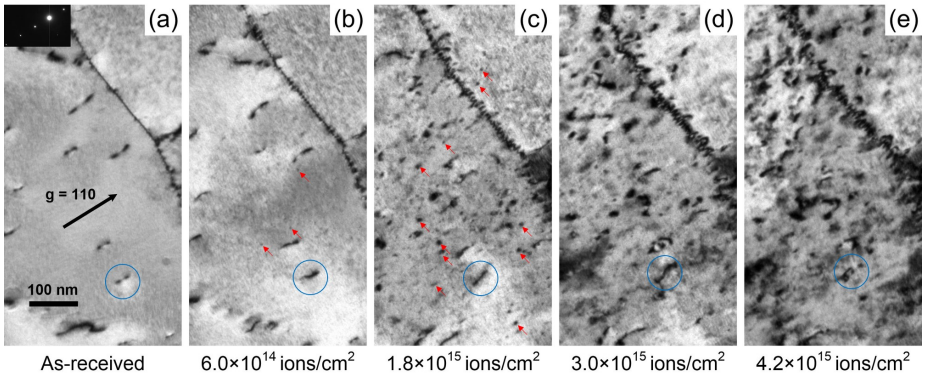

Figure 5.3: TEM bright field images showing the dislocation loop formation and development in T91 thin foil irradiated by 1 MeV Kr^{++} ions at 300°C at different doses: (a) as-received, (b) 6.0×10^{14} ions/cm^2 (1 dpa), (c) 1.8×10^{15} ions/cm^2 (3 dpa), (d) 3.0×10^{15} ions/cm^2 (5 dpa), and (e) 4.2×10^{15} ions/cm^2 (7 dpa). All the images were taken near the [001] zone.

by blue triangles) in dislocation D_1 were observed, and apparent changes in the curvature of dislocation D_2 can be readily seen. These complex changes indicate dislocation climb by absorbing point defects and maybe further interactions with dislocation loops as well. Similar jogs/kinks and changes in curvature have also been reported in lower dose ion irradiated Fe–Cr model alloys [94].

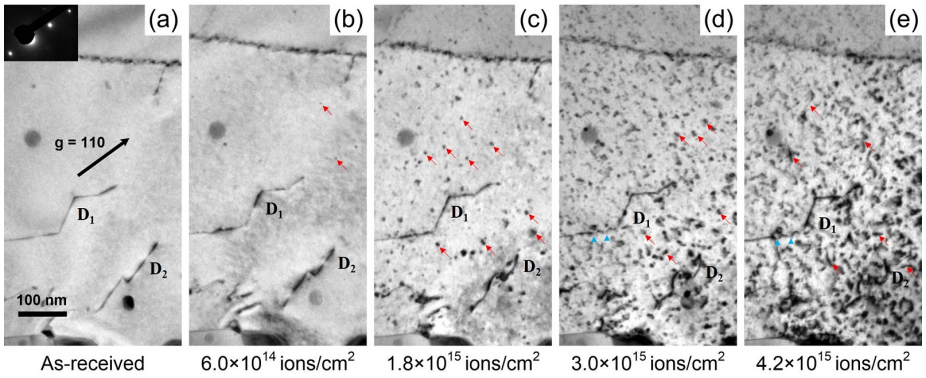

Figure 5.4: TEM bright field images showing the dislocation loop formation and development in T91 thin foil irradiated by 1 MeV Kr^{++} ions at 400°C at different doses: (a) as-received, (b) 1 dpa, (c) 3 dpa, (d) 5 dpa, and (e) 7 dpa. All the images were taken near the $[1\bar{1}0]$ zone.

For the 500°C case, Fig. 5.5 shows the microstructure evolution of a dislocation-rich region. As can be seen, little dislocation loops were observed at 1 dpa. At 3 dpa, most dislocation loops were black-dots. At 5 dpa, some black-dots grew

into much larger dislocation loops. The loops in the lower part of Fig. 5.5 (d) had the same Burgers vector and were well-aligned. Localized interactions between irradiation-induced dislocation loops and grown-in dislocations were again observed in Fig. 5.5 (c) to (e). After irradiation, both isolated loops and dislocation segments were found and no obvious dislocation network was observed.

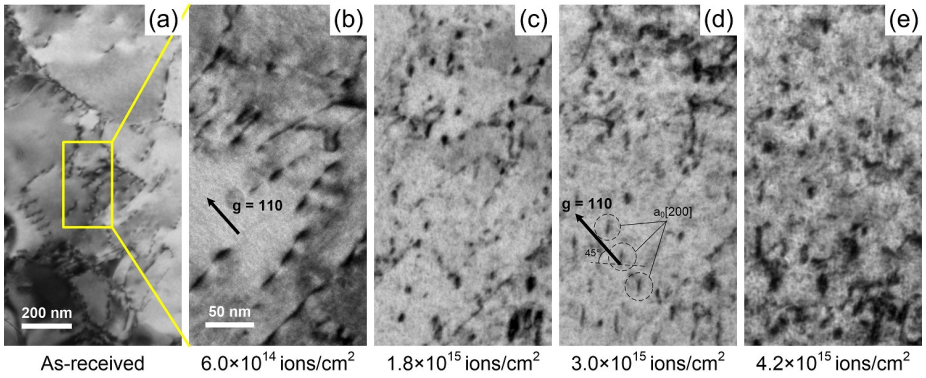

Figure 5.5: TEM bright field images showing the dislocation loop formation and development in T91 thin foil irradiated by 1 MeV Kr^{++} ions at 500℃ at different doses: (a) as-received, (b) 1 dpa, (c) 3 dpa, (d) 5 dpa, and (e) 7 dpa. All the images were taken near the [001] zone.

Similar *in situ* TEM ion irradiation experiments were also carried out for F/M steel G92. Fig. 5.6 shows the microstructural evolution of G92 irradiated at 300℃ up to 7 dpa. Similar to T91, black-dot dislocation loops started to occur at 1 dpa, and the loop density increased significantly from 1 dpa to 3 dpa. In addiation to the black-dot loops, dense network dislocation was observed after 5 dpa.

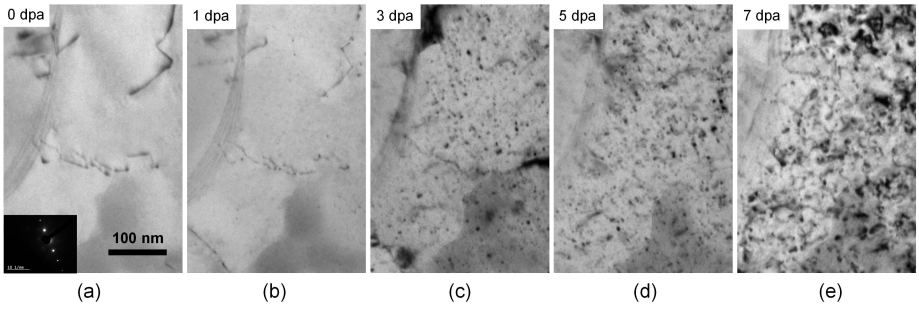

Figure 5.6: TEM bright field images showing the dislocation loop formation and development in G92 thin foil irradiated by 1 MeV Kr^{++} ions at 300℃ at different doses: (a) as-received, (b) 1 dpa, (c) 3 dpa, (d) 5 dpa, and (e) 7 dpa.

The microstructure evolution of G92 irradiated at 500℃ is shown in Fig. 5.7. Similar to T91, almost no dislocation loops were observed at 1 dpa. Extended large loops were observed in G92 at 3 dpa. At higher doses, aligned loops were observed, as shown in Figs. 5.7 (d) and (e).

Based on aftermentioned observations, our current results of G92 and T91 show similar temperature dependence: black-dot dislocation loops and network dislocations at lower temperature (300℃), and aligned (possibly $a_0\langle 100\rangle$ type) large loops at higher temperature (500℃). However, quantitative comparison on the defect structure (loop size, loop density, dislocation density) of these two alloys is not yet available.

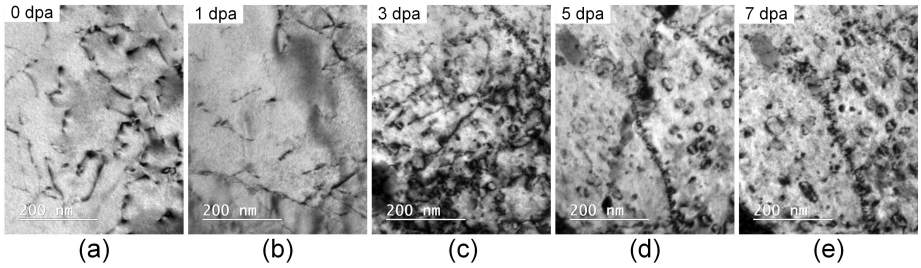

Figure 5.7: TEM bright field images showing the dislocation loop formation and development in G92 thin foil irradiated by 1 MeV Kr^{++} ions at 500℃ at different doses: (a) as-received, (b) 1 dpa, (c) 3 dpa, (d) 5 dpa, and (e) 7 dpa.

It should be noted that the physical processes of thin foil irradiation experiments could differ from bulk irradiation experiments, largely due to the two nearby surfaces of TEM thin foils. The free surfaces can act as sinks and remove a portion of the mobile defects such as $a_0/2\langle 111\rangle$ loops. In the in situ irradiation study of Fe–Cr–Ni austenitic steels at 450℃ [95], 20 nm was subtracted considering the depletion of defects near surfaces. Compared to austenitic steels, F/M steels have much lower defect mobility and high-density internal dislocation sinks, this effect is expected to be much less. The surface effects were not studied for F/M steels.

5.2 $\langle 111\rangle$–$\langle 100\rangle$ loop transition

Previous studies reported that the dislocation loops induced by both ion and neutron irradiations in α-iron, Fe–Cr model alloys, and F/M steels are $a_0\langle 100\rangle\{100\}$ or $a_0/2\langle 111\rangle\{111\}$ type [23–30,32,96,97]. Here, it is also assumed that all the loops are $a_0\langle 100\rangle\{100\}$ or $a_0/2\langle 111\rangle\{111\}$ type. The Burgers vectors of dislocations loops were be determined using bright-field TEM images taken under selected diffraction conditions. $a_0\langle 100\rangle\{100\}$ and $a_0/2\langle 111\rangle\{111\}$ loops can be distinguished by (1) standard $\mathbf{g}\cdot\mathbf{b}$ Burgers vector analysis or (2) habit plane analysis by comparing the orientation of the loops with respect to the diffraction vectors.

Fig. 5.8 shows the dislocation loops in a T91 specimen that was irradiated to 7 dpa at 500℃. Fig. 5.8 (a)–(c) were obtained by tilting the specimen to different diffraction conditions near the [001] zone. In Fig. 5.8 (a), only $\mathbf{g}_{020}$ was strongly excited, therefore only $a_0[001]$ and $a_0[100]$ loops are invisible ($\mathbf{g} \cdot \mathbf{b} = 0$) and all other types of loops ($a_0[010]$ and all $a_0/2\langle 111\rangle$ loops) should be visible. However, only $a_0[010]$ loops marked as "a" showed up in Fig. 5.8 (a), indicating that there was no $a_0/2\langle 111\rangle$ loops in this area. Both $a_0[100]$ and $a_0[010]$ loops are visible in Fig. 5.8 (b) and (c) since $\mathbf{g} \cdot \mathbf{b} \neq 0$. The loop marked as "b" showed up in Fig. 5.8 (b) and (c) but disappeared in Fig. 5.8 (a), indicating that it is a $a_0[100]$ loop. Comparing Fig. 5.8 (a)–(c), it was found that after irradiation to 7 dpa at 500℃, the dislocation loops are dominantly $a_0[010]$ type in this area. Since these loops have the same Burgers vector, they were well-aligned as shown in Fig. 5.8. Similar TEM examinations were carried out in other grains, and the loops were also found to be dominantly $a_0\langle 100\rangle$ type. Similar grain-level localized loop alignment was commonly observed and should be characteristic for the irradiation at 500℃.

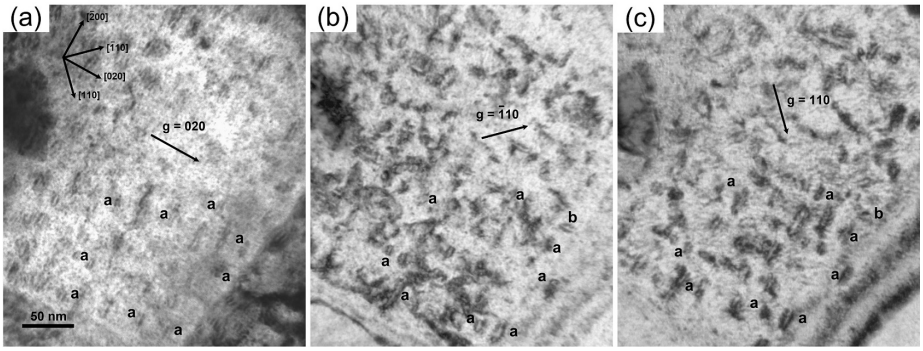

Figure 5.8: Dislocation loops in T91 irradiated to 7 dpa at 500℃ imaged using (a) $\mathbf{g}_{020}$, (b) $\mathbf{g}_{\bar{1}10}$, and (c) $\mathbf{g}_{110}$. The zone axis is [001].

For the 400℃ irradiation, however, distinct dislocation microstructure was observed. Fig. 5.9 shows the typical microstructure found in the specimen irradiated to 7 dpa at 400℃. The overall dislocation structure is shown in Fig. 5.9 (a). Fig. 5.9 (b)–(d) are enlarged TEM images showing the individual loops. All images was taken near the [001] zone and only $\mathbf{g}_{110}$ was strongly excited, as shown in the insertion in Fig. 5.9 (a). Under this diffraction condition, visible loops are $a_0[010]$, $a_0[100]$, $a_0/2[111]$, $a_0/2[11\bar{1}]$, $a_0/2[1\bar{1}1]$, and $a_0/2[\bar{1}11]$. The $a_0[010]$ and $a_0[100]$ loops can be easily distinguished from $a_0/2\langle 111\rangle$ loops by their orientations with respect to the diffraction vectors, i.e. $a_0[010]$ loops are perpendicular to $\mathbf{g}_{020}$ and 45° to $\mathbf{g}_{110}$, $a_0[100]$ loops are parallel to $\mathbf{g}_{020}$ and 45° to $\mathbf{g}_{110}$. Moreover, $a_0\langle 100\rangle$ loops are close to edge-on since the images were taken near the [001] zone axis. The loops in Fig. 5.9 (b)–(d) were distinguished by this method. The ones in red circles are $a_0\langle 100\rangle$ loops, and the ones in blue circles are $a_0/2\langle 111\rangle$ loops. Counting only the well-resolved loops in the three

areas near Fig. 5.9 (b)–(d), statistical data of the Burgers vector are shown in Table 5.1. It is estimated that the $\langle 111 \rangle / \langle 100 \rangle$ ratio is around 1.02 ± 0.38 for 400℃ irradiation.

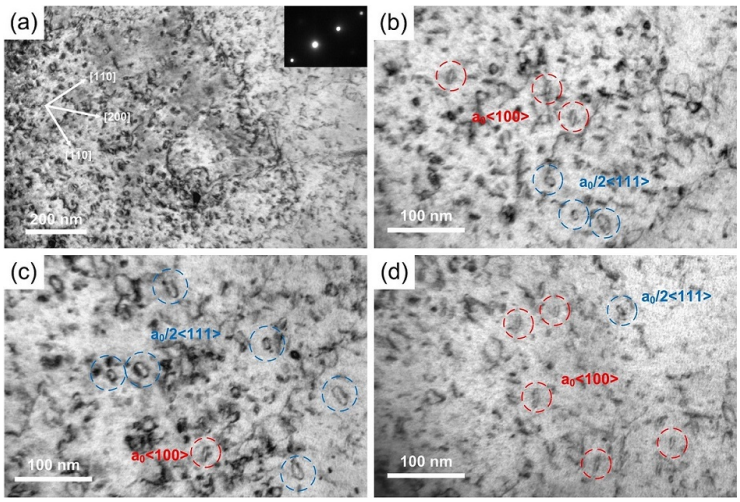

Figure 5.9: Dislocation loops in T91 irradiated to 7 dpa at 400℃: (a) low-mag image showing the overall microstructure, (b) an area with both loops, (c) an area with more $a_0/2\langle 111 \rangle$ loops, and (d) an area with more $a_0\langle 100 \rangle$ loops. All the images were taken near [001] zone with only $\mathbf{g}_{110}$ strongly excited.

Table 5.1: Statistical analysis of $a_0/2\langle 111 \rangle$ and $a_0\langle 100 \rangle$ loops in T91 irradiated to 7 dpa at 400℃.

	No. of $a_0/2\langle 111 \rangle$ loops	No. of $a_0\langle 100 \rangle$ loops	$\langle 111 \rangle / \langle 100 \rangle$ ratio
Area 1	20	17	1.18
Area 2	14	10	1.40
Area 3	13	19	0.68
Total	47	46	1.02 ± 0.38

The stability of $a_0\langle 100 \rangle$ loops with respect to $a_0/2\langle 111 \rangle$ loops is highly temperature dependent. Yao *et al.* performed self-ion irradiation on pure Fe and reported that about 80% of the loops were of the $a_0\langle 100 \rangle$ type at 400℃ [32]. In the present work, both $a_0\langle 100 \rangle$ and $a_0/2\langle 111 \rangle$ loops were found at 300℃, the ratio was not determined. However, based on the fact that only at 300℃, loops were observed to escape to the surface and disappeared, the fraction of mobile $a_0/2\langle 111 \rangle$ loops at 300℃ should be higher than 400 and 500℃, since $a_0\langle 100 \rangle$ loops are sessile and were not expected to move or escape to the surface. At 400℃, the ratio of $a_0/2\langle 111 \rangle$ to $a_0\langle 100 \rangle$ loops is around 1.02. At 500℃, the loops were found to be predominantly $a_0\langle 100 \rangle$ type. Based on our results at three different temperatures, the $a_0/2\langle 111 \rangle$–$a_0\langle 100 \rangle$ loop transition is confirmed. Although at 400℃, only ∼49% of the loops are $a_0\langle 100 \rangle$ type, different from the

80% in pure iron reported by Yao et al. [32], the general trend is consistent. The difference could be due to the effect of alloying elements such as chromium, as previous studies suggest that the addition of chromium tends to equalize the proportion of $a_0/2\langle 111\rangle$ and $a_0\langle 100\rangle$ loops [34], or to increase the fraction of $a_0/2\langle 111\rangle$ loops [31].

The observed loop transition has significant effects on the microstructural evolution. Fig. 5.10 shows the representative dislocation structure of T91 steel irradiated to 4.2×10^{15} ions/cm^2 at 300, 400, and 500℃, respectively. Dislocation networks were commonly found in the sample irradiated at 300℃, as shown in Fig. 5.10 (a). Some black-dot dislocation loops are also observed in addition to the network dislocations. In contrast to the dislocation network in Fig. 5.10 (a), isolated dislocation loops were commonly found in the samples irradiated at 400 and 500℃, as shown in Fig. 5.10 (b) and (c). However, the difference is that the dislocation loops in Fig. 5.10 (b) are randomly oriented, whereas the dislocation loops in Fig. 11 (c) are well-aligned.

The temperature dependence of the observed dislocation structures can be explained by the $a_0/2\langle 111\rangle$–$a_0\langle 100\rangle$ loop transition. At elevated temperatures, the $a_0/2\langle 111\rangle$ loops are highly mobile and $a_0\langle 100\rangle$ loops are sessile. Therefore, $a_0/2\langle 111\rangle$ loops can migrate over long distances and interact with distant grown-in defects, leading to the faster formation of dislocation segments and network dislocations at lower dose, whereas $a_0\langle 100\rangle$ can only act as stationary defect sinks once formed. If the $a_0\langle 100\rangle$ loops happen to form near grown-in defects, localized interaction between loops and nearby grown-in defects is possible. As an example, Fig. 5.4 shows clearly the process of localized interactions.

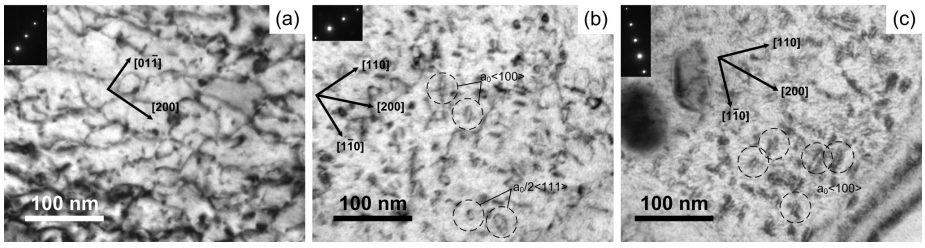

Figure 5.10: TEM BF images showing different dislocation structures in T91 irradiated by1.0 MeV Kr^{++} ions to 7 dpa at different temperatures: (a) dislocation network decorated by black-dot loops at 300℃, (b) randomly distributed $a_0\langle 100\rangle$ and $a_0/2\langle 111\rangle$ loops at 400℃, and (c) well-aligned $a_0\langle 100\rangle$ loops at 500℃.

5.3 Irradiation hardening

5.3.1 Modeling of irradiation hardening

In order to quantitatively characterize the irradiation-induced dislocation loops and estimate the increase in yield strength, the average loop sizes and densities were obtained. For the loop size measurement, TEM kinematic bright field images were used. Therefore, the results might be not very accurate for loops less than 10 nm, especially for the small black-dot loops around 2 nm. On average, 40–60 loops were measured for each dose and temperature condition to reduce the statistical errors. Figs. 5.11–5.13 show the histograms of the loop size distribution for the irradiation at 300, 400, and 500℃, respectively.

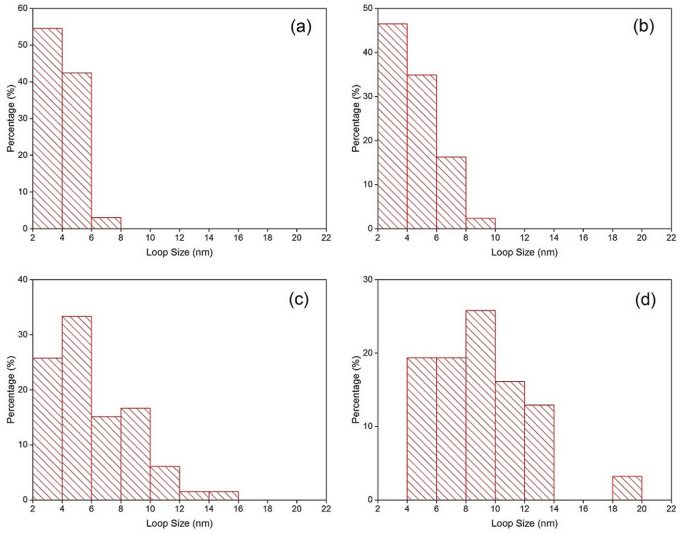

Figure 5.11: Loop size distribution histograms of T91 irradiated at 300℃ at different doses: (a) 1 dpa, (b) 3 dpa, (c) 5 dpa, and (d) 7 dpa.

At 300℃, the loops did not show significant increase in size, as shown in Fig. 5.11. Most loops are small black-dots and only a few extended loops around 6–10 nm were found at 5 dpa and 7 dpa. At 400℃, the loops also started as black-dots around 2 nm at 1 dpa, but the loop size increased significantly as the dose increased, and loops larger than 10 nm were commonly found at 7 dpa. At 500℃, few black-dots were observed at 1 dpa and therefore no size histogram was obtained. Large isolated loops around 20 nm were commonly found at 7 dpa. Based on these histograms, the average loop sizes were plotted in Fig. 5.14 (a), in which the error bars were calculated using the Student t-distribution and represent the 95% confidence interval. In addition to the loop size, the loop density as well as line dislocation density were also obtained, as

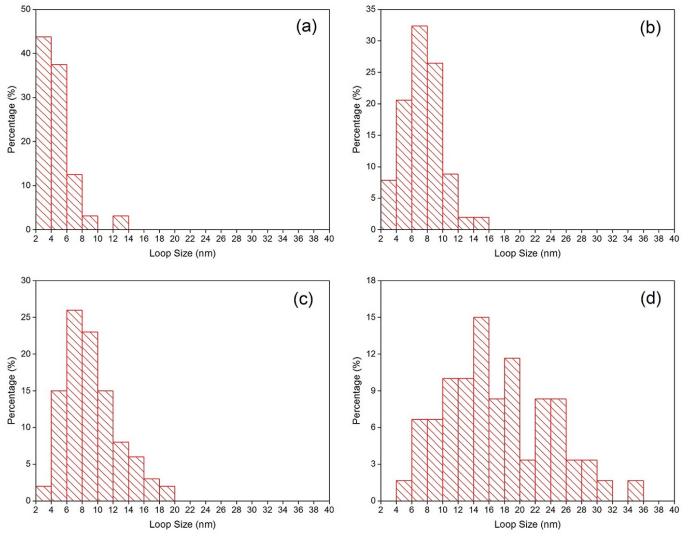

Figure 5.12: Loop size distribution histograms of T91 irradiated at 400℃ at different doses: (a) 1 dpa, (b) 3 dpa, (c) 5 dpa, and (d) 7 dpa.

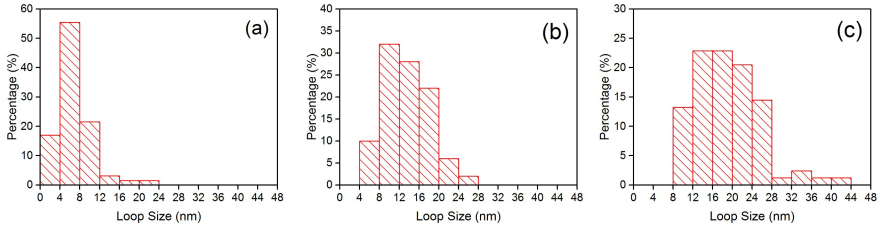

Figure 5.13: Loop size distribution histograms of T91 irradiated at 500℃ at different doses: (a) 3 dpa, (b) 5 dpa, and (c) 7 dpa.

shown in Fig. 5.14 (b). It should be noted that during the in situ irradiations, the thinner areas near the hole created by jet-polishing were bended significantly. All the TEM examinations were conducted on thick enough regions (not too thin to avoid bending, and not too thick to get good contrast). For the loop density calculation, all the sample thickness was assumed to be 100 nm, which is apparently a rough estimate. This uncertainty only affects the loop density calculation, since the line dislocation density is only related to the area of the chosen regions. In the line dislocation density calculation, both grown-in dislocations and dislocation segments formed from irradiation were taken into account. As shown in Fig.5.14 (b), for the 300℃ irradiation, the loop density began to drop between 3 dpa and 5 dpa, accompanied by a steady increase in the line dislocation density. At 400℃, the drop in loop density occurred between 5 dpa and 7 dpa, whereas the line dislocation density showed appreciable increase between 3 dpa and 5 dpa, due to the formation of dislocation segments. For the irradiation at 500℃, the loop density increased significantly between 1 dpa and 3 dpa and then dropped, and the line dislocation density slightly decreased between 3 dpa and 7 dpa. Another finding is that at 1 dpa, the loop density at 500℃ is significantly lower (by as much as an order of magnitude) than that at 300℃ and 400℃.

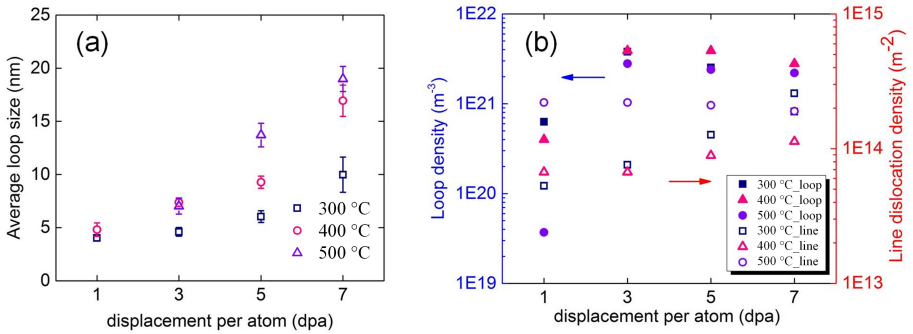

Figure 5.14: Statistical information of defects in T91 irradiated at different temperatures and doses: (a) average loop sizes, and (b) average line dislocation densities and loop densities.

Heavy ion irradiation are frequently employed to emulate neutron irradiation due to the degree of similarity in their weighted average recoil spectra [98]. The disadvantage of heavy ion irradiation is that it produces a non-uniform dose profile over a shallow region (less than 600 nm for 1Me Kr ions) beneath the sample surface. Our in situ TEM observation avoided this problem since the thickness of thin area is about 100 nm, where the dose profile can be approximated to be constant. The difficulty lies in that it is impossible to directly measure the mechanical properties by small scale tests such as nanoindentation, due to various factors contributing to the measurements. The results of shal-

low (less than 100 nm) indents will be largely influenced by the size effect and deeper indents will inevitably sample the whole non-uniform dose profile [99]. Quantitative comparison of the results of small scale tests on heavy ion irradiated samples with the data from neutron irradiated samples seems to be very challenging.

Alternatively, based on the observed defect microstructure it is possible to calculate the mechanical properties such as change in yield strength $\Delta\sigma_Y$ using well-accepted models. Recall the dispersed barrier hardening model in Eq. 4.2, for T91, we use $M = 3.06$, $\mu = 82$ GPa, and $b = 2.49$ nm, which are consistent with the values used in Fe–Cr alloys [27, 30, 34, 84, 86].

In general, the irradiation hardening results from multiple microstructure modifications under energetic ion/neutron bombardment, including voids, precipitates, dislocation loops, line dislocations, etc. The overall effect on the yield strength can be evaluated by the linear superposition of the contributions from various defects: $\Delta\sigma_Y = \Delta\sigma_{YV} + \Delta\sigma_{YP} + \Delta\sigma_{YL} + \Delta\sigma_{YD} + \Delta\sigma_{YR}$, where $\Delta\sigma_{YV}$, $\Delta\sigma_{YP}$, $\Delta\sigma_{YL}$, $\Delta\sigma_{YD}$ and $\Delta\sigma_{YR}$ represent the contribution from voids, precipitates, dislocation loops, line dislocations, and others (such as dislocation decoration, segregation of solute atoms), respectively.

In the case of T91, no obvious voids or irradiation-induced α' precipitates were observed during the in situ irradiation. This is also consistent with the observations in previous studies [82, 100, 101]. The favorable explanation is that 9–12%Cr F/M steels are well known for their excellent swelling resistance [102] and the final dose (7 dpa) is still in the transient regime [5]. Thus, only negligible amount of voids is expected at the final dose. Also, the Cr content is 9.24 wt.%, which is close to the threshold value for α–α' phase separation in Fe–Cr alloys [35], indicating very few, if any, α' precipitates are expected. Indeed, no α' precipitates were reported in F/M steel T91 after proton irradiation to 10 dpa at 400–500℃ or neutron irradiation up to 184 dpa at 413℃.

As a first order approximation, the contribution from voids and α' precipitates is neglected due to their marginal amount and small barrier strength [85, 86]. $\Delta\sigma_{YR}$ is also ignored for simplicity. Then we have the same equation as Eq. 4.2:

$$\Delta\sigma_Y = \Delta\sigma_{YL} + \Delta\sigma_{YD} = M\alpha_L\mu b\sqrt{\rho_L d_L} + M\alpha_D\mu b(\sqrt{\rho_D^{irr.}} - \sqrt{\rho_D^{unirr.}}) \quad (5.1)$$

where α_L, ρ_L, and d_L are the barrier strength, average density, and average size of dislocation loops, respectively; α_D is the barrier strength of line dislocations, $\rho_D^{irr.}$ and $\rho_D^{unirr.}$ are the line dislocation densities after and before irradiation, respectively. Here $\alpha_D = 0.64$ and α_L is temporarily taken to be 0.40, which are consistent with the values used in literature.

Using the loop sizes and loop/line dislocation densities, the dose dependence and temperature dependence of the increase in yield strength $\Delta\sigma_Y$ are shown in Figs. 5.15 and 5.16, respectively. Existing experimental data [17, 82, 103, 104] are also shown. For simplicity, only data at similar temperatures (∼300, 400, and 500℃) were shown in Fig.5.15 and only data in the similar dose range (7–12 dpa) were shown in Fig. 5.16. It is easy to see that the general trend is

consistent with the conventional irradiation hardening characteristics of F/M steels, i.e. more pronounced hardening at lower irradiation temperatures and earlier saturation at higher irradiation temperatures.

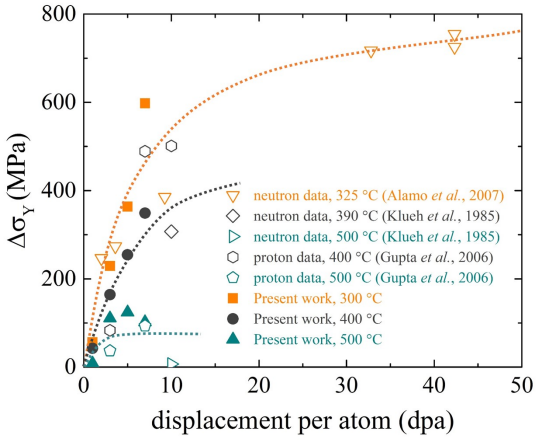

Figure 5.15: Change in yield strength $\Delta\sigma_Y$ as a function of dose. Two sets of proton data [82] and three sets of neutron data [17, 103, 104] at similar temperatures are also shown. The dotted lines are for visual aide only.

As can be seen in Fig. 5.15, there is noticeable difference in the data at different irradiation temperatures. Three dotted lines were plotted to show the trends. It is easy to find that the calculated results are reasonably consistent with the existing data. At 300℃, $\Delta\sigma_Y$ increases with increasing dpa and saturates at around 20 dpa. At 400℃, $\Delta\sigma_Y$ increases with increasing dpa at a lower rate and saturates earlier ($\sim$10 dpa). At 500℃, $\Delta\sigma_Y$ shows slightly increase and saturates around 3 dpa. In Fig. 5.16, the dose of all the proton data is the same (7 dpa) as that of the present work. For the neutron data, only these in the range of 9–12 dpa were plotted in order to make the data more comparable. For the neutron data below 450℃, $\Delta\sigma_Y$ decreases with increasing temperature, and above 500℃, $\Delta\sigma_Y \sim 0$. The trend is shown in the dotted green line. The ion irradiation data connected by dotted grey and dotted orange lines turn out to be of the similar shape. This manifests that the ion data has similar temperature dependence as the neutron data. It is also noticed that the ion data was shifted upwards from the neutron data by approximately 100–150 MPa, indicating that more pronounced hardening is expected for ion irradiations. Considering that the dose for the neutron data (9–12 dpa) is higher than that of the ion data (7 dpa), the upward shift in $\Delta\sigma_Y$ of the ion data becomes more compelling. One possible reason for the upward shift is related to the thermal annealing effect accompanying low dose rate neutron irradiations. Since the dose rate of ion irradiation is 10^3 to 10^4 higher than that of neutron irradiation, the material under ion irradiation experiences much less thermal

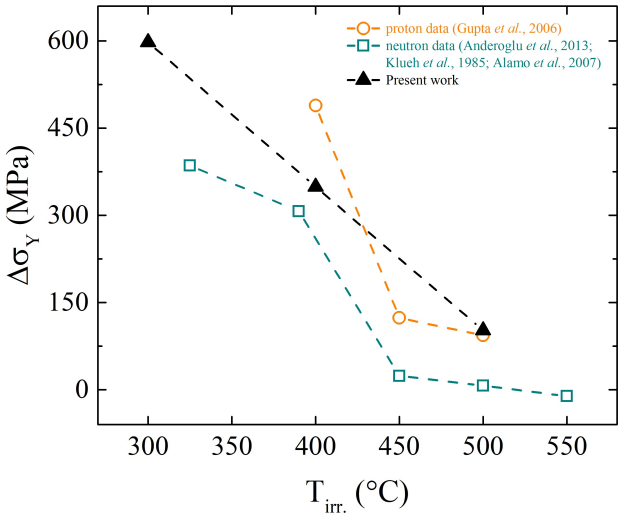

Figure 5.16: Change in yield strength $\Delta\sigma_Y$ as a function of irradiation temperature. The doses for all the proton data [82] and present work is 7 dpa, and all the neutron data [17, 103, 104] are in the range of 9–12 dpa. The dotted lines are for visual aide only.

annealing and therefore the defects (both grow-in dislocations and irradiation-induced defects) have much smaller chance to be annealed and the surviving defects are responsible for more noticeable hardening. On the other hand, the offset also indicates that the microstructure is generally similar, except for differences in the defect densityand size. For cases in which ion irradiations cannot produce the comparable microstructure as that of neutron irradiations, the ion-to-neutron is much more challenging. An example is that for Fe–Cr alloys above the α–α' phase separation threshold value, α' precipitates are only frequently observed in neutron-irradiated, rather than ion-irradiated specimens.

5.3.2 Nanoindentation measurement of irradiation hardening

Since the TEM specimens for *in situ* thin foil irradiation are too thin for nanoindentation, another set of separate bulk irradiation experiments for T91 and G92 were performed using the Van de Graaff accelerator at UIUC, as listed in Table 3.2. All the nanoindentation on irradiated T91 and G92 were done at UC Berkeley using either quasi-static or continuous stiffness measurement mode. The hardness values of similar indentation depth (93–100 nm) were chosen for the qualitative comparison.

Fig. 5.17 shows the hadness values of T91 and G92 in both unirradiated and irradiation conditions. The hardness of unirradiated T91 is 3.96±0.39 GPa,

very similar to that of G92, 3.94±0.24 GPa. For 400℃ irradiation at 3 dpa, the hadness of T91 is higher than G92, and for 500℃ irradiation at 3 dpa, the hardness values of T91 and G92 are similar and both higher than unirradiated values. Overall, The irradiation hardening of G92 is similar to (sometimes slightly less than) T91.For T91, the significant increase in hardness at 400℃ and moderate increase at 500℃ agrees with microstructure-based calcluations in previous section.

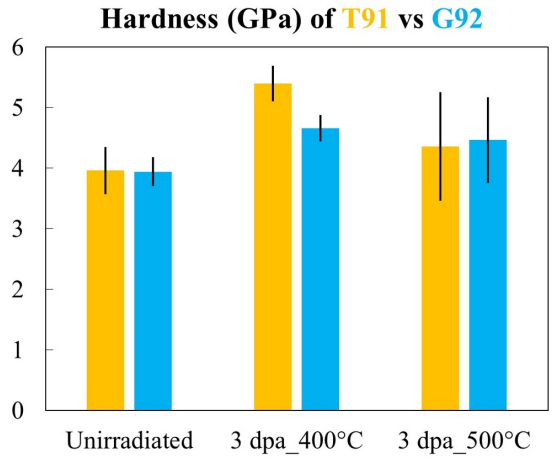

Figure 5.17: Comparison of the hardness of T91 with that of G92 at different irradiation conditions.

Fig. 5.18 shows the temperature dependence of hardening in G92 irradiated to 15 dpa. As can be seen, the hardness decreases significantly as temperature increases from 300℃ to 500℃. This is consistent with the irradiation hardening behavior of many F/M steels shown by previous studies [17].

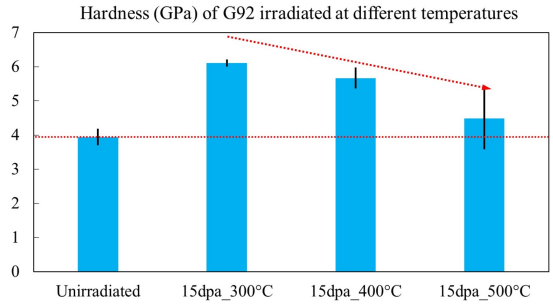

Figure 5.18: Temperature dependence of irradiation hardening in G92 irradiated to 15 dpa.

Fig. 5.19 shows the dose dependence of hardening in G92 at both 400℃

and 500℃. It was found that the irradiation hardening increases with increasing dose at 400℃, and is insensitive to dose at 500℃. Recall that for neutron irradiation in F/M steels shown in Fig. 2.8, almost no hardening was observed at 500℃ and above, implying negligible dose dependence. This agrees with our nanoindentation measurements.

In summary, the trends (both temperature dependence and dose dependence) shown by nanoindentation measurements on bulk ion-irradiated T91 and G92 are consistent with the typical hardening behavior of neutron-irradiated F/M steels. It should also be noted that our nanoindentation results can only be used as qualitative analysis, since the results suffer from size effect, substrate effect, and non-uniform dose profile over a few hundred nanometers.

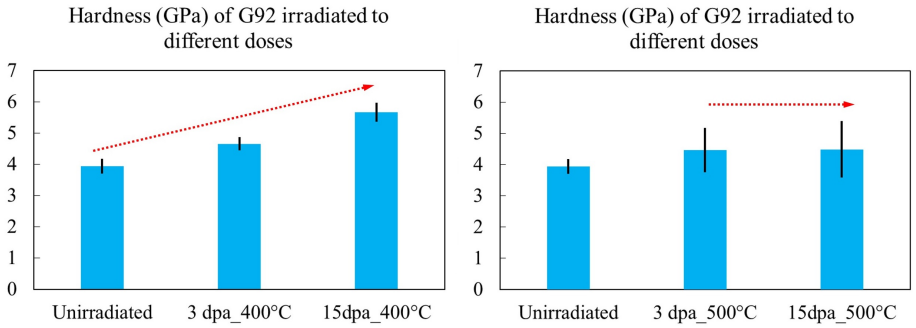

Figure 5.19: Temperature dependence of irradiation hardening in G92 irradiated to 15 dpa.

6. COMPARISON OF THIN FOIL IRRADIATION AND BULK IRRADIATION AT ELEVATED TEMPERATURES

Since both *in situ* thin foil irradiation and *ex situ* bulk irradiation were employed in this study, it is helpful to understand the complications involved in thin foil irradiation and under what conditions thin foil irradiations are expected to produce similar results to bulk irradiations.

One of the most important differences between thin foil irradiation and bulk irradiation is the difference in thickness. A TEM thin foil is typically ∼100 nm thick. For heavy ion irradiation, almost all heavy ions can penetrate through the specimen and create displacement damage inside the specimen without altering the chemical composition. This is clearly an advantage compared to bulk irradiation that injects heavy ions inside the specimen and causes defect imbalance near the tail. However, the influence of injected ions for bulk irradiations can be diminished by choosing proper depth region. A straightforward way is to avoid the implanted region and focus on the region about 1/3 to 1/2 of the peak damage depth.

A more important consequence of thin specimen is that the two free surfaces become closer with decreasing thickness. At ∼100 nm thickness, the number of atoms across the two free surfaces are only on the order of 300 to 1000. The free surfaces can have significant effects on the defect production and microstructural evolution.

The surface effects chould be less important for materials with high-density internal sinks such as martensitic steels that have high-density dislocations and ODS steels that have high-density ultra-fine nanoclusters. However, for materials with low sink density, such as austenitic stainless steel A709, the two free surfaces becomes more important, as they can act as strong sinks and alter the defect evolution, especially at elevated temperatures.

6.1 Surface effects on loop size and density in austenitic steel A709

In order to quantitatively study the surface effects, we need to think in details about the actual setup of thin foil irradiation experiments. Recall that

the specimens used for thin foil irradiations are TEM specimens prepared by jet-polishing, they are wedge-shaped with varying thicknesses. Near the edge of the perforation the thickness is typically only several nanometers, and the thickness increases with increasing distance to the edge. The thickness fringe measurements show that apart from the near-edge region, the thickness of jet-polished TEM specimens basically increases linearly with increasing distance to the perforation edge.

It is reasonable to expect that in the very thin (10s nm) region the surfaces effects becomes dominant, and in very thick (100s nm) regions surface effects become much less important. The microstructure evolution will therefore show thickness-dependent characteristics.

As an example, Fig. 6.1 shows several TEM BF images taken at regions of different thicknesses in the same grain in a A709 TEM specimen *in situ* irradiated to 1 dpa at 400℃. It is obvious that from Fig.6.1 (a) to (d), the the loop size and loop density both increased with increasing thickness (or distance to the edge). Impacts due to other factors such as differences in irradiation temperature, grain orientation, and diffraction condition, are excluded and the observed thickness-dependent loop size and density is due to the surface effect.

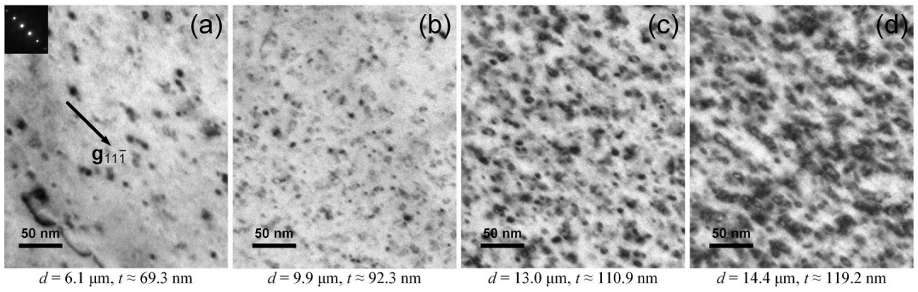

Figure 6.1: Thickness dependent loop distribution in A709 thin foil irradiated by 1.0 MeV Kr^{++} ions to 1 dpa at 400℃. Images were taken inside the same grain at (a) $d = 6.1$ μm, (b) $d = 9.9$ μm, (c) $d = 13.0$ μm, and (d) $d = 14.4$ μm, where d is the distance to the edge of perforation.

The quantitative results on the differences in the loop size are shown in Fig. 6.2. As can be seen, The loop are black-dots loop size remains less than 4 nm if the distance is less than ∼10 μm, larger loops ($>$ 6 nm) were only observed in distant (thicker) regions.

Fig. 6.3 shows the measured loop area density at different distances. Again, the loop density also shows distance-dependent characterisitics. For distances $\geqslant$ 10 μm, the loop area density increases linearly with increasing distance. The linearity fails at small distances, and the measured loop density at distances $\leqslant$ 6 μm is less than that projected by the linear dashed line. This shows that the surface effects can lead to reduced loop density.

The effect of the two free surfaces on the loop size becomes more apparent at higher dose. Fig. 6.4 shows BF images of loops in A709 irradiated to 3 dpa at

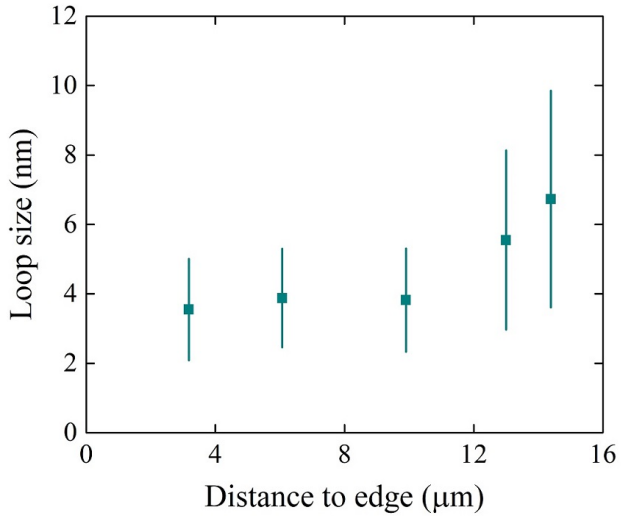

Figure 6.2: Loop size as a function of distance to edge in A709 thin foil irradiated to 1 dpa at 400°C.

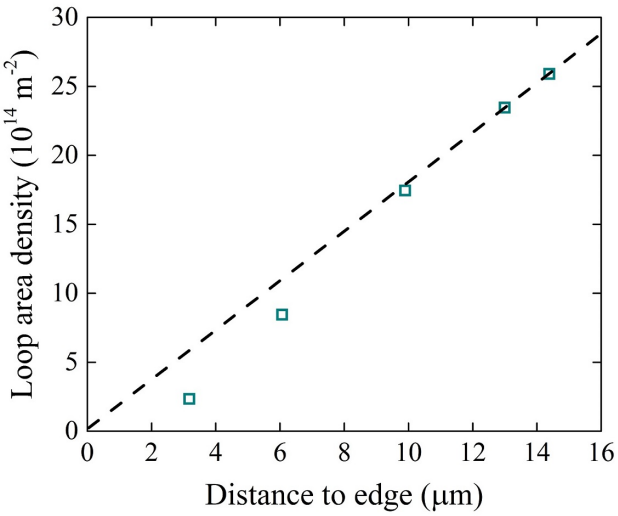

Figure 6.3: Loop area density as a function of distance to edge in A709 thin foil irradiated to 1 dpa at 400°C. The open squares are measured values and the dashed line is the linear fit of data in distant region.

400℃. The loops at thick region in Fig. 6.4 (c) are apparently much larger than the loops in thin region 6.4 (a). Moreover, edge-on Frank loops are dominant in the thick region Fig. 6.4 (c) but are absent in the thin region 6.4 (a). This could be an indication that the surfaces also have impacts on the loop character.

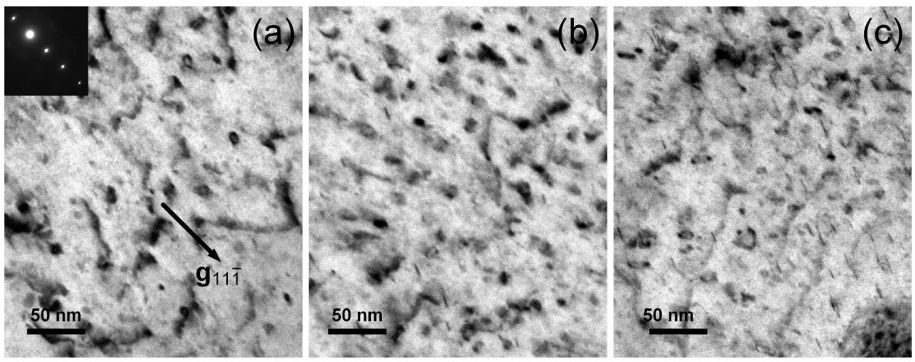

Figure 6.4: Thickness dependent loop distribution in A709 thin foil irradiated by 1.0 MeV Kr^{++} ions to 1 dpa at 400℃. Images were taken inside the same grain at (a) $d = 6.1$ μm, (b) $d = 8.4$ μm, (c) $d = 9.9$ μm.

Now, using the distance-thickness relation meausred by thickness fringes, we are ready to plot the average loop size at different thicknesses. The result is shown in Fig. 6.5. Only two data points were obtained for 3 dpa, since the contrast in thick regions was not ideal. The results clearly shows the thickness-dependence of the loop size.

The loop densities at different thicknesses are shown in Fig. 6.6. The differences in loop density at different thicknesses are more significant: the loop density in the thick reigon can be as much as 4 times the density in the thin region. It is also observed that at 400℃, the loop density seems saturated for thicknesses greater than 100 nm, which indicates that the surface effects is insignificant in the thick region.

The surface effects on the loop size and density is illustrated in Fig. 6.7. At thin regions near the perforation edge, surface effects become dominant and the loop size and density is strongly impacted. Very thick regions suffer little from surface effects but they are not suitable for TEM observations. Only at proper thick region, the surface effects are relatively insignificant and TEM characterization is still doable. This region is termed quasi-bulk region that is expected to produce similar defect structure as bulk irradiation.

However, it should be noted that for low sink density materials, the surface effects become more obvious with increasing irradiation temperature. For high temperature irradiation, such quasi-bulk region may not exist. In other words, the thick region that surface effects are negligible can be too thick for TEM observations.

In addition to the mentioned impacts on the loop size and density, it should

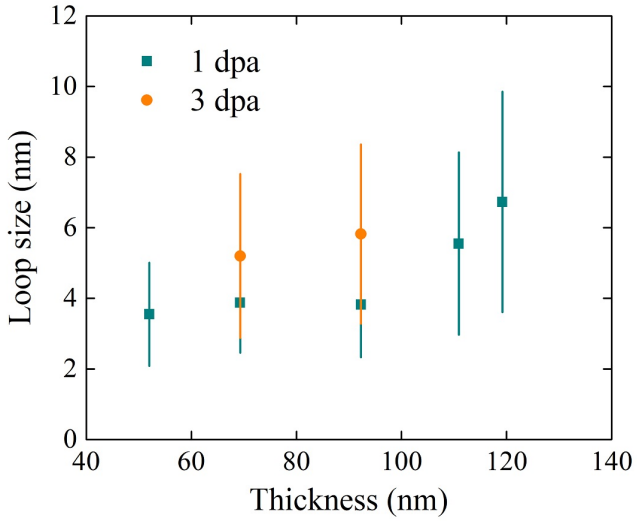

Figure 6.5: Loop size distribution as a function of thickness in A709 thin foil irradiated at 400℃.

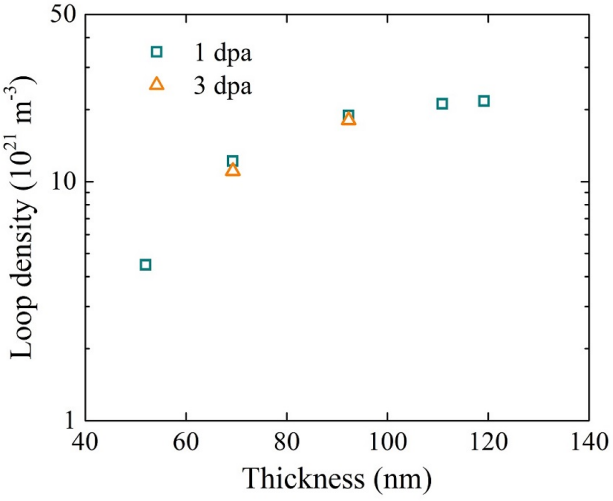

Figure 6.6: Loop density as a function of thickness in A709 thin foil irradiated at 400℃.

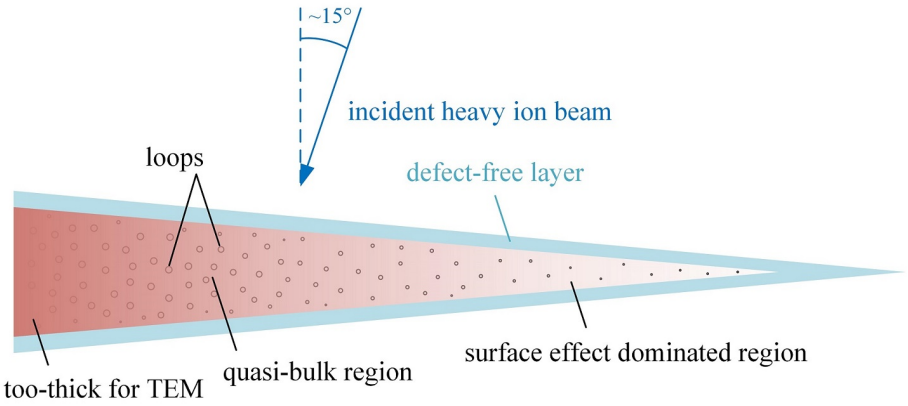

Figure 6.7: Illustration of the surface effects of thin foil irradiation.

be noted that a defect-free layer may also present for thin foil irradiation. This layer can be formed due to oxidation, sputtering, preferential precipitation at near surface regions, etc. A previous study [95] showed that the thickness of the defect-free layer is ∼20 nm for a Fe–12Ni–18Cr model alloy irradiated at 450℃.

6.2 Surface effects on loop character in austenitic steel A709

Besides surface effects on the loop size and density, thin foil irradiation can differ from bulk irradiation in other aspects. With only hundreds of atoms across the entire thickness, it is likely that under energetic ion bombardment, significant amount of stress can build up inside the TEM specimen. For instance, sample bending is frequently observed in many *in situ* irradiation experiments. Moreover, the image force exerted by the free surfaces also impacts the stress state inside the TEM specimen. It is not difficult to imagine that the local stress state can impact the defect structure. For Frank faulted loops in FCC materials such as A709, enough stress can lead to loop unfaulting or loop reorientation to accomodate local stresses.

As an example, Fig. 6.8 shows different defect structures at different thickness regions in the same grain in A709 irradiated to 3 dpa at 600℃. Figs. 6.8 (a)–(c) are taken with $\mathbf{g}_{200}$ strongly excited, and Figs. 6.8 (d)–(f) are taken with $\mathbf{g}_{\bar{1}\bar{1}1}$ strongly excited.

It is obvious that many different types of loops are present in the same grain. Loops marked by 'b' and 'e' show fault contrast (the fault contrast of 'e' loops is shown later), and loops marked by 'a', 'c', and 'd' have no stacking fault constrast. In the following analysis only two types of Burgers vector and three types of habit planes are considered: $1/3\langle 111\rangle$ and $1/2\langle 110\rangle$ Burgers vectors, $\{111\}$, $\{110\}$, and $\{100\}$ habit planes.

It is easy to identify 'e' loops as Frank faulted loops, as they are near edge-on, are perpendicular to $\mathbf{g}_{\bar{1}\bar{1}1}$ or $\mathbf{g}_{1\bar{1}1}$, and are present under both diffraction conditions.

'a' loops disappear under $\mathbf{g}_{200}$ and appear under $\mathbf{g}_{\bar{1}\bar{1}1}$, indicating that their Burgers vector is $1/2[011]$ or $1/2[0\bar{1}1]$. Note that 'a' loops are parallel to $\mathbf{g}_{200}$. Using the projection method in Fig. 3.5, it is easy to see that the habit plane of 'a' loops is $(0\bar{1}1)$ plane. Therefore, 'a' loops are $1/2\langle 110\rangle\{110\}$ perfect loops.

'b' loops show stacking fault contrast, indicating that they are $1/3\langle 111\rangle$ loops. The fact that they show up in both diffraction conditions is also consistent with $1/3\langle 111\rangle$ Burgers vectors. According to the projected shape illustrated in Fig. 3.5, the habit plane of 'b' loops is [110] or $[\bar{1}01]$ plane. Therefore, 'b' loops are $1/3\langle 111\rangle\{110\}$ faulted loops.

'c' loops disappear under $\mathbf{g}_{200}$ and appear under $\mathbf{g}_{\bar{1}\bar{1}1}$, Only $1/2[011]$ or $1/2[0\bar{1}1]$ Burgers vectors satisfy $\mathbf{g}_{200}\cdot\mathbf{b}=0$ and $\mathbf{g}_{\bar{1}\bar{1}1}\cdot\mathbf{b}\neq 0$. Therefore, the Burgers vector of 'c' loops is $1/2[011]$ or $1/2[0\bar{1}1]$, which is also consistent that 'c' loops show no fault contrast. Note that the longest side of'c' loops is parallel to $\mathbf{g}_{200}$ and 'c' loops are not near edge-on. Comparing with the illustrations shown in Figs. 3.4–3.6, the habit plane of 'c' loops should be (001) or (010) plane. Therefore, 'c' loops are $1/2\langle 110\rangle\{100\}$ perfect loops.

The Burgers vector of 'd' loops can not be directly determined using $\mathbf{g}\cdot\mathbf{b}$ criteria, since 'd' loops show up under both diffraction conditions. However, the fact that 'd' loops show no fault contrast indicates that the Burgers vector of 'd' loops is of $1/2\langle 110\rangle$ type. Now using $\mathbf{g}\cdot\mathbf{b}$ criteria it is easy to determine that the Burgers vector is $1/2[101]$ or $1/2[10\bar{1}]$. To determine the habit plane of 'd' loops, note that their longest side is parallel to $\mathbf{g}_{1\bar{1}1}$ and they are not edge-on. Comparing with Figs. 3.4–3.6, the habit plane of 'd' loops should be (110) or $(\bar{1}01)$ plane. Therefore, 'd' loops are $1/2\langle 110\rangle\{110\}$ perfect loops.

'f' loops appear under $\mathbf{g}_{200}$ and disappear under $\mathbf{g}_{\bar{1}\bar{1}1}$. The Burgers vector that satisfies $\mathbf{g}_{200}\cdot\mathbf{b}\neq 0$ and $\mathbf{g}_{\bar{1}\bar{1}1}\cdot\mathbf{b}=0$ is $1/2[1\bar{1}0]$. 'f' loops show no fault contrast, which is also consistent with $1/2[1\bar{1}0]$ Burgers vector. To determine the habit plane, note that the longest side of 'f' loops is perpendicular to $\mathbf{g}_{200}$, which indicates that the habit plane is $(\bar{1}11)$ or (111), based on the illustration shown in Fig. 3.4. Therefore, 'f' loops are $1/2\langle 110\rangle\{111\}$ perfect loops.

The fault contrast of 'g' loops can be an indication that their Burgers vector is of $1/3\langle 111\rangle$ type. The character of 'g' loops is not determined, since the shape of 'g' loops does not match anyone in Figs. 3.4–3.6. There can be two possible reasons: one reason is that 'g' loops are in the intermediate state of loop transition and their habit plane is not {111}, {110}, or {100} planes, and the other reason that they are precipitates rather than loops.

Comparing the three different thickness regions in Fig. 6.8, it is easy to see that 'b', 'c', and 'g' loops occur primarily in the region I (thinnest region), 'a' loops are mostly found in region II, 'd' loops occur mostly in regions II and III, 'f' loops are primarily found in region III.

In Fig. 6.8, only several Frank faulted loops, or 'e' loops, are found: one in region I, one in region II, and two in region III. The thickness dependence is not clear due to the low Frank loop count. Considering that the thickness of

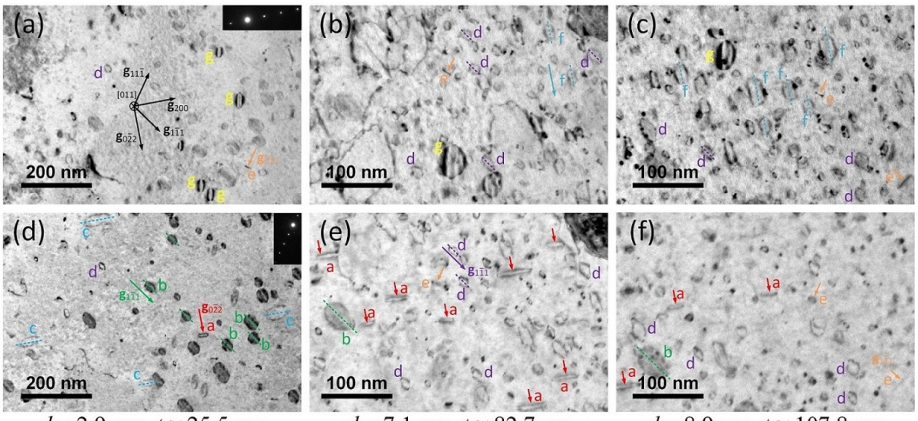

Figure 6.8: Different defect structures at different thickness regions in the same grain in A709 irradiated to 3 dpa at 600℃. All images are taken near [011] zone. (a)–(c) are taken with $\mathbf{g}_{200}$ strongly excited, and (d)–(f) are taken with $\mathbf{g}_{\bar{1}\bar{1}1}$ strongly excited. (a) and (d) are the same region (region I) with distance to edge $d = 2.9$ μm, (b) and (e) are the same region (region II) with $d = 7.1$ μm, (c) and (f) are the same region (region III) with $d = 8.9$ μm.

region III is only 107.8 nm, it may be helpful to examine even thicker regions. Fig. 6.9 shows the loops in a much more distant region ($d = 17.1$ μm) with corresponding thickness of about 221 nm. This region is still within the same grain as the regions shown in Fig. 6.8. It now becomes clear that Frank faulted loops marked by 'e' occurs mostly in very thick regions. In Fig. 6.9, several 'f' loops were also found, and no 'a', 'b', or 'c' loops were found.

In summary, for A709 thin foil irradiation at 600℃, Detailed TEM analysis shows the loop character strongly depends on the thickness of the corresponding region. Lots of loops other than Frank faulted loops were found in the irradiated TEM specimen. In total, $1/2\langle 110\rangle\{110\}$ perfect loops, $1/3\langle 111\rangle\{110\}$ faulted loops, $1/2\langle 110\rangle\{100\}$ perfect loops, $1/2\langle 110\rangle\{111\}$ perfect loops, and $1/3\langle 111\rangle\{111\}$ Frank faulted loops were found. 'a' loops (or $1/2\langle 110\rangle\{110\}$ perfect loops), 'b' loops (or $1/3\langle 111\rangle\{110\}$ faulted loops), and 'c' loops (or $1/2\langle 110\rangle\{100\}$ perfect loops) were only found in thin regions, and Frank faulted loops marked by 'e' were mostly found in very thick regions. These results show that the surface effects can have huge impacts on the loop character. The underlying reason could be due to the buildup of local stresses during thin foil irradiation. The higher stresses in the thin region leads to earlier loop unfaulting (change in Burgers vector) or loop reorientation (change in habit plane) to accomodate the local stresses.

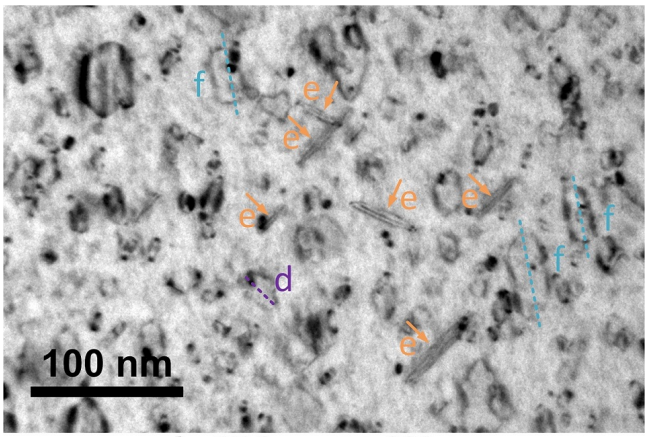

Figure 6.9: Frank faulted loops in a thick region in A709 irradiated to 3 dpa at 600℃. The corresponding distance to edge is 17.1 μm, and the thickness is 221 nm.

6.3 Comparison of thin foil irradiation with bulk irradiation

Now we know that the surface effects can have impacts on the loop size, loop density, and also loop character. The effects on the loop size and density is due to the fact that the two nearby free surfaces can act as strong sinks for radiation-induced defects. We term this as sink effect. The effects on the loop character is likely due to the buildup of local stresses since the foil is thin and there is no direct mechanical suppot in the thin region. We term this as stress effect. With so many differences, one may wonder can thin foil irradiation still be used as a surrogate of bulk irradiation? Under what conditions can thin foil irradiation produce quantitatively similar defects as bulk irradiation?

The complete answer to this is very complex, and beyond the scope of this work. However, it is possible to provide some sketchy answers.

Firstly, the sink effect becomes less important for materials with high-density internal sinks. Examples are F/M alloys, ODS alloys, CW alloys, nanocrystalline materials, etc. With enough internal sinks, the radiation-induced point defects or mobile defect clusters will be mostly trapped by the internal sinks, even if the temperature is high enough to allow them to migrate to the free surfaces. As shown in a recent study [105], simple rate thory estimation shows that high density ($\sim 10^{14}$ m^{-2}) dislocations or high density ($\sim 10^{23}$ m^{-3}) nanoparticles ($r \approx 2$ nm) can lower the point defect concentration by 1–2 orders of magnitude, in other words most of the point defects can be absorbed by the internal sinks.

Secondly, the stress effect becomes less important for high strength materials such as F/M alloys and ODS alloys. The high strength provides structural stability under thin foil irradiation. The high-density dislocations can also accomodate the local stress through dislocation movement and interactions.

Lastly, for materials with low-density internal sinks, such as SA austenitic alloys, the sink effect is less important at low temperatures. For example, the size of Frank loops observed in the thick region in A709 thin foil irradiated to 3 dpa at 400℃ (shown in Fig. 6.4) is close to the Frank loops found in bulk irradiated to 10 peak dpa (4.24 dpa for 200–400 nm depth region) at 400℃ (shown in Fig. 4.6).

For A709, we already know that lots of loops other than Frank loops are produced at high temperatures (e.g. 600℃), one may wonder if we only compare the Frank loops, is thin foil irradiation still different from bulk irradiation?

To answer this, systematic comparison on the Frank loop size and density is required. Fig. 6.10 shows the sizes of the Frank loops in thin foil irradiated A709 with those in bulk irradiated A709. For thin foil irradiation, the comparison only considered Frank loops in the thick region. For bulk irradiation, the comparison only included Frank loops in the 10 peak dpa specimens in the 200–400 nm depth region (corrsponding dose is 4.24 dpa). The results clearly shows that thin foil irradiation can produce similar sized Frank loops as bulk irradiation for all three temperatures.

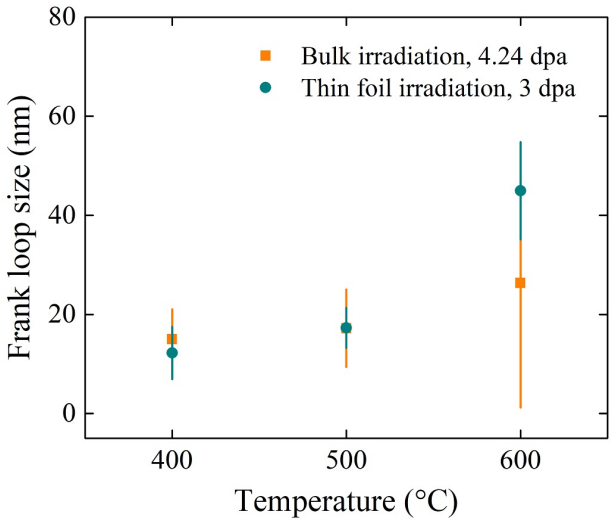

Figure 6.10: Frank loop sizes in thin foil irradiated vs bulk irradiated A709. The data for thin foil irradiation are from the thick regions, and the data for bulk irradiation are from the 200–400 nm depth region.

The comparion on the Frank loop density of thin foil irradiation with that of bulk irradiation is shown in Fig. 6.11. All the densities are 4 times the measured

Frank loop densities (only counting one {111} variant). It can be seen that the density of Frank loops is comparable for both types of irradiation at 400℃. However, the Frank loop density of thin foil irradiation becomes less than that of bulk irradiation with increasing irradiation temperture. At 600℃, the Frank loop density of thin foil irradiation is about 1/3 of that of bulk irradiation.

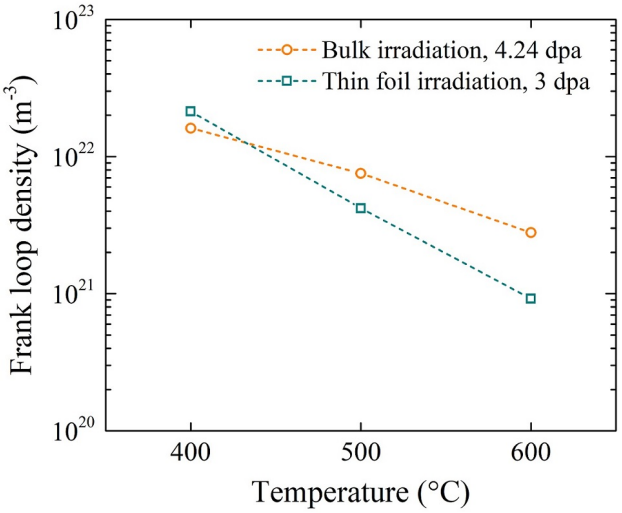

Figure 6.11: Frank loop densities in thin foil irradiated vs bulk irradiated A709. The data for thin foil irradiation are from the thick regions, and the data for bulk irradiation are from the 200–400 nm depth region.

Combine the results on the Frank loop size and density, it seems that the Frank loop size is not impacted by the surface effects, and the Frank loop density is strongly impacted. The Frank loop density of thin foil irradiation and that of bulk irradiation are still similar at 400℃. Therefore, for A709, when the irradiation temperature is $\leqslant$ 400℃, thin foil irradiation is basically equivalent to bulk irradiation, provided that the TEM analysis is focused on the thick region for thin foil irradiation. This also justifies our use of *in situ* thin foil irradiation results for A709 irradiated at 300℃ (Fig. 4.5).

7. CONCLUSIONS AND RECOMMENDATIONS

In this report, the radiation response of several different advanced alloy systems were investigated. State-of-the-art characterization techniques including TEM, SEM-EBSD, APT, STEM-EDS, and nanoindentation were used to systematically study the radiation effects in austenitic alloy A709 and 316H, ferritic/martensitic alloys T91 and G92. *Ex situ* bulk ion irradiation, *in situ* TEM thin foil irradiation, and neutron irradiation were employed. The study on A709 covers both bulk ion irradiation and thin foil ion irradiaiton, the microstructural results on T91 are from thin foil irradiation and the nanoindentation results are from bulk irradiation.

7.1 Radiation-induced microstructural and mechanical property modifications in austenitic alloy A709

For A709 bulk irradiation at 300–600℃ up to 150 peak dpa, a series of radiation-induced microstructural and mechanical property modifications were observed and discussed in detail:

1. The radiation-induced Frank faulted loops in A709 irradiated at 400℃ and above were systematically characterized using WBDF and rel-rod DF imaging techniques. Compared to neuton-irradiated stainless steel 316, ion-irradiated A709 show similar Frank loop density at 400℃. However, the Frank loop density at 500 and 600℃ is much higher.

2. Radiation-induced segregation of Ni and Si was observed in every irradiation condition. RIS of Ni and Si was found at various sinks: line dislocations, dislocation loops, surfaces of voids, and particle-matrix interfaces.

3. Radiation-induced Ni,Si-rich precipitates were observed. They are only enriched in Ni and Si, and depleted in other elements. These Ni,Si-rich precipitates are very similar to Ni_3Si precipitates in neutron-irradiated austenitic stainless steel 316 reported in previous studies. However, they show no extra spots in the diffraction pattern. The reason could be that the cascade damage of high dose rate ion irradiation leads to distorted crystal structure of the Ni,Si-rich precipitates.

4. Radiation-modified Cr-rich carbides were found in the highest dose (150 peak dpa) samples for both 500 and 600℃ irradiation. Several different types of carbides were found: $M_{23}C_6$ phase at 500℃, and M_6C and $(\mathbf{Cr},Mo)_2(\mathbf{C},N)$ phases at 600℃.

5. Radiation-induced change in the orientation relationship of pre-existing MX precipitates was observed in A709 irradiated to 50 peak dpa at 600℃. The MX precipitates changed from incoherent with no preferred orientation to semicoherent with a cubic-on-cubic orientation relationship.

6. Radiation-induced voids were commonly found in A709 irradiated to 50 and 150 peak dpa at 500℃. A few voids were also observed in A709 irradiated at 600℃. The voids were only found regions less than 750 nm in depth. The highest swelling for A709 irradiated at 500℃ to 50 and 150 peak dpa is about 0.44% and 0.37%, respectively. This also indicates that 150 peak dpa is still within the transient regime.

7. Nanoindentation measurements show apparent decrease in irradiation hardening with increasing temperature. For 500℃ irradiation, the hardness increased significantly at 10 peak dpa, and then increased gradually from 10 peak dpa to 150 peak dpa. For the lowest dose irradiation, microstructure-based calculations averaging over the entire irradiated region agree well with the nanoindentation measurements.

7.2 Radiation-induced microstructural and mechanical property modifications in ferritic/ martensitic alloys T91 and G92

The radiation response of F/M steel T91 and G92 was studied by *in situ* TEM heavy ion irradiation. T91 and G92 TEM thin foils were irradiated up to 7 dpa at 300, 400, and 500℃. A set of bulk irradiations were also carried out for nanoindention measurements. Following conclusions can be drawn:

1. The microstructure evolution of T91 and G92 under *in situ* irradiation is found sensitive to the irradiation temperature: at lower temperature (300℃), black-dot dislocation loops and network dislocations were observed; at higher temperature (500℃), only aligned extended loops were observed.

2. Post-irradiation examination show that the loops are dominantly $a_0/2\langle 111\rangle$ type at 500℃. The loops at 400℃ are mixture of $a_0/2\langle 111\rangle$ and $a_0\langle 100\rangle$ loops. This is consistent with previously observed loop transition in Fe–Cr model alloys.

3. The loop size and density, and dislocation density data were used to estimate the change in yield strength using the dispersed barrier hardening

model. It was found that as temperature increases, the major contributor to irradiation hardening changed from network dislocations to dislocation loops. The calculated $\Delta\sigma_Y$ is higher than that of neutron data in literature.

4. Nanoindentation measurements on bulk-irradiated spcimens show that T91 and G92 have similar hardening behavior. The temperature dependence and dose dependence of nanoindentation hardness data are consistent with the typical hardening behavior of neutron-irradiated F/M steels.

7.3 Recommendations for future irradiation studies of A709

Alloy A709 has potential advantages over 316-type stainless steels for mechanical properties and corrosion resistance for elevated temperature application in sodium cooled fast reactor applications. It is likely to be more resilient at target operation temperatures of 550℃ than the austenitic steels which have lower Cr and Ni content. Efforts to develop a significant data base to qualify A709 for structural applications in future SFR applications are supported by the results of this study.

A709 does undergo significant precipitation and second phase development processes during thermal aging above 500℃, which have been thoroughly studied and characterized in alloy systems with comparable compositions to A709 in this study. These thermal aging conditions may extend to SFR reactor structural applications in the temperature range of interest for a proposed 60 year design life and can be largely studied through long-term thermal aging and ambient stress creep studies.

The results of the current study show that there are significant irradiation-induced microstructural changes at temperatures between 300 and 600℃ which could significantly influence the alloy performance in service. These include: Frank loop formation and resulting hardening, major precipitation effects (e.g. matrix $M_{23}C_6$), major alloying element segregation effects (e.g. Ni-Si cosegregation to multiple defect sinks like dislocations, loops and precipitates) and void swelling. It is well established that, due to the higher dose rates in heavy ion irradiation studies, the rates (i.e. the dose) at which some of these effects form can be both accelerated (i.e. form at lower doses) and can shift in temperature (typically to higher temperatures).

Future neutron irradiation campaigns on this alloy should concentrate on these radiation-induced changes over a similar temperature range examined here: 300 to 600℃, to doses up to and beyond the 10 or 20 dpa anticipated for the total reactor life of the structural material applications. It is significant that the evolution of nearly all of the irradiation-induced microstructural changes occur quickly, even at low doses. Only the observed void swelling takes significant dose at a sufficiently high irradiation temperature to occur. The

observed microstructural changes will affect mechanical properties and also potentially affect sodium corrosion resistance, so future neutron irradiation should include reasonable scale tensile, fracture toughness and irradiation creep tests, to characterize potential changes (degradation) in materials structural properties. Comparisons to the significant data and literature on neutron irradiated 316-type stainless steels could confirm the superiority of A709 for SFR long-term structural applications.

7.4 Recommendations for future irradiation studies of G92

Ferritic/martensitic alloy G92 in the optimized heat-treatment condition was shown to have similar, but somewhat better irradiation-resistance properties compared to T91 in this study. It appears that the compositional control and heat treatment improvements make G92 better qualified for elevated temperature application in sodium cooled fast reactor applications than other current versions of the Fe–9Cr class of alloys. This should be confirmed by a future neutron irradiation campaign on this alloy.

G92 shows similar development of dislocation black dot and dislocation networks at lower irradiation temperatures (300℃) and dislocation loop structures at higher temperatures (400 and 500℃) as other similar alloy compositions. The dislocation loop structure also changes with temperature, a mixture of ⟨111⟩-type and ⟨100⟩-type are found at 400℃, while ⟨100⟩-type predominate at 500℃, also consistent with studies on other Fe–9Cr-class alloys. The major irradiation related issue with this alloy class is predominately lower temperature loss of ductility.

Future neutron irradiation campaigns on this alloy should concentrate on these radiation-induced changes over a similar temperature range examined here: 300 to 600℃, to doses up to and beyond the 10 or 20 dpa anticipated for the total reactor life of the structural material applications. Future neutron irradiation should include reasonable scale tensile, fracture toughness, Charpy and irradiation creep tests, to characterize potential changes (degradation) in materials structural properties. An emphasis should be placed on characterize lower temperature ductility loss due to irradiation exposure.

REFERENCES

[1] G. S. WAS, Fundamentals of Radiation Materials Science, Springer New York, 2017. doi:10.1007/978-1-4939-3438-6.

[2] S. J. Zinkle, J. T. Busby, Structural materials for fission & fusion energy, Materials Today 12 (11) (2009) 12–19. doi:10.1016/s1369-7021(09)70294-9.

[3] S. Zinkle, G. Was, Materials challenges in nuclear energy, Acta Materialia 61 (3) (2013) 735–758. doi:10.1016/j.actamat.2012.11.004.

[4] P. Maziasz, Overview of microstructural evolution in neutron-irradiated austenitic stainless steels, Journal of Nuclear Materials 205 (1993) 118–145. doi:10.1016/0022-3115(93)90077-c.

[5] F. Garner, M. Toloczko, B. Sencer, Comparison of swelling and irradiation creep behavior of fcc-austenitic and bcc-ferritic/martensitic alloys at high neutron exposure, Journal of Nuclear Materials 276 (1–3) (2000) 123–142. doi:10.1016/s0022-3115(99)00225-1.

[6] C. Cawthorne, C. Brown, The occurrence of an ordered FCC phase in neutron irradiated M316 stainless steel, Journal of Nuclear Materials 66 (1–2) (1977) 201–202. doi:10.1016/0022-3115(77)90149-0.

[7] H. Brager, F. Garner, Swelling as a consequence of gamma prime (γ') and $M_{23}(C, Si)_6$ formation in neutron irradiated 316 stainless steel, Journal of Nuclear Materials 73 (1) (1978) 9–19. doi:10.1016/0022-3115(78)90474-9.

[8] P. Maziasz, Formation and stability of radiation-induced phases in neutron-irradiated austenitic and ferritic steels, Journal of Nuclear Materials 169 (1989) 95–115. doi:10.1016/0022-3115(89)90525-4.

[9] D. Edwards, E. Simonen, F. Garner, L. Greenwood, B. Oliver, S. Bruemmer, Influence of irradiation temperature and dose gradients on the microstructural evolution in neutron-irradiated 316SS, Journal of Nuclear Materials 317 (1) (2003) 32–45. doi:10.1016/s0022-3115(03)00003-5.

[10] H. Brager, F. Garner, Dependence of void formation on phase stability in neutron-irradiated type 316 stainless steel, in: Effects of Radiation on Structural Materials, ASTM International, 1979, pp. 207–232. doi:10.1520/stp38167s.

[11] P. Maziasz, J. Busby, Properties of austenitic steels for nuclear reactor applications, in: Comprehensive Nuclear Materials, Elsevier, 2012, pp. 267–283. doi:10.1016/b978-0-08-056033-5.00019-7.

[12] E. Lee, P. J. Maziasz, A. Rowcliffe, The structure and composition of phases occurring in austenitic stainless steels in thermal and irradiation environments, in: J. Holland, L. Mansur, D. Potter (Eds.), Phase Stability During Irradiation, The Metallurgical Society of AIME: New York, 1981, p. 191.

[13] W. Yang, Precipitate evolution in Type 316 stainless steels irradiated in EBR-II, in: Radiation-Induced Changes in Microstructure: 13th International Symposium (Part I), ASTM International, pp. 628–646. doi:10.1520/stp33848s.

[14] G. S. Was, P. L. Andresen, Irradiation-assisted stress-corrosion cracking in austenitic alloys, JOM 44 (4) (1992) 8–13. doi:10.1007/bf03222812.

[15] A. Jacobs, G. Wozadlo, K. Nakata, S. Kasahara, T. Okada, S. Kawano, S. Suzuki, The correlation of grain boundary composition in irradiated stainless steel with IASCC resistance, in: Proceedings of the sixth international symposium on environmental degradation of materials in nuclear power systems-water reactors, 1993.

[16] O. Chopra, A. Rao, A review of irradiation effects on LWR core internal materials – IASCC susceptibility and crack growth rates of austenitic stainless steels, Journal of Nuclear Materials 409 (3) (2011) 235–256. doi:10.1016/j.jnucmat.2010.12.001.

[17] O. Anderoglu, T. S. Byun, M. Toloczko, S. A. Maloy, Mechanical performance of ferritic martensitic steels for high dose applications in advanced nuclear reactors, Metallurgical and Materials Transactions A 44 (S1) (2012) 70–83. doi:10.1007/s11661-012-1565-y.

[18] T. Byun, K. Farrell, Irradiation hardening behavior of polycrystalline metals after low temperature irradiation, Journal of Nuclear Materials 326 (2–3) (2004) 86–96. doi:10.1016/j.jnucmat.2003.12.012.

[19] R. Klueh, A. Nelson, Ferritic/martensitic steels for next-generation reactors, Journal of Nuclear Materials 371 (1–3) (2007) 37–52. doi:10.1016/j.jnucmat.2007.05.005.

[20] A. Kohyama, A. Hishinuma, D. Gelles, R. Klueh, W. Dietz, K. Ehrlich, Low-activation ferritic and martensitic steels for fusion application, Journal of Nuclear Materials 233–237 (1996) 138–147. doi:10.1016/s0022-3115(96)00327-3.

[21] B. Raj, M. Vijayalakshmi, Ferritic steels and advanced ferritic–martensitic steels, in: Comprehensive Nuclear Materials, Elsevier, 2012, pp. 97–121. doi:10.1016/b978-0-08-056033-5.00066-5.

[22] R. L. Klueh, Elevated temperature ferritic and martensitic steels and their application to future nuclear reactors, International Materials Reviews 50 (5) (2005) 287–310. doi:10.1179/174328005x41140.

[23] B. C. Masters, Dislocation loops in irradiated iron, Philosophical Magazine 11 (113) (1965) 881–893. doi:10.1080/14786436508223952.

[24] D. Gelles, Microstructural examination of neutron-irradiated simple ferritic alloys, Journal of Nuclear Materials 108–109 (1982) 515–526. doi:10.1016/0022-3115(82)90523-2.

[25] A. Okada, T. Yasujima, T. Yoshiie, I. Ishida, M. Kiritani, Mechanical property changes and microstructures of iron irradiated with fission and fusion neutrons, Journal of Nuclear Materials 179–181 (1991) 1083–1087. doi:10.1016/0022-3115(91)90280-k.

[26] Y. Katoh, A. Kohyama, D. S. Gelles, Swelling and dislocation evolution in simple ferritic alloys irradiated to high fluence in FFTF/MOTA, Journal of Nuclear Materials 225 (1995) 154–162. doi:10.1016/0022-3115(94)00669-5.

[27] S. Porollo, A. Dvoriashin, A. Vorobyev, Y. Konobeev, The microstructure and tensile properties of Fe–Cr alloys after neutron irradiation at 400 ℃ to 5.5–7.1 dpa, Journal of Nuclear Materials 256 (2–3) (1998) 247–253. doi:10.1016/s0022-3115(98)00043-9.

[28] Y. Konobeev, A. Dvoriashin, S. Porollo, F. Garner, Swelling and microstructure of pure Fe and Fe–Cr alloys after neutron irradiation to ∼26dpa at 400 ℃, Journal of Nuclear Materials 355 (1–3) (2006) 124–130. doi:10.1016/j.jnucmat.2006.04.011.

[29] M. Matijasevic, E. Lucon, A. Almazouzi, Behavior of ferritic/martensitic steels after n-irradiation at 200 and 300 ℃, Journal of Nuclear Materials 377 (1) (2008) 101–108. doi:10.1016/j.jnucmat.2008.02.063.

[30] M. Matijasevic, A. Almazouzi, Effect of Cr on the mechanical properties and microstructure of Fe–Cr model alloys after n-irradiation, Journal of Nuclear Materials 377 (1) (2008) 147–154. doi:10.1016/j.jnucmat.2008.02.061.

[31] M. Hernández-Mayoral, C. Heintze, E. Oñorbe, Transmission electron microscopy investigation of the microstructure of Fe–Cr alloys induced by neutron and ion irradiation at 300 ℃, Journal of Nuclear Materials 474 (2016) 88–98. doi:10.1016/j.jnucmat.2016.03.002.

[32] Z. Yao, M. Jenkins, M. Hernández-Mayoral, M. Kirk, The temperature dependence of heavy-ion damage in iron: A microstructural transition at elevated temperatures, Philosophical Magazine 90 (35–36) (2010) 4623–4634. doi:10.1080/14786430903430981.

[33] S. L. Dudarev, R. Bullough, P. M. Derlet, Effect of the α–γ phase transition on the stability of dislocation loops in bcc iron, Physical Review Letters 100 (13). doi:10.1103/physrevlett.100.135503.

[34] W.-Y. Chen, Irradiation damage in neutron-irradiated Fe–Cr model alloys, Ph.D. thesis (2014).

[35] G. Bonny, D. Terentyev, L. Malerba, On the α – α' miscibility gap of Fe–Cr alloys, Scripta Materialia 59 (11) (2008) 1193–1196. doi:10.1016/j.scriptamat.2008.08.008.

[36] G. Bonny, P. Erhart, A. Caro, R. C. Pasianot, L. Malerba, M. Caro, The influence of short range order on the thermodynamics of Fe–Cr alloys, Modelling and Simulation in Materials Science and Engineering 17 (2) (2009) 025006. doi:10.1088/0965-0393/17/2/025006.

[37] G. Bonny, D. Terentyev, L. Malerba, New contribution to the thermodynamics of Fe–Cr alloys as base for ferritic steels, Journal of Phase Equilibria and Diffusion 31 (5) (2010) 439–444. doi:10.1007/s11669-010-9782-9.

[38] V. Kuksenko, C. Pareige, C. Genevois, F. Cuvilly, M. Roussel, P. Pareige, Effect of neutron-irradiation on the microstructure of a Fe–12at.%Cr alloy, Journal of Nuclear Materials 415 (1) (2011) 61–66. doi:10.1016/j.jnucmat.2011.05.042.

[39] M. Bachhav, G. R. Odette, E. A. Marquis, α' precipitation in neutron-irradiated Fe–Cr alloys, Scripta Materialia 74 (2014) 48–51. doi:10.1016/j.scriptamat.2013.10.001.

[40] O. Tissot, C. Pareige, E. Meslin, B. Decamps, J. Henry, Kinetics of α' precipitation in an electron-irradiated Fe15Cr alloy, Scripta Materialia 122 (2016) 31–35. doi:10.1016/j.scriptamat.2016.05.021.

[41] F. Soisson, T. Jourdan, Radiation-accelerated precipitation in Fe–Cr alloys, Acta Materialia 103 (2016) 870–881. doi:10.1016/j.actamat.2015.11.001.

[42] E. R. Reese, N. Almirall, T. Yamamoto, S. Tumey, G. R. Odette, E. A. Marquis, Dose rate dependence of Cr precipitation in an ion-irradiated Fe–18Cr alloy, Scripta Materialia 146 (2018) 213–217. doi:10.1016/j.scriptamat.2017.11.040.

[43] Private communication with T.-L. (Sam) Sham, Argonne National Laboratory.

[44] Private communication with Lizhen Tan, Oak Ridge National Laboratory.

[45] S. Sham, L. Tan, Y. Yamamoto, Development of Advanced 9Cr Ferritic-Martensitic Steels and Austenitic Stainless Steels for Sodium-Cooled Fast Reactor, 2013.
URL `http://www.osti.gov/scitech/servlets/purl/1223062`

[46] L. Tan, M. A. Sokolov, T.-L. Sham, Creep Resistance and Fracture Toughness of Recently-Developed Optimized Grade 92 and Its Weldments for Advanced Fast Reactors, 2017.
URL http://www.osti.gov/scitech/servlets/purl/1376380

[47] T. Sourmail, H. K. D. H. Bhadeshia, Microstructural evolution in two variants of NF709 at 1023 and 1073 K, Metallurgical and Materials Transactions A 36 (1) (2005) 23–34. doi:10.1007/s11661-005-0135-y.

[48] B. Kim, L. Tan, C. Xu, Y. Yang, X. Zhang, M. Li, Microstructural evolution of NF709 (20Cr–25Ni–1.5MoNbTiN) under neutron irradiation, Journal of Nuclear Materials 470 (2016) 229–235. doi:10.1016/j.jnucmat.2015.12.037.

[49] D. Powell, R. Pilkington, D. Miller, The precipitation characteristics of 20% Cr/25% Ni–Nb stabilised stainless steel, Acta metallurgica 36 (3) (1988) 713–724.

[50] C. Taylor, Precipitation in 20Cr–25Ni type stainless steel irradiated at low temperatures in a thermal reactor (AGR), in: Dimensional stability and mechanical behaviour of irradiated metals and alloys. V. 1, 1983.

[51] S. Zinkle, P. Maziasz, R. Stoller, Dose dependence of the microstructural evolution in neutron-irradiated austenitic stainless steel, Journal of Nuclear Materials 206 (2–3) (1993) 266–286. doi:10.1016/0022-3115(93)90128-l.

[52] P. Maziasz, Temperature dependence of the dislocation microstructure of PCA austenitic stainless steel irradiated in ORR spectrally-tailored experiments, Journal of Nuclear Materials 191–194 (1992) 701–705. doi:10.1016/0022-3115(92)90563-z.

[53] H. Brager, J. Straalsund, Defect development in neutron irradiated type 316 stainless steel, Journal of Nuclear Materials 46 (2) (1973) 134–158. doi:10.1016/0022-3115(73)90131-1.

[54] E. Bloom, J. Stiegler, Effect of irradiation on the microstructure and creep-rupture properties of type 316 stainless steel, in: Effects of Radiation on Substructure and Mechanical Properties of Metals and Alloys, ASTM International, 1973.

[55] H. Brager, The effects of cold working and pre-irradiation heat treatment on void formation in neutron-irradiated type 316 stainless steel, Journal of Nuclear Materials 57 (1) (1975) 103–118. doi:10.1016/0022-3115(75)90184-1.

[56] H. Brager, F. Garner, G. Guthrie, The effect of stress on the microstructure of neutron irradiated type 316 stainless steel, Journal of Nuclear Materials 66 (3) (1977) 301–321. doi:10.1016/0022-3115(77)90119-2.

[57] P. Barton, B. Eyre, D. Stow, The structure of fast-reactor irradiated solution-treated AISI type 316 steel, Journal of Nuclear Materials 67 (1–2) (1977) 181–197. doi:10.1016/0022-3115(77)90173-8.

[58] P. Maziasz, Microstructures developed in austenitic stainless steels irradiated in HFIR at 552 ℃, in: Trans. Am. Nucl. Soc.; (United States), Vol. 39, 1981.

[59] M. Tanaka, S. Hamada, A. Hishinuma, P. Maziasz, Microstructural development of austenitic stainless steels irradiated in HFIR, Journal of Nuclear Materials 155–157 (1988) 801–805. doi:10.1016/0022-3115(88)90419-9.

[60] S. Hamada, M. Suzuki, P. J. Maziasz, A. Hishinuma, M. P. Tanaka, The microstructural evolution and swelling behavior of type 316 stainless steel irradiated in HFIR, in: Effects of Radiation on Materials: 14th International Symposium (Volume I), ASTM International, 1990.

[61] H. Brager, F. Garner, E. Gilbert, J. Flinn, W. Wolfer, Stress-affected microstructural development and creep-swelling interrelationship, in: Conference on radiation effects in breeder reactor structural materials, 1977.

[62] P. J. Maziasz, C. J. McHargue, Microstructural evolution in annealed austenitic steels during neutron irradiation, International Materials Reviews 32 (1) (1987) 190–219. doi:10.1179/095066087790150331.

[63] P. Maziasz, Effects of helium content of microstructural development in Type 316 stainless steel under neutron irradiation, Tech. rep. (nov 1985). doi:10.2172/6441891.

[64] H. Brager, L. Blackburn, D. Greenslade, The dependence on displacement rate of radiation-induced changes in microstructure and tensile properties of AISI 304 and 316, Journal of Nuclear Materials 122 (1–3) (1984) 332–337. doi:10.1016/0022-3115(84)90620-2.

[65] H. Kawanishi, S. Ishino, Microstructure of Fe–16Ni–15Cr alloys irradiated in JOYO, Journal of Nuclear Materials 155–157 (1988) 806–809. doi:10.1016/0022-3115(88)90420-5.

[66] H. Kawanishi, S. Ishino, Characterization of microstructure at 673 K in neutron-irradiated Fe–16Ni–15Cr with the addition of C, Ti and Nb, Journal of Nuclear Materials 179–181 (1991) 534–537. doi:10.1016/0022-3115(91)90143-u.

[67] T. Sawai, P. Maziasz, A. Hishinuma, Microstructural evolution of welded austenitic stainless steels irradiated in the spectrally-tailored ORR experiment at 400 ℃, Journal of Nuclear Materials 179–181 (1991) 519–522. doi:10.1016/0022-3115(91)90139-x.

[68] N. Yoshida, Q. Xu, H. Watanabe, T. Muroga, M. Kiritani, Low dose fission neutron irradiation on P- and Ti-modified austenitic alloys with improved temperature control, Journal of Nuclear Materials 191–194 (1992) 1114–1118. doi:10.1016/0022-3115(92)90648-5.

[69] A. Etienne, B. Radiguet, P. Pareige, J.-P. Massoud, C. Pokor, Tomographic atom probe characterization of the microstructure of a cold worked 316 austenitic stainless steel after neutron irradiation, Journal of Nuclear Materials 382 (1) (2008) 64–69. doi:10.1016/j.jnucmat.2008.09.015.

[70] J. F. Ziegler, M. Ziegler, J. Biersack, SRIM – the stopping and range of ions in matter (2010), Nuclear Instruments and Methods in Physics Research Section B: Beam Interactions with Materials and Atoms 268 (11–12) (2010) 1818–1823. doi:10.1016/j.nimb.2010.02.091.

[71] R. Stoller, M. Toloczko, G. Was, A. Certain, S. Dwaraknath, F. Garner, On the use of SRIM for computing radiation damage exposure, Nuclear Instruments and Methods in Physics Research Section B: Beam Interactions with Materials and Atoms 310 (2013) 75–80. doi:10.1016/j.nimb.2013.05.008.

[72] Standard practice for investigating the effects of neutron radiation damage using charged-particle irradiation. doi:10.1520/e0521-16.

[73] D. B. Williams, C. B. Carter, Transmission Electron Microscopy, Springer US, 2009. doi:10.1007/978-0-387-76501-3.

[74] P. B. Hirsch, A. Howie, R. Nicholson, D. Pashley, M. J. Whelan, Electron microscopy of thin crystals, Butterworth Inc., 1965.

[75] M. K. Miller, R. G. Forbes, Atom-Probe Tomography, Springer US, 2014. doi:10.1007/978-1-4899-7430-3.

[76] D. Edwards, E. Simonen, S. Bruemmer, Evolution of fine-scale defects in stainless steels neutron-irradiated at 275 ℃, Journal of Nuclear Materials 317 (1) (2003) 13–31. doi:10.1016/s0022-3115(03)00002-3.

[77] A. Etienne, M. Hernández-Mayoral, C. Genevois, B. Radiguet, P. Pareige, Dislocation loop evolution under ion irradiation in austenitic stainless steels, Journal of Nuclear Materials 400 (1) (2010) 56–63. doi:10.1016/j.jnucmat.2010.02.009.

[78] J. Gigax, T. Chen, H. Kim, J. Wang, L. Price, E. Aydogan, S. Maloy, D. Schreiber, M. Toloczko, F. Garner, L. Shao, Radiation response of alloy T91 at damage levels up to 1000 peak dpa, Journal of Nuclear Materials 482 (2016) 257–265. doi:10.1016/j.jnucmat.2016.10.003.

[79] T. Chen, E. Aydogan, J. G. Gigax, D. Chen, J. Wang, X. Wang, S. Ukai, F. Garner, L. Shao, Microstructural changes and void swelling of a 12Cr ODS ferritic-martensitic alloy after high-dpa self-ion irradiation, Journal of Nuclear Materials 467 (2015) 42–49. doi:10.1016/j.jnucmat.2015.09.016.

[80] L. Shao, C.-C. Wei, J. Gigax, A. Aitkaliyeva, D. Chen, B. Sencer, F. Garner, Effect of defect imbalance on void swelling distributions produced in pure iron irradiated with 3.5 MeV self-ions, Journal of Nuclear Materials 453 (1–3) (2014) 176–181. doi:10.1016/j.jnucmat.2014.06.002.

[81] F. Garner, Impact of the injected interstitial on the correlation of charged particle and neutron-induced radiation damage, Journal of Nuclear Materials 117 (1983) 177–197. doi:10.1016/0022-3115(83)90023-5.

[82] G. Gupta, Z. Jiao, A. Ham, J. Busby, G. Was, Microstructural evolution of proton irradiated T91, Journal of Nuclear Materials 351 (1–3) (2006) 162–173. doi:10.1016/j.jnucmat.2006.02.028.

[83] C. Deo, C. Tomé, R. Lebensohn, S. Maloy, Modeling and simulation of irradiation hardening in structural ferritic steels for advanced nuclear reactors, Journal of Nuclear Materials 377 (1) (2008) 136–140. doi:10.1016/j.jnucmat.2008.02.064.

[84] W.-Y. Chen, Y. Miao, J. Gan, M. A. Okuniewski, S. A. Maloy, J. F. Stubbins, Neutron irradiation effects in fe and fe–cr at 300 ℃, Acta Materialia 111 (2016) 407–416. doi:10.1016/j.actamat.2016.03.060.

[85] K. G. Field, X. Hu, K. C. Littrell, Y. Yamamoto, L. L. Snead, Radiation tolerance of neutron-irradiated model Fe–Cr–Al alloys, Journal of Nuclear Materials 465 (2015) 746–755. doi:10.1016/j.jnucmat.2015.06.023.

[86] F. Bergner, C. Pareige, M. Hernández-Mayoral, L. Malerba, C. Heintze, Application of a three-feature dispersed-barrier hardening model to neutron-irradiated Fe–Cr model alloys, Journal of Nuclear Materials 448 (1–3) (2014) 96–102. doi:10.1016/j.jnucmat.2014.01.024.

[87] T. Chen, L. Tan, L. He, B. Tyburska-Püschel, K. Sridharan, Microstructural evolution in Fe–20Cr–25Ni austenitic alloys under proton irradiation at 670 ℃, in: Transactions of the American Nuclear Society, Vol. 117, 2017, pp. 581–583.

[88] T. Allen, J. Cole, C. Trybus, D. Porter, H. Tsai, F. Garner, E. Kenik, T. Yoshitake, J. Ohta, The effect of dose rate on the response of austenitic stainless steels to neutron radiation, Journal of Nuclear Materials 348 (1–2) (2006) 148–164. doi:10.1016/j.jnucmat.2005.09.011.

[89] F. Garner, M. Hamilton, N. Panayotou, G. Johnson, The microstructural origins of yield strength changes in AISI 316 during fission or fusion irradiation, Journal of Nuclear Materials 104 (1981) 803–807. doi:10.1016/0022-3115(82)90698-5.

[90] J. T. Busby, M. C. Hash, G. S. Was, The relationship between hardness and yield stress in irradiated austenitic and ferritic steels, Journal of Nuclear Materials 336 (2–3) (2005) 267–278. doi:10.1016/j.jnucmat.2004.09.024.

[91] A. Lupinacci, K. Chen, Y. Li, M. Kunz, Z. Jiao, G. Was, M. Abad, A. Minor, P. Hosemann, Characterization of ion beam irradiated 304 stainless steel utilizing nanoindentation and Laue microdiffraction, Journal of Nuclear Materials 458 (2015) 70–76. doi:10.1016/j.jnucmat.2014.11.050.

[92] A. C. Fischer-Cripps, Nanoindentation, Springer New York, 2004. doi:10.1007/978-1-4757-5943-3.

[93] H. Kitahara, R. Ueji, N. Tsuji, Y. Minamino, Crystallographic features of lath martensite in low-carbon steel, Acta Materialia 54 (5) (2006) 1279–1288. doi:10.1016/j.actamat.2005.11.001.

[94] D. Kaoumi, J. Adamson, M. Kirk, Microstructure evolution of two model ferritic/martensitic steels under in situ ion irradiation at low doses (0–2 dpa), Journal of Nuclear Materials 445 (1–3) (2014) 12–19. doi:10.1016/j.jnucmat.2013.10.047.

[95] S. Jublot-Leclerc, X. Li, L. Legras, M.-L. Lescoat, F. Fortuna, A. Gentils, Microstructure of Au-ion irradiated 316L and FeNiCr austenitic stainless steels, Journal of Nuclear Materials 480 (2016) 436–446. doi:10.1016/j.jnucmat.2016.08.006.

[96] M. Matijasevic, W. V. Renterghem, A. Almazouzi, Characterization of irradiated single crystals of Fe and Fe–15Cr, Acta Materialia 57 (5) (2009) 1577–1585. doi:10.1016/j.actamat.2008.11.042.

[97] M. Hernández-Mayoral, D. Gómez-Briceño, Transmission electron microscopy study on neutron irradiated pure iron and RPV model alloys, Journal of Nuclear Materials 399 (2–3) (2010) 146–153. doi:10.1016/j.jnucmat.2009.11.013.

[98] R. Averback, Atomic displacement processes in irradiated metals, Journal of Nuclear Materials 216 (1994) 49–62. doi:10.1016/0022-3115(94)90006-x.

[99] P. Hosemann, D. Kiener, Y. Wang, S. A. Maloy, Issues to consider using nano indentation on shallow ion beam irradiated materials, Journal of Nuclear Materials 425 (1–3) (2012) 136–139. doi:10.1016/j.jnucmat.2011.11.070.

[100] Z. Jiao, N. Ham, G. Was, Microstructure of helium-implanted and proton-irradiated T91 ferritic/martensitic steel, Journal of Nuclear Materials 367–370 (2007) 440–445. doi:10.1016/j.jnucmat.2007.03.118.

[101] J. V. den Bosch, O. Anderoglu, R. Dickerson, M. Hartl, P. Dickerson, J. Aguiar, P. Hosemann, M. Toloczko, S. Maloy, SANS and TEM of ferritic–martensitic steel T91 irradiated in FFTF up to 184 dpa at 413 ℃, Journal of Nuclear Materials 440 (1–3) (2013) 91–97. doi:10.1016/j.jnucmat.2013.04.025.

[102] G. Odette, M. Alinger, B. Wirth, Recent developments in irradiation-resistant steels, Annual Review of Materials Research 38 (1) (2008) 471–503. doi:10.1146/annurev.matsci.38.060407.130315.

[103] R. Klueh, J. Vitek, Elevated-temperature tensile properties of irradiated 9Cr–1MoVNb steel, Journal of Nuclear Materials 132 (1) (1985) 27–31. doi:10.1016/0022-3115(85)90389-7.

[104] A. Alamo, J. Bertin, V. Shamardin, P. Wident, Mechanical properties of 9Cr martensitic steels and ODS-FeCr alloys after neutron irradiation at 325 ℃ up to 42 dpa, Journal of Nuclear Materials 367–370 (2007) 54–59. doi:10.1016/j.jnucmat.2007.03.166.

[105] X. Liu, Y. Miao, M. Li, M. A. Kirk, G. Zhang, S. Ukai, S. A. Maloy, J. F. Stubbins, Radiation resistance of oxide dispersion strengthened alloys: Perspectives from in situ observations and rate theory calculations, Scripta Materialia 148 (2018) 33–36. doi:10.1016/j.scriptamat.2018.01.018.

INCOMPLETE LIST OF PUBLICATIONS

Publications

1. X. Liu, J. Gigax, L. Shao, F. Garner, J. Stubbins, Frank loops and irradiation hardening in self-ion irradiated austenitic alloy 709, in preparation.

2. X. Liu, J. Gigax, J. Poplawsky, W. Guo, L. Shao, F. Garner, J. Stubbins, Ion irradiation induced microstructural and mechanical property modifications of austenitic alloy 709 at 500℃, in preparation.

3. X. Liu, Y. Miao, M. Li, M. Kirk, G. Zhang, S. Ukai, S. Maloy, J. Stubbins, Radiation resistance of oxide dispersion strengthened alloys: Perspectives from in situ observations and rate theory calculations, Scripta Materialia 148 (2018) 33–36.

4. X. Liu, Y. Miao, M. Li, M. Kirk, S. Maloy, J. Stubbins, Ion-irradiation-induced microstructural modifications in ferritic/martensitic steel T91, Journal of Nuclear Materials 490 (2017) 305–316.

Conference Presentations

1. X. Liu, J. Gigax, L. Shao, F. Garner, J. Stubbins, Radiation-induced microstructural evolution and hardening of austenitic alloy 709, accepted by ANS Annual Meeting 2018.

2. X. Liu, Y. Miao, W.-Y. Chen, Y. Wu, M. Li, J. Stubbins, Transactions of the American Nuclear Society 116 (2017) 369–370.

3. X. Liu, Y. Miao, D. Krumwiede. P. Hosemann, M. Li, M. Kirk. J. Stubbins, Ion irradiation damage in ferrtic/martensitic steel T91, TMS 2016 Annual Meeting & Exhibition, Febuary 14–18, Nashville, TN, USA.